Nanoscale Light-Matter Interactions in the Near-Field of High-Q Microresonators

A Thesis
Presented to
Academic Faculty

by

Ali Asghar Eftekhar

In Partial Fulfillment
of the Requirements for the Degree
Doctor of Philosophy in Electrical and Computer Engineering

School of Electrical and Computer Engineering
Georgia Institute of Technology
December 2011

Nanoscale Light-Matter Interactions in the Near-Field of High-Q Microresonators

Approved by:

Dr. Ali Adibi, Advisor
School of Electrical and Computer Engineering
Georgia Institute of Technology

Dr. Thomas K. Gaylord
School of Electrical and Computer Engineering
Georgia Institute of Technology

Dr. John A Buck
School of Electrical and Computer Engineering
Georgia Institute of Technology

Dr. Maysam Ghovanloo
School of Electrical and Computer Engineering
Georgia Institute of Technology

Dr. Rick Trebino
School of Physics
Georgia Institute of Technology

Date Approved: Oct. 26, 2011

In the Name of God, the Beneficent, the Merciful

To my dear Sara, Amir Hossein, and Zoha and to my parents

ACKNOWLEDGMENTS

I would like to thank my advisor, Professor Ali Adibi, for his support and encouragement and for providing me with the opportunity to explore many different ideas and be involved in many different multi-disciplinary researches during my PhD studies. During the course of my PhD program I have worked on many different projects under Dr. Adibi's supervision and we had long discussion meetings. I have learned a lot from him, not only from academic perspective of the work, but also from his wise and thoughtful approach in facing with challenges and leading large scale research programs. I also thank his family for their warm hospitality.

I would also like to thank my committee members, Dr. Thomas Gaylord, Dr. John A. Buck, Dr. Maysam Ghovanloo, and Dr. Rick Trebino for their time, supports and feedback on my work.

During my many years in Photonic Research Group in Georgia Tech, I have enjoyed having the opportunity to work with many of my colleagues and learning from them. I especially thank Dr. Siva Yegnanarayanan, Dr. Babak Momeni, and Dr. Mohammad Soltani. I enjoyed working closely with Siva on many different projects and research proposals. I also had very fruitful discussion with Babak and Mohammad. I also would like to acknowledge Dr. Saeed Mohammadi, Dr. Amir Atabaki, Dr. Charles Camp, Dr. Ali Hashmi, Pouyan Mohajerani, Qing Li, Zhixuan Xia, Farshid Ghasemi, Payam Alipour, and Ali Behrouz that I have collaborated with them in different projects.

I also appreciate the helps and supports from all former and current photonic research group members, including Dr. Majid Badiei, Dr. Ehsan Shahhosseini, Dr. Murtaza

Askari, Dr. Saman Jafarpour, Dr. Charles Reinke, Yee Lou, Maysam Chamanzar, Majid Sodagar, Hossein Taheri, Hessam Moradinejad, Hamed Mousavi, and Amir hossein Hosseininia.

I have had the chance of studying in the same university with a few of my old friends. This old friendship has helped me to always feel at home from the first day that I came to Georgia Tech. I would like to thank Dr. Omid Momtahan, Dr. Arash Karbaschi, and Dr. Reza Sarvari for their friendship and for all good times that we had together in Atlanta.

Finally, from bottom of my heart, I would like to thank my parents to whom I'm indebted forever, my dear wife, Sara, and my wonderful children Amir Hossein and Zoha. Sara has been my best friend and advisor during all these years. I could never go through this period of my life without her kind support in all aspect of works and without her wisdom, kindness, patience, and vision. In the most difficult situation, she always has been the one who has brought hope to me and has been willing to sacrifice. She has been the best thing that has happened to me in my entire life.

TABLE OF CONTENTS

LIST OF TABLES

LIST OF FIGURES

LIST OF ABBREVIATIONS

Acronym	Definition
1D	One Dimensional
2D	Two Dimensional
3D	Three Dimensional
AFM	Atomic force microscopy
ANSOM	Aperture-less near-field scanning optical microscopy
AOFS	Acousto-optic frequency shifter
CW	Clockwise
CCW	Counter-clockwise
CCD	Charged-coupled detector
CROW	Coupled resonator waveguide
CWMR	Coupled waveguide-microdisk resonator
DAQ	Data Acquisition
DDA	Discrete dipole approximation
EBL	Electron Beam Lithography
EDFA	Erbium doped fiber amplifier
FDTD	Finite difference time domain
FE	Finite element
FEM	Finite element method
FOM	Figure of merit
FP	Fabry-Perot
FSR	Free spectral range
GMT	Generalized multi-pole technique
HSQ	Hydrogen Silsequioxane
IR	Infrared
LCORR	Liquid core optical ring resonator
LSPR	Longitudinal surface plasmon resonance
MZ	Mach-Zehnder
NIL	Nanoimprint lithography
NIR	Near Infrared
NSOM	Near-field scanning optical microscopy
PC	Polarization controller
PC	Photonic crystal
PDMS	Polydimethylsiloxane
PMD	polarization mode dispersion
PML	Perfectly matches layer
Q	Quality factor
Q/V	Q-over-mode-volume
QED	Quantum electrodynamics
RIU	Refractive index unit

RF	Radio frequency
RMSAD	Root mean square alignment deviation
RMSD	Root mean square displacement
SEM	Scanning electron microscope
SERS	Surface enhanced Raman scattering
Si	Silicon
SiN	Silicon Nitride
SOI	Silicon on insulator
SPR	Surface plasmon resonance
TE	Transverse electric
TFDM	Thin-film dielectric material
TM	Transverse magnetic
TMM	Transfer matrix method
TWR	Traveling-wave resonator
UV	Ultraviolet
WGM	Whispering Gallery Mode

LIST OF SYMBOLS

Notation	Description
a_{cw}	Amplitude of the clockwise mode in the microdisk resonator
a_{ccw}	Amplitude of the counter-clockwise mode in the microdisk resonator
a_{np}	Amplitude of the surface plasmon resonant mode of the nanoparticle
α_{η}	Transverse components of the polarizability
α_{p}	Dielectric nanoparticle polarizability
α_{ξ}	Longitudinal components of the polarizability
β	Guided wave propagation-constant (Chapter 2)
β	Coupling rate between the degenerated microdisk resonator modes (Chapter 3)
c	Speed of the light in vacuum
ΔU_c	Change in the total stored energy in the microdisk resonator
$\delta\omega$	Microdisk resonator frequency detuning
$\Delta\omega_0$	Initial microdisk resonator frequency detuning
$\Delta\omega_c$	Microdisk resonator half linewidth
$\Delta\omega_{np}$	The detuning between the microdisk resonator and the nanoparticle
$\Delta\omega_p$	Nanoparticle-induce shift in the microdisk resonance wavelength
$E_c^{\max}$	Maximum electric field intensity in the microdisk resonator
$E_c(r_0)$	Microdisk resonator electric field intensity at the position r_0
$E_{np}(r)$	nanoparticle electric field at the position r
$E_{np}^{\max}$	Maximum electric field intensity of the surface plasmon nanoparticle
$\bar{\varepsilon}(\omega, r)$	Effective dispersive permittivity of the nanoparticle
ε_c	Microdisk resonator permittivity
ε_i	Microdisk cladding environment permittivity
ε_m	Nanoparticle permittivity
f_{grad}	Optical gradient force
f_p	Optical propulsive force
Γ_0	Intrinsic loss rate of the microdisk resonator
Γ_c	Loss rate of the unperturbed microdisk resonator modes
Γ_{in}	Coupling rate between the input waveguide and the microdisk resonator
Γ_{in}^{Opt}	Optimal coupling rate between the input waveguide and the microdisk

Γ_{np}	Loss rate of the nanoparticle resonant mode
Γ_{p}	Particle-induced loss rate of the microdisk resonator
η	Microdisk cladding fluid viscosity
k_t	Optical trap spring constant
K_B	Boltzmann constant
κ	Coupling rate between the nanoparticle and the microdisk resonator
$\kappa_{\max}$	Maximum coupling rate between the nanoparticle and the microdisk
κ_{opt}	Optimal coupling rate between the nanoparticle and the microdisk
m	Azimuthal mode orders of a TWR
n_g	Effective group index
n_{eff}	Effective refractive index of the microdisk resonator
n_s	Microdisk resonator cladding material refractive index
P_{in}	Input waveguide power
P_{np}	Total power extinction through the nanoparticle
Q_c	Loaded quality factor of a resonator
Q_i	Intrinsic quality factor of a resonator
Q_L	Overall (i.e. loaded) quality factor
r_p	Trapped nanoparticle radius
S	Poynting vector on the travelling wave in the microdisk resonator
S_{in}	Amplitude of the guide mode in the input waveguide
S_t	Optical trap stability factor
σ_a	Nanoparticle absorption cross-section
σ_{ex}	Nanoparticle extinction cross-section
σ_p	Dielectric nanoparticle scattering cross-section
σ_s	Nanoparticle scattering cross-section
T	System temperature
$t(\delta\omega)$	Transmission spectrum of the coupled waveguide and microdisk resonator
τ	Exerted optical torque on the nanoparticle
τ_0	Intrinsic photon lifetime of a resonator
τ_c	Wave guide coupling photon lifetime of a resonator
$\tau_{\xi\eta}$	The exerted torque on the nanoparticle in the radial-vertical plane
τ_L	Overall photon lifetime in a resonator
U_c	Total stored energy in the microdisk resonator
U_{np}	Stored optical energy in the nanoparticle
V_c	Microdisk resonator mode volume
V_{np}	Surface plasmon nanoparticle mode volume

V_{rod}	Surface plasmon nanoparticle volume
ω_c	Resonance frequency of the microdisk resonator
ω_{np}	Surface plasmon resonance frequency of the nanoparticle
ξ	Trapped nanoparticle displacement in the radial-vertical plane

SUMMARY

An optical resonator is a structure that can trap the light in a small volume and for an extended period of time. This enables to achieve a high density of optical energy and electromagnetic field intensity. The large field enhancement in the compact optical resonators considerably enhances the light-matter interactions and amplifies both linear and non-linear optical processes. This enhancement enables many different applications including lasing, optical switching, strong-coupling cavity quantum electrodynamics (QED), nanoparticle trapping and manipulation, and chemical and biological sensing. Among different alternative optical resonators, microdisk and microring resonators have attracted much attention as they provide high-quality factors and small mode-volumes.

The main objective of this research has been to study the light-matter interactions in the near-field of high-Q microdisk resonators. In this work, we initially developed the required characterization tools to study the near-field interactions in the vicinity of a microdisk resonator. The developed tools, then, is used to investigate the applications enabled by the strong local field enhancement in the high-Q microdisk resonators.

In this research, I developed an alternative approach for the near-field characterization of high-Q microdisks. In this approach, a tiny atomic force microscopy (AFM) tip is used as a small controllable perturbation. The perturbation, caused by the AFM tip, depends on the local near-field intensity at the tip position. Therefore, the local field intensity of the microdisk resonator can be estimated from the measured changes in the microdisk resonator properties (e.g., loss, and resonance wavelength shift), caused by the AFM tip. This technique not only enables high-resolution imaging of the near-field

profile of the optical modes in high-Q resonators, but also can be used as a tool to investigate different near-field phenomena such as near-field mode coupling and optical forces.

In this thesis, I also investigated the application of the high-Q microdisk resonators for nanoparticle manipulation and sensing. I theoretically studied the possibility of the simultaneous trapping and sensing of nanoparticles using compact high-Q microdisk resonators. My focus, in this work, has been on using small microdisk resonators, fabricated on silicon on isolator (SOI) wafers, at infrared wavelengths. The interaction of a microdisk resonator with a surface plasmon nanoparticle is also theoretically studied. Furthermore, the optimal conditions and requirements for the combined-microdisk resonator-gold nanorod field enhancement, gold nanorod trapping, and gold nanoparticle alignment are discussed. Our proposed resonator-enhanced SERS sensing is based on compact microdisks, fabricated on silicon nitride on oxide platform and excited at visible and near-infrared (NIR) wavelengths.

CHAPTER 1

INTRODUCTION

Near-field optics is the study of localized fields and their interaction with matter. The near-field region is defined as the region in space where the evanescent waves cannot be neglected. The optical near-field is localized to the surface of materials or devices that guide, confine, or interact with light. Near-field optics, in a broad sense, can be defined as the ability to localize, monitor, or manipulate optical processes in sub-wavelength scales. By confining light to small volumes and for long periods of time, optical micro/nanoresonators considerably enhance the near-field intensity. This results in a much stronger light–matter interaction in the vicinity of the micro/nanoresonators. This enhancement is needed for many different applications, including lasing, optical switching, strong-coupling cavity quantum electrodynamics (QED), and chemical and biological sensing [1, 2, 3, 4]. The temporal and spatial confinements in the optical resonators are usually quantified by the resonator quality factor (Q) and mode volume (V)[1]. A smaller mode volume and a higher quality factor correspond to a larger local field enhancement. Different microresonator structures have been proposed that can provide high-Qs and small mode volumes. Ultra-high whispering galley mode resonators with the $Q > 10^9$ based on microsphere and microtoroid structures have been reported [5, 6]. On

[1] The photon lifetime (τ) in the cavity is proportional to the Q over the resonance frequency (ω) (i.e., $\tau = 2Q/\omega$).

the other hand, photonic crystal (PC) resonators can provide relatively high-Qs and very small mode volumes [7, 8, 9]. Among different alternatives, microdisk and microring resonators have been actively pursued in silicon-based materials such as silicon (Si) [10] and silicon nitride (SiN) [11]. The high quality factors and small mode volumes of microdisk resonators, in addition to other advantages, such as ease of fabrication, integrability with mature silicon (Si) electronics, and their flexibility in the tuning of the waveguide-resonator coupling, make them the preferred choice for large-scale integrated photonic platforms.

The main objective of this research was the study of light-matter interactions in the near-field of high-Q microdisk resonators. In this work, I initially developed the required characterization tools to study the near-field interactions in the vicinity of a microdisk resonator. Then the developed tools are used to investigate the applications enabled by the strong local field enhancement in the high-Q microdisk resonators.

Near-field scanning optical microscopy (NSOM) provides a powerful tool for the investigation of near-field optics in integrated optics devices [12]. Traditional NSOM techniques typically use tapered optical fibers (often metal coated) to collect light from the evanescent field through a sub-wavelength-sized aperture [13]; however, the relatively large size of the NSOM aperture needed to collect enough power not only limits the measurement spatial resolution, but also, more importantly, in the case of high-Q resonators, considerably perturbs the mode structure. In this research, I have developed an alternative approach for the near-field characterization of high-Q microdisks. In this approach, a tiny atomic force microscopy (AFM) tip is used as a small controllable perturbation. The perturbation, caused by the AFM tip, depends on the local near-field

intensity at the tip position; therefore, the local field intensity of the microdisk resonator can be estimated from the measured changes in the microdisk resonator properties (e.g., loss and resonance wavelength shift) caused by the AFM tip. This technique not only enables high-resolution imaging of the near-field profile of the optical modes in high-Q resonators, but also can be used as a tool to investigate different near-field phenomena such as near-field mode coupling and optical forces.

The strong light-matter interactions in the near-field of microdisk resonators considerably enhance both linear and nonlinear optical processes and make them very sensitive to small changes in the their surrounding environment. These properties introduce the microdisk resonators as a unique solution for optical sensors based on different sensing modalities. In recent years, integrated photonic sensing has been an intensely active area of research [14]. Different optical biosensing techniques have been studied in which the analyte selectively binds to a captured molecule immobilized on the surface of a waveguide or resonator (i.e., surface coating) through an affinity interaction. The detection mechanisms in biophotonic sensors can be classified into three categories: mass sensors, fluorescence sensors, and Raman sensors. Mass sensors measure the presence of the captured analyte by detecting changes in the sensor optical transmission caused by the bound analyte [15]. Although the mass sensors have been shown to provide a high sensitivity for many applications [16], they are ineffective for analytes with small molecular weights and are sensitive to nonspecific binding.

Fluorescence sensors measure the emission from an immobilized fluorescently labeled analyte and are generally more sensitive and more specific than mass sensors [17]; however, fluorescence measurements usually require pre-processing of the input

analyte to fluorescently label them. This intermediate labeling step complicates the sample preparation and detection process. On the other hand, fluorescent measurements do not provide any detailed molecular information. Raman scattering is capable of providing highly resolved molecular vibrational information, which enables the unique detection of the structural properties of target substances. Although Raman scattering by itself is an extremely inefficient process and its scattering cross-sections are much smaller than those of fluorescent labels, surface-enhanced Raman scattering (SERS) considerably enhances the Raman scattering cross-sections and has enabled single molecule detection [18].

Microdisk resonators can considerably enhance the detection sensitivity of the aforementioned sensing modalities (i.e., mass sensing, fluorescent sensing, and Raman sensing). The small mode volume and high-Q of the microdisk resonators lead to a high mass sensitivity and a very small detection limit for microdisk resonator-based mass sensors [19, 20]. Because of the small mode volume of the microdisk resonators, a small perturbation can lead to a large shift in the resonance wavelength of the microdisk resonators. On the other hand, the high-Q of microdisk resonators makes it possible to detect a small shift in their resonance wavelength. The combination of these two enhancements enables a mass sensitivity in the range of sub-attograms, which corresponds to single molecule sensitivity.

While traditional Raman-based sensors have the advantage of molecular specificity and sensitivity, the Raman signal is inherently very weak and often masked by an auto-fluorescence background; therefore, high power laser sources and bulky filters and spectrometers are required to detect the Raman signal. An integrated microresonator can

also be used to improve the effective Raman cross-section of the desired target. Combining the high electric field enhancement in the microdisk resonator near-field with the SERS enhancement using metallic nanoparticles considerably increases the effective Raman scattering cross-section. The improved efficiency relaxes the requirements on high pump laser power and long integration time for detection based on Raman scattering.

Although the integrated optics sensors based on microresonators provide a very high sensitivity, this high sensitivity is provided over a relatively small area within the sensor. One of the major challenges in the design of resonator-based integrated optical sensors is sample delivery [21]. Generally, a microfluidic system is used to deliver the analyte samples to the vicinity of the microresonator surface. The desired analyte then selectively attaches to the resonator surface through chemical binding with the resonator surface coating; however, this chemical surface binding usually has a very low affinity and slow binding kinetics; therefore, the input sample should be confined to a small volume over the sensitive area to increase the binding probability. This requires microfluidic channels with very small cross-sections, which considerably increases the sensing assay time; therefore, there is a need for a new mechanism to transport the particle to the sensitive surface of the high-Q microdisks. One possible solution may be to use optical force to trap the particles on the surface of the microresonators. The application of optical forces to expedite particle transportation in microfluidic channels has attracted a lot of attention in recent years [22]; however, most of the work up till now has been limited to micrometer-sized particles [23]. The large local field enhancement and sharp field gradient in the microdisk resonators near-field result in a large optical force, which

enables trapping of small nanoparticles with diameters as small as a few tens of nanometers at relatively low input power.

In this thesis, I have developed a new sensing paradigm based on simultaneous trapping and sensing of nanoparticles using compact, high-Q microdisk resonators. The proposed approach is pursued in two different sensing modalities, namely, mass sensing and SERS sensing. In the first sensing modality, I envision developing mass sensors based on compact and high-Q microdisk resonators with the ability to attract and trap large molecules and small nanoparticles by optical forces. In the second modality, my goal is to trap and align a gold nanoparticle in a microdisk resonator trap to enable resonator-enhanced SERS sensing based on combined microresonator-gold nanorod field enhancement.

In this thesis, I theoretically study the possibility of the simultaneous trapping and sensing of nanoparticles using compact and high-Q microdisk resonators. My focus in this work is on using small microdisk resonators, fabricated on silicon on isolator (SOI) wafers, at infrared wavelengths. I also theoretically study the interaction of a microdisk resonator with a surface plasmon nanoparticle and discuss the optimal conditions and requirements for the combined microdisk resonator-gold nanorod field enhancement, gold nanorod trapping, and gold nanoparticle alignment. My proposed resonator-enhanced SERS sensing is based on compact microdisks, fabricated on silicon nitride on oxide platform, and excited at visible and near-infrared (NIR) wavelengths.

The organization of this thesis is as follows: in chapter 2, I provide an overview of high-Q resonators fabricated in Si and SiN platforms. In chapter 3, I describe the implementation of a near-field characterization setup that will be used for the near-field

characterization and manipulation of the high-Q resonators. In this chapter, I also develop a technique for high resolution near-field imaging of the near-field pattern for the resonant mode of high-Q resonators and the experimental results for the case of high-Q microdisk resonators are provided. In chapter 4, I discuss the application of compact and high-Q microdisk resonators for label-free sensing. Chapter 5 is devoted to the theoretical study of nanoparticle trapping using high-Q microdisk resonators. In chapter 6, I theoretically study the interactions between a high-Q microdisk resonator with a gold nanoparticle and the possibility of nanoparticle trapping and alignment in an optical trap. Finally, in the last two chapters, I suggest possible paths for the future continuation of this research and related works and discuss different aspects of the work in this thesis and draw some conclusions.

CHAPTER 2

FUNDAMENTALS OF TRAVELING-WAVE RESONATORS

In this chapter, we present the fundamental concepts of dielectric optical resonators and electromagnetic properties of traveling-wave resonators (TWRs). We will also discuss different aspect of the TWRs, including modeling of the different resonant modes, coupling between resonators and waveguides, and fabrication and characterization techniques for these structures.

2.1. Fundamentals of optical microresonators

An optical resonator is a structure that can confine the light (i.e., photons) at a specific wavelength, in a small volume, and for an extended period of the time. The wavelength at which this confinement is achieved is called the resonant wavelength of the resonator, and the solution of the Maxwell equations for the resonator structure at the resonance wavelength is called the resonant mode of the resonator.

Resonant modes of a resonator are eigenmode solutions of the Maxwell equations for the resonator structure; therefore, both the resonance wavelength and field distribution of the resonator resonant mode can be obtained by solving the Maxwell equations for the resonator geometry. The main features of the resonant modes of a resonator are the degree of the confinement in the temporal and the spatial domains, which can be quantified by the photon lifetime (τ_0) and the mode volume (V_m) of the resonator mode. The degree of temporal confinement of the light for any mode of a resonator is usually

expressed in terms of quality factor (Q_0), which is the ratio of the stored energy in the resonator to the energy loss or leakage in each period of the oscillation. The photon lifetime and the quality factor of the resonator at each wavelength are proportional and can be easily converted to each other using the following relation:

$$(Q_0 = \omega_0 \tau_0 / 2), \tag{2.1}$$

where ω_0 is the angular frequency of the resonant mode of the resonator. A longer photon lifetime or a higher quality factor in a resonator enables a higher field enhancement in the resonator and consequently a higher light-matter interaction, which is desired for many applications. The mode volume of any resonant mode of a resonator is defined as the ratio of the total stored energy in the resonator to the maximum energy density in the resonator:

$$V_m = U_c \max_r [0.5\varepsilon(r) |\mathrm{E}(r)|^2], \tag{2.2}$$

where U_c is the total stored energy in the resonator:

$$U_c = \int_V 0.5\varepsilon(r) |\mathrm{E}(r)|^2 dr^3, \tag{2.3}$$

In the above equation, $\varepsilon(r)$ is the electrical permittivity and $E(r)$ is the electric field intensity at the location r in the space. Similar to the case for the temporal confinement, a higher spatial confinement (i.e., smaller mode volume) results in a higher field intensity in the resonator, which can improve the light-matter interactions in the resonator. Therefore, in most of applications, a resonator with a smaller resonant mode volume is desired. However, reducing the size of a resonator usually results in a reduction of the resonator quality factor caused by the light radiation and scattering effects; therefore, achieving both high quality factor and small mode volume at the same time is a challenging problem.

2.2. Traveling-wave resonators (TWR) in thin film dielectric materials

Thin-film dielectric materials (TFDMs) are used in many applications as they allow fabricating photonic structures using conventional two-dimensional (2D) lithography and etching techniques. A TFDM is composed of a thin high-refractive index material on the top of a lower index substrate. Two common platforms for TFDM, which are the focus of this work are silicon-on-isolator (SOI) and thin-film-silicon-nitride-on-silicon-dioxide. Traveling wave resonators (TWRs) or whispering gallery mode (WGM) resonators are a category of resonators, where the confined electromagnetic field in the resonator propagates (i.e., travels) in a closed loop. Because of the symmetry between the clockwise (CW) and counter-clockwise (CCW) propagation directions, the modes in the TWRs are degenerated; therefore, at each resonance wavelength, the resonator supports one CW propagating mode and one CCW propagating mode. The main advantages of TWRs over alternative resonator designs such as PCs are the ease of their design and coupling to the conventional ridge waveguides. In contrast to the resonant modes of the standing-wave resonators, which concurrently interact with the forward-propagating and backward-propagating modes of a coupled waveguide, resonant modes of TWRs can selectively interact with either the forward or backward mode of a waveguide. This selective interaction considerably simplifies the design of the photonic structures based on the waveguide and resonator coupling. These features, along with the possibility to achieve high-Q and small-mode volume have made TWRs the most popular form of resonators in the integrated optics structures. Traveling-wave resonators in TFDM are usually fabricated in the form of microring or microdisk structures, which enable relatively high-Q and low-mode-volume resonators. Microrings and microdisks

resonators have auxiliary symmetry around their axes normal to the thin film plane; therefore, the solution of the Maxwell equations for these structures in the cylindrical coordinate can be written in the form of

$$\overline{E}(\bar{r},t) = \overline{E}(r,z)\exp(i\omega t - im\phi), \tag{2.4}$$

where $\overline{E}(\bar{r},t)$ is the electric field vector (the same form can be used for the magnetic field) at the position $\bar{r}$ and the time t and r, ϕ, and z correspond to radial, azimuth, and vertical components in the cylindrical coordinate, respectively. In this equation, m should be an integer to satisfy the phase continuity of the field after a 2π rotation and is called the azimuthal mode number; therefore, for each integer value of the m, the resonator may support one or more resonant modes for each polarization.

In auxiliary symmetric resonators with infinite thickness, the solution to the Maxwell equations can be separated to two orthogonal modes with different polarization; namely, transverse electric (TE) and transverse magnetic (TM) modes. In this case, the TE (TM) mode only includes transverse (i.e., in-plane in respect to the r-ϕ plane) components of the electric (magnetic) field and vertical (i.e, along z direction) component of magnetic (electric) field. In TWR resonators with finite thickness, these two modes are mixed and generate two orthogonal modes with mixed polarizations; however, in most cases they still keep a dominant TE or TM element and, therefore, are called as quasi-TE and quasi-TM modes. The quasi-TE and quasi-TM terms are usually shortened to the TE and TM, respectively, for brevity. The thickness of TFDM is usually selected to have a single mode slab structure at the desired wavelengths; therefore, TWRs in these platforms usually support a single vertical mode for each polarization. However, for each different

azimuthal mode order (i.e., *m*), TWRs may support several different modes, which are identified by their radial mode order.

Similar to any propagating wave, a propagation-constant (β) can be defined for the confined traveling resonant mode in a resonator. For each azimuthal mode order *m*, we have, $\beta L = 2\pi m$, where L is the effective cavity length or the perimeter of the resonator (i.e., $L = 2\pi R$, where R is the radius of the resonator). In the same way, an effective index (n_{eff}) can be defined for the resonator as

$$n_{eff} = \frac{c\beta}{\omega_0} = \frac{m\lambda_0}{L}. \tag{2.5}$$

Although different modes of a TWR resonator with different radial mode order have different effective indexes, the resonant modes corresponding to the same radial mode order for different azimuthal mode orders (*m*) have similar field patterns and effective indexes (ignoring the effect of the dispersion). The frequency range between two consecutive modes with the same radial mode numbers is called free spectral range (FSR) and can be calculated as

$$FSR^{(\omega)} = \omega_0^{(m+1)} - \omega_0^{(m)} = \frac{\Delta\omega_0}{\Delta\beta}\frac{2\pi}{L} = \frac{2\pi c}{n_g L}, \tag{2.6}$$

where n_g ($n_g = n_{eff} + \omega\, dn_{eff}/d\omega$) is the effective group index of the resonant mode of the resonator.

2.3. Numerical simulation of optical modes in TWRs

Analytical solutions are not available for the case of TWRs with finite thickness. Different numerical simulation, such as finite difference time domain (FDTD) and finite element method (FEM) have been employed to solve for the solution of the Maxwell

equations in TWR structures. While a full 3D simulation of the Maxwell equation using any of the proposed numerical methods is computationally cumbersome, the 2D FEM model based on the axial symmetry of the structure provides a relatively low computation cost solution. In this technique, for each azimuthal mode order *m*, the resonant frequency and field distribution in the *r-z* plane (Refer to the Equation 2.4) are found by solving for the eigenvalue and eigenvector of the Maxwell equations using 2D FEM. While Maxwell equations in 3D are not full-ranked, using axial symmetry in TWRs, it is possible to reduce the Maxwell equations to a second-order full-ranked equation that only includes in-plane magnetic field (i.e., H_r, and H_z) components. Then, the magnetic field component normal to the r-z plane (i.e., H_θ) and the electric field components can be calculated from the in-plane magnetic field components. The detail of the formulation for calculation of the optical modes of TWRs using 2D FEM can be found in [24]. Figure 2.1 shows an example of a TWR on SOI platform, where the resonant modes of a microdisk resonator are calculated using the 2D FEM method.

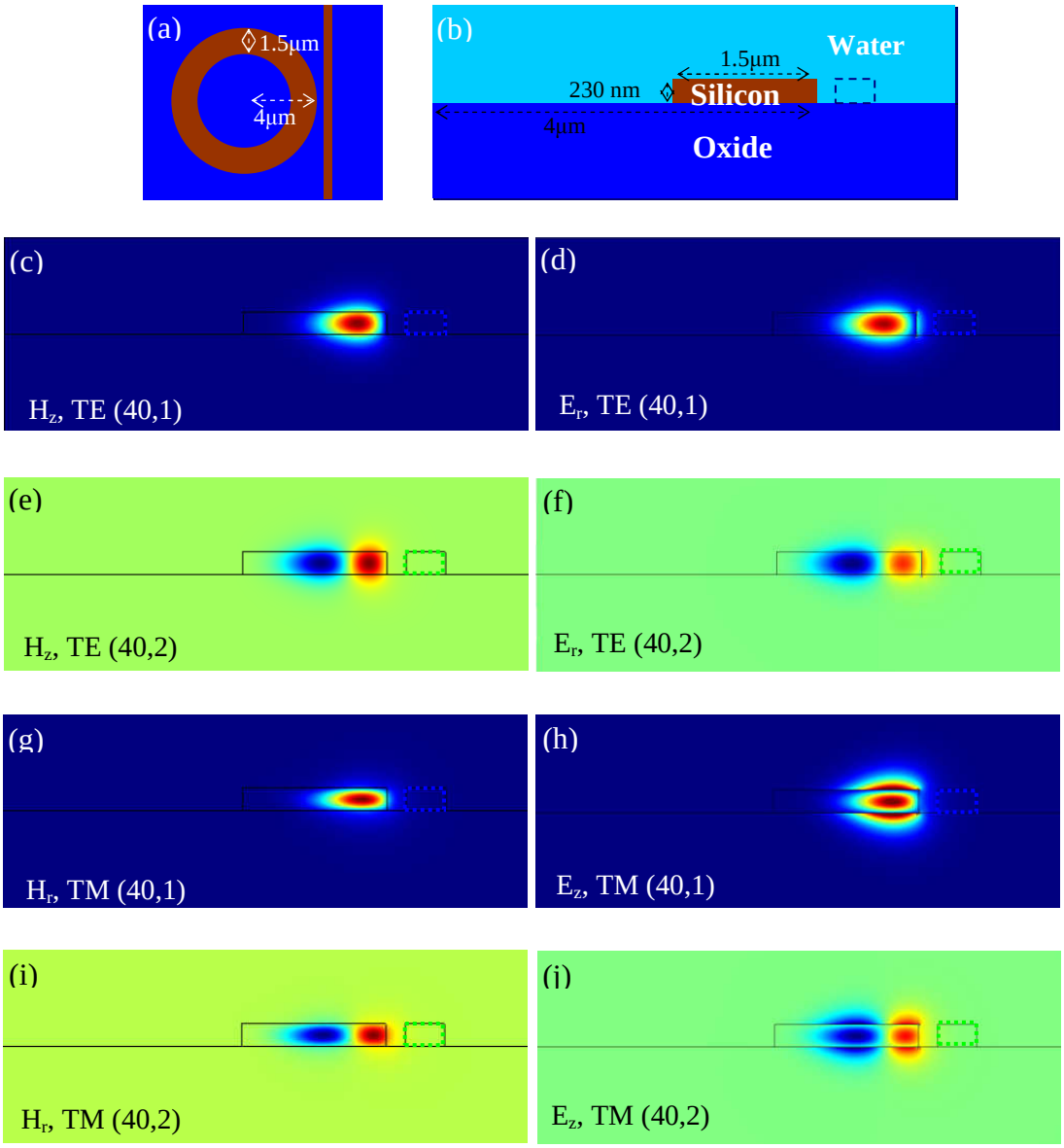

Figure 2.1: Calculation of the resonant modes of a microdisk resonator with a hole at its center (i.e., microdonut) using 2D FEM with axial symmetry. The simulated structure is a microdonut with an outer radius of 4µm made in a 230 nm thick Si layer on oxide substrate. The resonator cladding is water. (a) and (b) show schematic top and side view of the simulated structure. (c-f) show the dominant magnetic and electric fields (i.e., H_z, and E_r) corresponding to the first and second-radial-order modes of the resonator for the TE polarization corresponding to the azimuthal mode order m = 40. (g-j) show the dominant magnetic and electric fields (i.e., H_r, and E_z) corresponding to the first-radial-order and second-radial-order modes of the resonator for the TM polarization corresponding to the azimuthal mode order, m = 40.

2.4. Traveling-wave resonators on SOI platform

The resonant modes of microdisk resonators are confined at the edge of the microdisk by the refractive index contrast between the microdisk and its surrounding material. The curved trajectory of the confined light results in the radiation loss, which is one of the limiting factors of the Q of the TWRs. The amount of the radiation loss (i.e., the radiation loss-limited Q) depends on the resonator geometry (i.e., thickness and diameter) and the refractive index contrast between the disk and the surrounding dielectric material. Apparently, a lower resonator refractive index and a smaller disk diameter (i.e., higher light trajectory curvature) result in a lower propagation loss-limited Q.

The main advantage of the microdisk resonators as compared to the single-mode microring resonators is their higher Q. This higher Q is enabled by having a single etched side wall (as compared to two etched side walls for microrings) and lower field overlap with the etched side wall that results in smaller scattering loss due to the surface roughness and surface absorption. However, one issue with the microdisk resonators is their multi-mode nature as they can provide resonant modes with multiple radial mode orders (refer to Figure 2.2 as an example). As an example, an Si microdisk resonator on SOI with a thickness of 220 nm and diameter of 40 μm can support high-Q modes with more than 20 different radial-mode orders. This multi-mode nature of microdisk resonators results in a crowded spectrum and very small overall effective single-mode FSR. The higher-order modes of the microdisk resonator for the same azimuthal order modes have higher frequencies, smaller effective indexes, and larger radial spans. The number of the resonant modes of a microdisk can be reduced by etching a hole in the center the microdisk to form a microring (or microdonut)-shaped structure or (and) by

shrinking the size of the microdisk. Both these changes result in reducing the effective indexes of the higher radial-order modes so that they become leaky and the modified structure only supports lower radial-order modes. An extreme case is when the width of the microring structure is reduced to that of a single mode waveguide and, therefore, the microring resonator also only supports a single resonant radial mode.

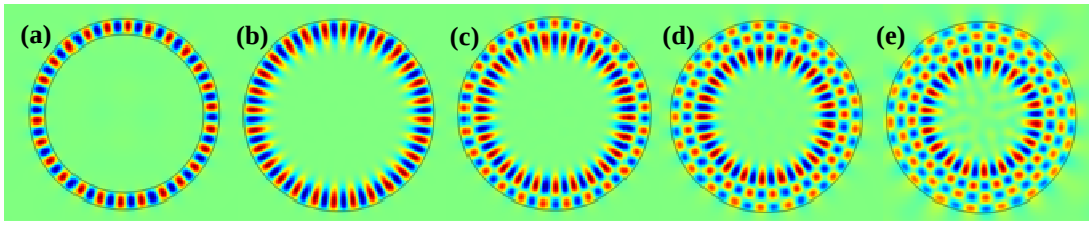

Figure 2.2: (a) 2D FEM simulation of resonant modes of a microring and a microdisk resonator. (a) The dominant magnetic field (H_z) profile of the TE resonant modes of the microring resonator. (b-e) The dominant magnetic field (H_z) profiles of the first to fourth order radial mode of the microdisk resonator for TE polarization.

Different properties of microdisk resonators, such as their FSR, Q, and mode volume depend on their geometry (i.e., thickness, diameter, and width). Figure 2.3 shows the effective index and FSR of the first and second-radial-order TE-polarized and first-radial-order TM-polarized modes of microdisk resonators with different diameters. Smaller TWR resonators (i.e., TWRs with smaller diameters) have larger FSRs and smaller mode volumes; however, shrinking the size of the resonator results in a lower Q, as it results in higher radiation losses and higher surface scattering and absorption losses. With the typical fabrication techniques, the quality factor of a typical microdisk is mainly limited by the surface scattering and surface absorption losses, which put a much tighter limit on the Q as compared to radiation-loss-limited Q. Further reduction of the microdisk size pushes the optical modes of the microdisk towards the edges of the microdisk and results in higher field overlap with the etched surfaces of the microdisk and consequently higher losses. Therefore, for any specific application, the size of the microdisk resonator

should be adjusted based on a trade-off between different desired specifications, including FSR, mode volume, Q, and compactness of the structure. For example, microdisk resonators in thin film SOIs, with diameters less than 4 μm, not only provide a large single mode FSR as large as 57-70 nm in a very small footprint, but also they provide a higher Q-over-mode-volume (Q/V) as compared to the larger microdisks. This makes the compact microdisk resonators the favorite choice for many applications, including low power nonlinear optical devices, multiplexed sensing, and particle trapping and manipulation using the optical force.

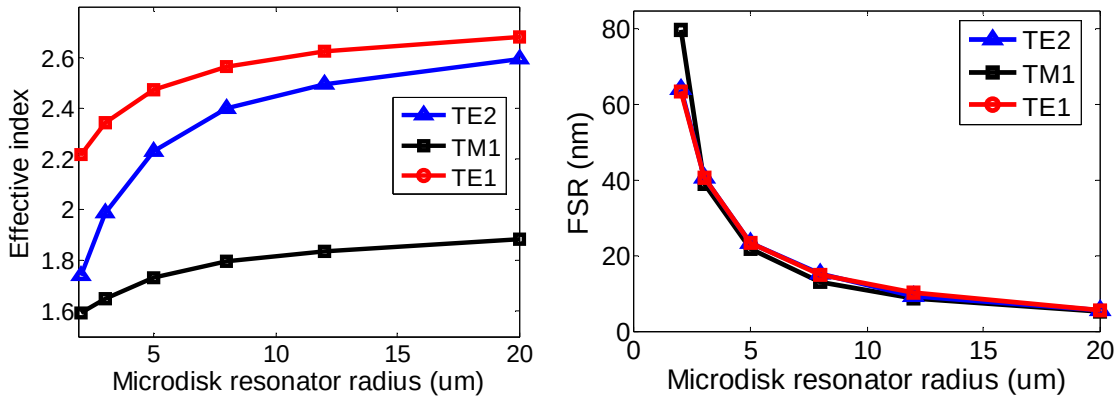

Figure 2.3: Calculated (a) effective index (n_e) and (b) FSR of the first and the second radial quasi-TE modes (TE1 and TE2, respectively) and the first order TM mode of a Si microdisk resonator versus its diameter for resonance wavelengths in a range around 1550 nm. The microdisk resonators for these simulations have a thickness of 220 nm over the oxide substrate and have a water cladding.

2.5. Waveguide coupling to TWRs

In most of the integrated optics applications, the light is coupled into and out of the resonator through a waveguide coupled to the resonator. One of the main techniques for the coupling of a waveguide to TWRs is side coupling, where the waveguide is brought into close proximity with the resonator to allow evanescent coupling between the waveguide and the resonator. The main advantage of this coupling scheme is that the

waveguides and resonators are fabricated on the same optical layer and, therefore, the coupling between the waveguide and resonator can be adjusted by tailoring the coupling geometry. Similar to the case of a waveguide-waveguide coupler, the coupling between a waveguide and a resonator depends on the effective field overlap between the waveguide and resonator optical modes, the coupling length, the phase mismatch between their propagating modes.

The analysis of the coupling between waveguides and resonators is usually done either in time domain [25] or in the frequency domain using a transfer matrix (i.e., space domain) approach [26]. Each of these approaches has its own advantages. Time domain analysis is a more general approach and can be applied to any coupled waveguide-resonator or resonator-resonator problem at wavelengths close to their resonance wavelengths. On the other hand, space domain approach is especially useful for TWRs and can be used to analyze the coupling regime over a wider bandwidth and for multiple FSRs at the same time.

2.5.1. Time-domain analysis of the waveguide coupling to TWR resonators

In the time domain analysis, the field amplitude of the resonator is normalized to the total stored energy in the resonator. Assuming there is no coupling between the two degenerated modes of a TWR, the equations that govern the time evolution of the EM fields in a waveguide coupled TWR and at the frequencies near its resonance frequency (ω_0) can be written as follows [26]:

$$\frac{da_c^t}{dt} = (j\omega_0 - 1/\tau_0 - 1/\tau_c)a_c^t + j\kappa_t S_{in}. \tag{2.7}$$

In this equation, a_c^t and S_{in} are the field amplitude of the resonant mode of the TWR and propagating waveguide mode, normalized to the total stored energy in the resonator (U_c)

and total propagating power (P_w) in the waveguide, respectively (i.e., $|a_c^t|^2 = U_c$ and $|S_{in}|^2 = P_w$). In addition, τ_0 and τ_c are the photon lifetime in the resonator corresponding to the intrinsic loss and coupling to the waveguide, respectively. Finally, κ_t ($\kappa_t = \sqrt{2/\tau_c}$) is the coupling rate between the waveguide and the resonator. As it is evident from Equation 2.7, the overall photon lifetime in the resonator (τ_L) can be calculated as $\tau_L = 1/(1/\tau_0 + 1/\tau_c)$. By taking a Fourier transform from Equation 2.7, the field inside the resonator in frequency domain can be found as

$$a_c^t(\omega) = \frac{\kappa_t}{j(\omega - \omega_0) + 1/\tau_0 + 1/\tau_c} S_{in}(\omega). \tag{2.8}$$

To quantify the effect of the intrinsic loss and the coupling on the overall (i.e. loaded) quality factor (Q_L) of a waveguide-coupled resonator, a coupling quality factor (Q_C) is defined, which is related to the coupling photon lifetime as $Q_C = \omega\tau_c/2$ (Refer to Equation 2.1). Then, the overall quality factor of the resonator (Q_L) can be calculated as $Q_L = 1/(1/Q_0 + 1/Q_c)$.

2.5.2. Space-domain analysis of the waveguide coupling to TWR resonators

In the space domain analysis, the resonator field amplitude is normalized to the traveling power (P_{tr}) in the resonator (i.e., $|a_c^s|^2 = P_{tr}$). In this case, the coupled waveguide-TWR is modeled by a waveguide-waveguide coupler at the coupling region and a feedback-path, which corresponds to a single round trip path of the traveling wave through the TWR (See Figure 2.4). The coupling equation in the space domain can be written as

$$a_c^s(\omega) = \lambda_s \gamma_s e^{-j\phi_{RT}} a_c^s(\omega) + j\kappa_s S_{in}. \tag{2.9}$$

In this equation, $a_c^s(\omega)$ is the normalized amplitude of the traveling wave in the resonator; λ_s and κ_s ($\lambda_s^2 + \kappa_s^2 = 1$) are the transmission and coupling coefficient of the waveguide-resonator coupler; γ_s is the equivalent round trip transmission of the resonator, $\delta\omega = \omega - \omega_0$ is the frequency detuning from the resonator resonance at ω_0; and, finally, ϕ_{RT} is the resonator round trip phase modulo 2π. At the resonance wavelength, we have $\beta(\omega_0)L = 2\pi m$; therefore, ϕ_{RT} can be found as $\phi_{RT} = \delta\beta(\omega)L = \delta\omega t_r$, where t_r ($t_r = n_g L / c$) is the round trip time for the traveling wave in the resonator. Then, the solution for the traveling wave in the resonator can be found as

$$a_c^s(\omega) = \frac{j\kappa_s}{1 - \lambda_s \gamma_s e^{-j\delta\omega t_r}} S_{in}. \tag{2.10}$$

For small detuning from the resonator resonance frequency (as compared to the resonator FSR), and κ_s, $(1-\gamma_s) << 1$, we have:

$$a_c^s(\omega) = \frac{j\kappa_s / t_r}{j\delta\omega + \kappa_s^2 / 2t_r + (1-\gamma_s)/t_r} S_{in}. \tag{2.11}$$

Comparing Equation 2.11 and Equation 2.8 and noting that $U_c = t_r P_{tr}$, the waveguide-resonator coupling coefficient for the time domain analysis (κ_t) and space domain analysis (κ_s) can be related as $\kappa_t = \kappa_s / \sqrt{t_r}$. Also, the intrinsic photon lifetime (τ_0) can be related to the round trip transmission of the resonator by $\tau_0 = t_r/(1-\gamma_s)$. In the rest of this thesis, unless it is specifically mentioned, we use the time domain analysis and $a_c(\omega)$ and κ refer to $a_c^t(\omega)$ and κ_t, respectively.

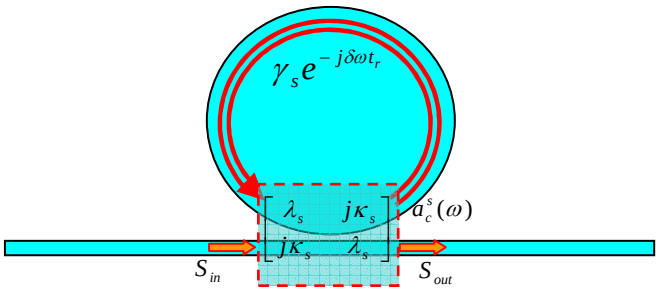

Figure 2.4: Schematic of the waveguide–resonator coupling using space domain modeling.

2.5.3. Coupled waveguide-resonator transmission

In a coupled waveguide-resonator system, the input light form the waveguide is coupled to the resonator and is trapped in the resonator for a period of time corresponding to the overall resonator photon lifetime (τ_L). When the resonator is excited at its resonance frequency (i.e., $\omega=\omega_0$), the stored energy in the resonator reaches its maximum and can be calculated from Equation 2.8 as

$$U_c = \frac{2/\tau_c}{(1/\tau_0 + 1/\tau_c)^2} P_w . \tag{2.12}$$

For any resonator with an specific intrinsic photon lifetime (τ_0), the stored energy in the resonator depends on the coupling strength between the waveguide and the resonator (i.e., $\kappa^2 = 2/\tau_c$) and the overall resonator photon lifetime (τ_L). As can be inferred from Equation 2.12, the maximum value of U_c is achieved when $\tau_0 = \tau_c$. The built up field in resonator couples back to the input waveguide with the same coupling rate and interferes with the waveguide input light. Therefore, the amplitude of the output power of the waveguide (S_{out}) can written as

$$S_{out} = S_{in} + j\kappa a_c . \tag{2.13}$$

By combining Equation 2.13 and Equation 2.10 the waveguide transmission spectrum ($T(\omega) = S_{out}(\omega)/S_{in}(\omega)$) can be written as

$$T = \frac{S_{out}(\omega)}{S_{in}(\omega)} = \frac{j(\omega-\omega_0)+1/\tau_0-1/\tau_c}{j(\omega-\omega_0)+1/\tau_0+1/\tau_c}. \quad (2.14)$$

It is interesting that at the condition for achieving maximum U_c (i.e., $\omega=\omega_0$ and $\tau_0 = \tau_c$), the waveguide output power vanishes. This coupling condition is called critical-coupling and corresponds to the condition where the whole input power from the waveguide in coupled to the resonator and is lost (or consumed) through it. If the coupling strength between the waveguide and resonator is weaker than this threshold, it is referred to as under-coupling regime and if it is stronger, it is called over-coupling regime. Figure 2.5 shows the stored energy in the resonator and the waveguide transmission (amplitude and phase) for a waveguide-coupled TWR resonator for different coupling regimes. As can be seen from Equation 2.14, switching between the resonator intrinsic and coupling Qs does not change the transmission amplitude of this system; however, it completely changes transmission phase response.

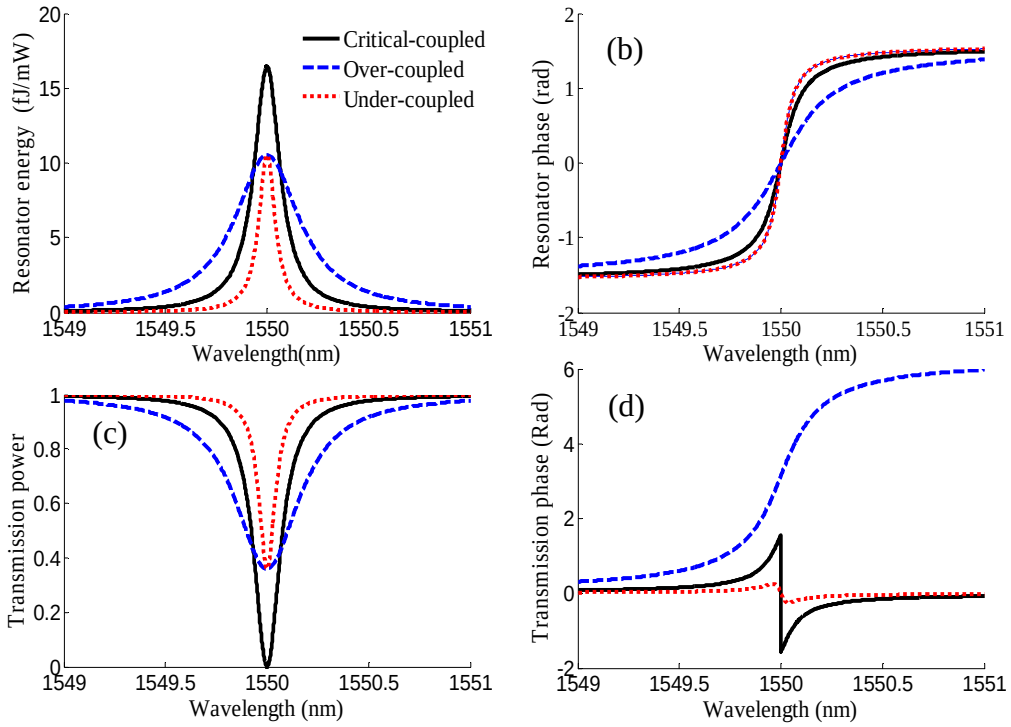

Figure 2.5: The stored energy in the resonator and the waveguide transmission (amplitude and phase) for a waveguide coupled to a resonator with a resonant mode at λ=1550 nm (Q_0=*20,000)*. The ratio of the stored energy in the resonator to the input power of the waveguide, the relative phase of the field in the resonator to the field in the waveguide at coupling point, the waveguide transmission amplitude, and the waveguide transmission phase are shown in the figures (a), (b), (c), and (d), respectively. The solid black, dashed blue, and dotted red lines show different coupling regimes for critically-coupled, over-coupled (Q_c=*5,000*), and under-coupled (Q_c=*80,000*) cases, respectively.

2.5.4. Waveguide-resonator coupling rate

The coupling between the waveguide and resonator (κ) can be calculated using the coupled-mode theory by integrating the waveguide-resonator field overlap over the waveguide. For a TWR side coupled to a waveguide, the coupling between the TWR resonant mode with an azimuthal mode order m and the waveguide mode, propagating along *z* direction with a wave propagation-constant β, can be calculated as [27]

$$\kappa = -\frac{j\omega_0}{4}\int_V \Delta\varepsilon_w \overline{E}_c^*(\bar{r})e^{jm\phi}\overline{E}_w(\bar{r})e^{-j\beta z}dV \ . \qquad (2.15)$$

In this equation, $\overline{E}_c(\bar{r})$ and $\overline{E}_w(\bar{r})$ are the resonator and waveguide modes normalized electric field vector and $\Delta\varepsilon_w$ is the permittivity perturbation in vicinity of the resonator caused by the adjacent waveguide. The integration is done over the waveguide perturbation volume (Figure 2.6).

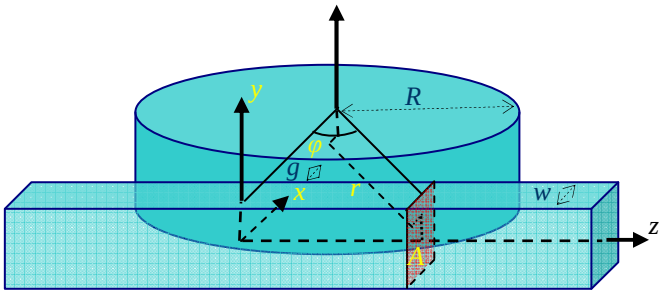

Figure 2.6: Schematic of the waveguide-resonator coupling geometry

For a specific mode of a given resonator, the coupling between the resonator and waveguide can be adjusted by 1) changing the gap between the waveguide and resonator (g) to change the waveguide-resonator modes field overlap, 2) changing the waveguide width (w) to adjust the phase mismatch between the waveguide and resonator modes, and 3) tailoring the waveguide geometry (e.g., curving the waveguide around the resonator) to change the effective waveguide-resonator coupling length. A detailed study of the waveguide-resonator coupling can be found at [28]. Figure 2.7 shows the coupling Q (Q_c) between the first order, TE-polarized, resonant mode of a fully etched Si microdisk resonator and the propagating mode of a straight waveguide versus the waveguide-resonator gap size for different cladding materials. The thickness of the Si layer in this simulation is 220 nm. The microdisk resonator diameter and the waveguide width are 4μm and 400 nm, respectively. As is evident from this figure, Q_c increases exponentially with increasing the waveguide-resonator gap. Also, much higher coupling rates (i.e.,

lower coupling Qs) can be obtained using oxide and water cladding as compared to the air cladding with the same microdisk resonator-waveguide gap.

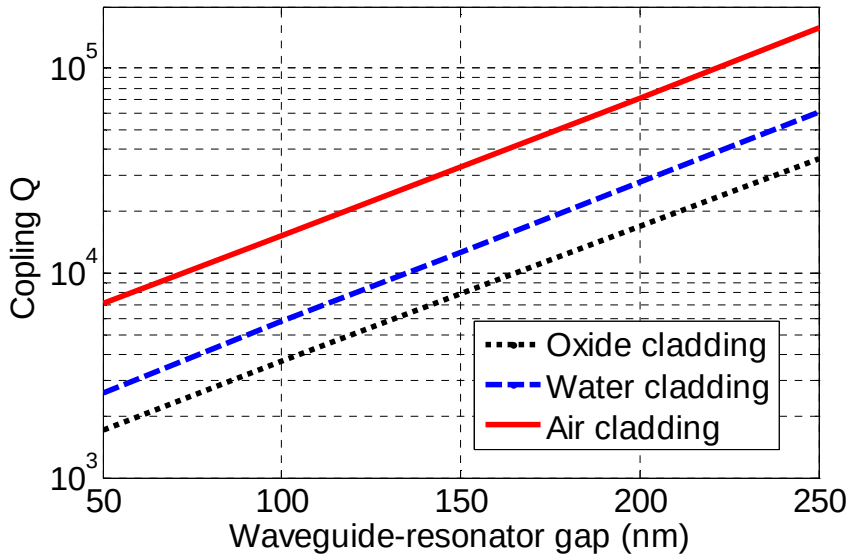

Figure 2.7: The coupling Q (Q_c) between the first order, TE polarized, resonant mode of a fully etched Si microdisk resonator and the propagating mode of a straight waveguide versus the waveguide-resonator gap size for different cladding materials. The thickness of the Si layer in this simulation is 220 nm. The microdisk resonator diameter and the waveguide width are 4 μm and 400 nm, respectively.

2.6. Fabrication of TWRs on SOI platforms

The small features size of the integrated photonic devices fabricated in thin dielectric films (i.e., thin SOI or SiN on oxide) and the high sensitivity of the their specifications to variations in feature sizes and the device surface quality demand a precise fabrication process. The fabrication of passive photonic structures usually includes two main steps, 1) a nanolithography step to define the device pattern and 2) an etching step to transfer the pattern to the dielectric film. These main processes may be followed by further processing steps, such as protecting the device with a cladding layer or integrating active controls, such as PN junction or thermal heaters with the structure. The nanolithography step is usually done either directly using electron-beam (E-beam) lithography [29] or

indirectly by deep ultra violet (UV) lithography or nanoimprint lithography [30], using an E-beam-fabricated mask. The design of a fabrication process for the high-Q resonators in TFDM requires careful optimization of different fabrication steps, including lithography, etching, and post fabrication steps to achieve steep sidewall angles, low side wall roughness, and good control over the size of the photonic device features.

2.6.1 Fabrication on integrated photonic structures using E-beam lithography

In contrast to more conventional optical lithography, in electron beam (E-beam) lithography a focused electron beam is used to achieve a higher resolution (far beyond the diffraction limited resolution in conventional optical lithography). The electron beam scans across the sample surface, covered by a thin layer of electron resist. Then, the electron resist is patterned by selectively removing (i.e., developing) the exposed (for positive resist) or not exposed (for negative resist) areas of the electron resist using a resist developer. Then, the E-beam pattern is transferred to the device layer by dry etching. The minimum resolution that can be obtained using E-beam lithography depends on several parameters, including the electron bean shape and size, the E-beam resist thickness, resist development contrast, and etch selectivity of the resist layer over the device film. The main advantage of the E-beam lithography is the very high resolution it can provide. Furthermore, the mask-less nature of E-beam lithography makes it very flexible. However, the main draw back of E-beam lithography is its very low throughput. E-beam lithography is widely used to fabricate mask for other lithography techniques, such as nanoImprint lithography and deep UV lithography. The high resolution and rapid turn around of E-beam lithography also make it an excellent choice for academic research applications as it is now widely used in many universities and research institutes. Figure

2.8 shows an example of the devices fabricated using E-beam lithography (JEOL JBX-9300FS 100kV electron beam lithography system at MiRC in Georgia Tech) and dry etching. Our extensive analysis based on three dimensional atomic force microscopy (3D AFM) and comparing with the experimental results show that a side wall roughness less than 1nm with a correlation length of 30nm and relative dimension accuracy as low as 1nm can be achieved using this system [31]. The minimum achievable feature size depends on the type of resist and the resist thickness. Lines with dimensions as low as 19 nm has been demonstrated using this system [32].

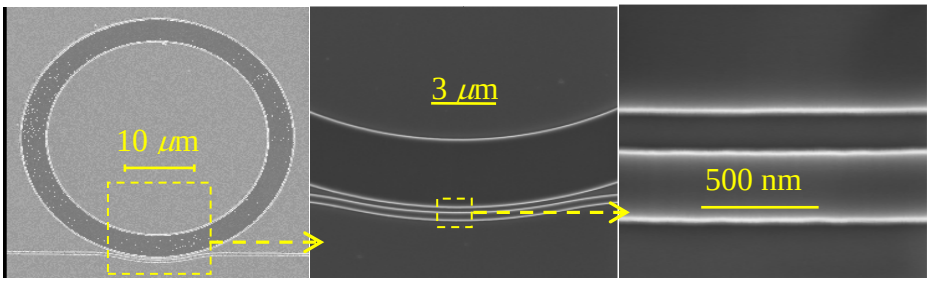

Figure 2.8: Scanning electron microscopy (SEM) image of a Si microdisk resonator side-coupled to a Si ridge waveguide.

2.6.2 Fabrication of integrated photonic devices using deep UV lithography

In contrast to E-beam lithography, deep UV lithography uses short wavelength UV lights with wavelengths at 193nm and 248nm to transfer the pattern on a mask to a photo-resist layer spun on the top of the target sample. Currently, masks technologies of 0.13um to 0.25um are used. The possibility of using step-and-scan tools enables to make many replicates of the same structure using the same mask in a very short time. While deep UV lithography tools are more expensive and require masks (that need to be fabricated using E-beam lithography), they are currently the only commercially available foundry service for large-scale fabrication of the integrated photonic circuits. Figure 2.9 shows examples

of the photonic integrated structures fabricated using deep epiXfab's deep UV Si-photonic foundry run at IMEC facilities [33]. Comparing with the resonators fabricated using E-beam lithography; deep UV fabricated resonators have higher sidewall roughnesses and provide lower quality factors. However, the quality of the fabricated resonators still satisfies the requirements for many applications.

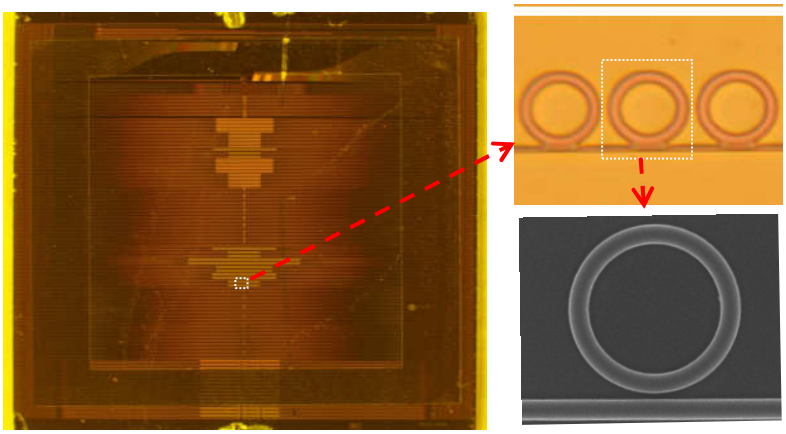

Figure 2.9: Optical micrograph of photonic devices fabricated using epiXfab services. Each chip (left image) is 6mm by 6mm die.

2.6.3 Fabrication of integrated photonic devices using NanoImprint lithography

Recently nanoimprint lithography (NIL) is also used for the fabrication of high-Q silicon microdisk resonators [30]. The nanoImprint lithography is completely different from deep UV and E-beam lithography as it depends on mechanical deformation of resist by applying pressure to the mask rather than chemically changing the resist by photon or electron exposure. The major advantage of thermal imprint is that it enables to precisely transfer a pattern from a master mold to a resist on the top of the device. The resolution of the NIL is limited by the features on the mask. This allows using precise and well-mastered but expensive techniques to make a single master, which can be used many times to copy the photonic device pattern with a low-cost process. Also, NIL enables to

achieve a much better control over feature sizes of different devices fabricated using the same mask than what can be achieved directly with E-beam or deep UV lithography [34]. NanoImprint Lithography is usually done using either thermal or UV resists. In contrast to UV NIL, thermal NIL has the advantage that does not require a transparent mask. This enables to benefit from well-developed fabrication process to make silicon master mold with high resolution and small surface roughness.

The process flow for the fabrication of the photonic devices using thermal NIL is summarized in Figure 2.9 [30]. In this process, the nanoImprint resist is spun on the top of the device wafer (e.g., SOI wafer) and the master mold is used to transfer the pattern to the nanoImprint resist at the elevated temperature. The thickness of the nanoImprint resist is adjusted to allow for a residual resist layer that enables the resist to smoothly flow laterally. The wafer is then cooled down to fix the resist pattern and the master mold is detached from the wafer. The mask is usually covered with an anti-sticking layer to facilitate the master detachment. The resist pattern is then transferred to the device layer by a two step dry etching where in the first step the residual resist layer is removed and in the next step the device layer is etched to form the desired photonic devices. Finally, the remaining resist layer is removed from the top of the photonic device.

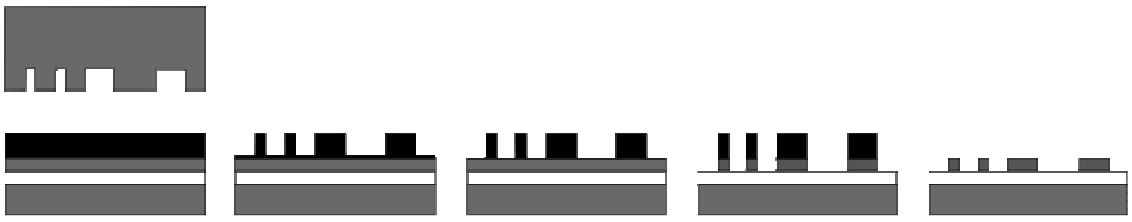

Figure 2.10: Summary of the process flow. (a) Imprinting of the resist coated SOI wafer. (b) Imprinted resist layer on top of the SOI wafer. (c) Etching of the residual resist thickness. (d): Etching of the silicon layer using the imprinted resist as a mask and the oxide layer as an etch stop. (e) Removal of the resist mask to get the final SOI device [30].

Figure 2.10 shows several example devices fabricated on a 230 nm thick SOI wafer [30] using a 250nm deep Si master mold. In these structures, gaps as small as 50 nm can be resolved.

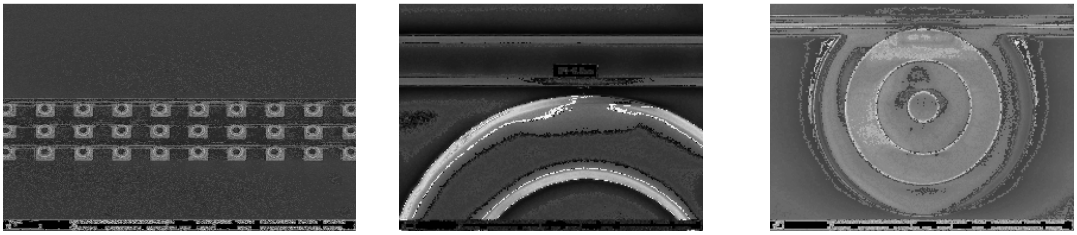

(a) (b) (c)

Figure 2.11: SEM images of several devices fabricated on SOI after the full process. (a) series of 4µm disk resonators.(b) close up on the sub 100nm gap between the resonator and the waveguide; (c) 20µm disk resonator.

2.7 Characterization of integrated photonic structures

The characterization of fabricated integrated photonic devices is usually done through the measurement of their optical transmission responses. In this schema, the light from a tunable laser is coupled to the structure through the input waveguide using either grating coupling or butt coupling. The output light of the structure is also collected through the output waveguide and is coupled to a detector. Then, the photonic device transmission is measured over the desired spectral range. Figure 2.11(a) shows the schematic of a typical characterization setup for integrated photonic devices. A tunable laser is used as the source. The light is coupled into and out of the structure using a set of tapered fibers. The tapered fibers are mounted on top of precision three-dimensional translation/tilt stages to enable high precision alignment of the input/output tapered fibers with the integrated input/output waveguides. The output light of the integrated device is coupled to a detector to measure the device transmission. The top view of the device is imaged on an infrared camera using a microscope system with a long working distance lens. The microscope

can navigate different portion of the integrate device and facilitates the input/output tapered fiber alignment to optimize the input/output coupling efficiency. Figures 2.11(b) and 2.12(c) show images of two separate measurement setups based on butt-coupling using tapered fibers and grating coupling, respectively. In the characterization setup in Figure 2.11(c), the sample is mounted on a thermal stage to stabilized the sample temperature and avoid the variation in the photonic device response, caused by thermal variations.

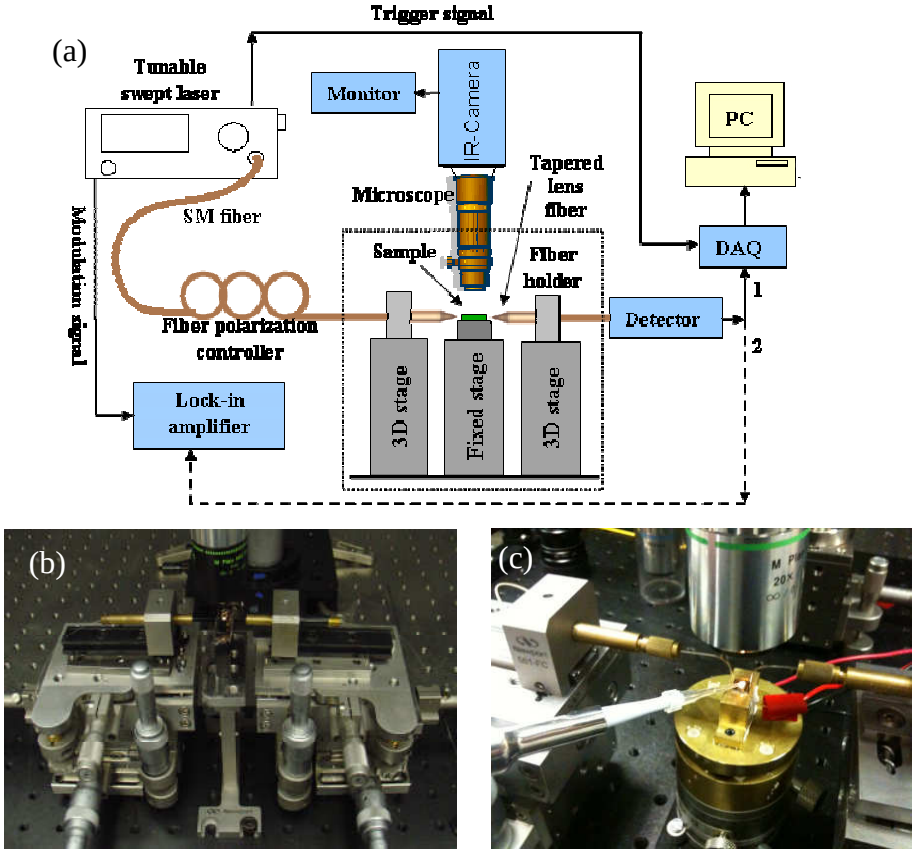

Figure 2.12: (a) schematic of the setup for the characterization of the of integrated photonic devices transmission. (b) and (c) the images of measurement setups based on butt-coupling using tapered fibers and grating coupling, respectively.

The measured optical response of an array of 32 resonators (2 µm radius microdisk) side coupled to a single waveguide, fabricated using nanoImprint lithography, is shown in Figure 2.12(a). The FSR of the resonators in the array is 54.6 nm. The resonance peak of each resonator is slightly offset to enable interrogation with a single waveguide input. A detailed spectral shape of a single resonance peak is shown in Figure 2.12(b). The extracted unloaded quality factor is 60,000, which is in the same range as those of devices directly fabricated by E-beam lithography, using the same process used to fabricate the mold masks. The resonance peaks of different microdisks show fairly uniform quality.

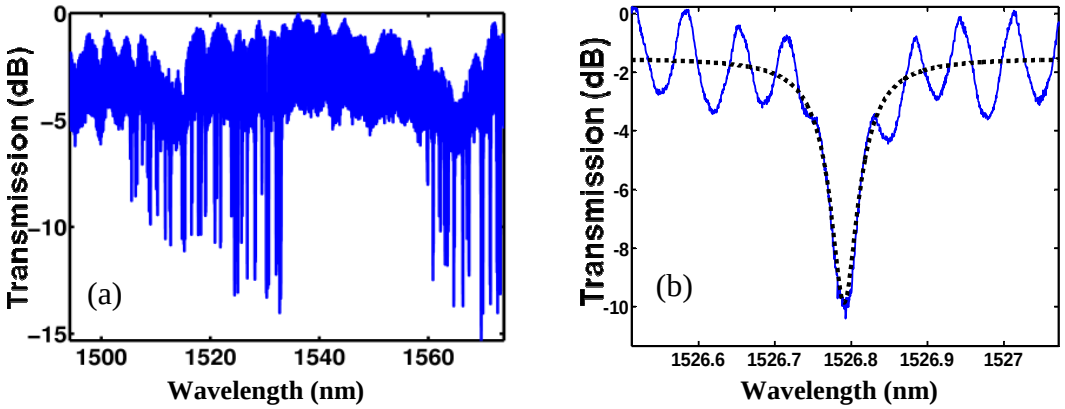

Figure 2.13: Optical response of a series of 4µm microdisk resonator as shown in Figure 2(a). (a) full spectral response.(b) close-up on a resonance peak and the lorentzian line-shape fit showing unloaded Q ~ 60,000 [30].

CHAPTER 3

Near-Field Characterization of High-Q Resonators

The history of near-field microscopy goes back to 1928, when Synge proposed using the scattered light from a small particle or collected light through a tiny aperture to overcome the diffraction limit of conventional microscopy techniques [12]. This proposal set the stage for what are now referred to as aperture-based and apertureless near-field scanning optical microscopy (NSOM). However, the first experimental demonstration of optical near-field microscopy was performed about half a century later in 1982 at the IBM Research Laboratories [35]. The combination of this technique with the atomic force microscopy (AFM) technique, which was invented later, to keep the tip distance with the photonic structure surface constant, has led to the currently available NSOM systems [36]. The conventional NSOM technique has been used to image the near-field intensity of the optical mode profile in different integrated optic devices including waveguides [37], photonic crystal waveguides and cavities [38, 39, 40], whispering gallery mode resonators [41], and plasmonic devices [42]. The application of coherent detection in NSOM systems (i.e., interferometric NSOM) also has enabled the simultaneously measurement of the near-field amplitude and phase of the optical signal in integrated devices [43]. As an alternative technique, aperture-less NSOM (ANSOM) techniques [44, 45, 46, 47], based on the collection of the scattered light from an AFM probe, has been used, which can potentially improve the NSOM imaging resolution and reduce the perturbation caused by the large size of the NSOM apertures. Transmission-based

ANSOM techniques also have been used to image the mode profile of integrated optics devices, such as waveguides [48] and microring resonators [49]. In this technique, the effect of the near-field perturbation on the integrated optics devices is used to estimate the near-field intensity. Similar near-field perturbation-based techniques have been used to image the mode profile of the photonic crystal (PC) resonators with a high resolution [50, 51, 52, 53, 54, 55].

In this thesis, I have developed a near-field characterization system for the characterization of high-Q resonators. I have developed a model for the interaction of a small nanoparticle with a traveling wave resonator (TWR) and using this model, a technique for the high resolution imaging of optical modes in high-Q TWRs is developed.

3.1 Development of a near-field characterization setup

To study the near-field properties of the optical modes in integrated optic platforms, a near-field optical characterization setup is realized. This near-field setup not only enables directly measurement of the near-field signals collected through an NSOM aperture, but also can be used to characterize the effect of the NSOM (or AFM) tip on the optical response (e.g., transmission) of the integrated optics device. Figure 3.1 shows the schematic of this setup. The developed near-field characterization setup is based on a tip-scanning AFM/NSOM head (Multi view 2000, Nanonics Inc.). A coherent detection scheme is developed to enable simultaneous detection of the amplitude and the phase of the output optical signal with high sensitivity. In this experimental setup, the input signal from a tunable laser (HP7560, HP-Agilent) is divided into the signal and reference arms using a 50/50 coupler/splitter. An acousto-optic frequency shifter (AOFS), (FCM-401E5C - Intraaction), driven by a 40 MHz radio frequency (RF) input signal, modulates

the signal in the reference arm. The light in the signal arm is coupled to the integrated photonic structure. The output signal (collected either from the output waveguide or from the near-field of the resonator structure) is mixed with the signal in the reference arm using another 50/50 coupler. The two outputs of the coupler are then detected by a set of balanced detectors (PDB150C, Thorlabs). Finally, a lock-in amplifier (SR844, Stanford Research Systems) is used to lock the differential output of the balanced detector to the AOFS modulating RF signal and extract the amplitude and phase of the output optical signal.

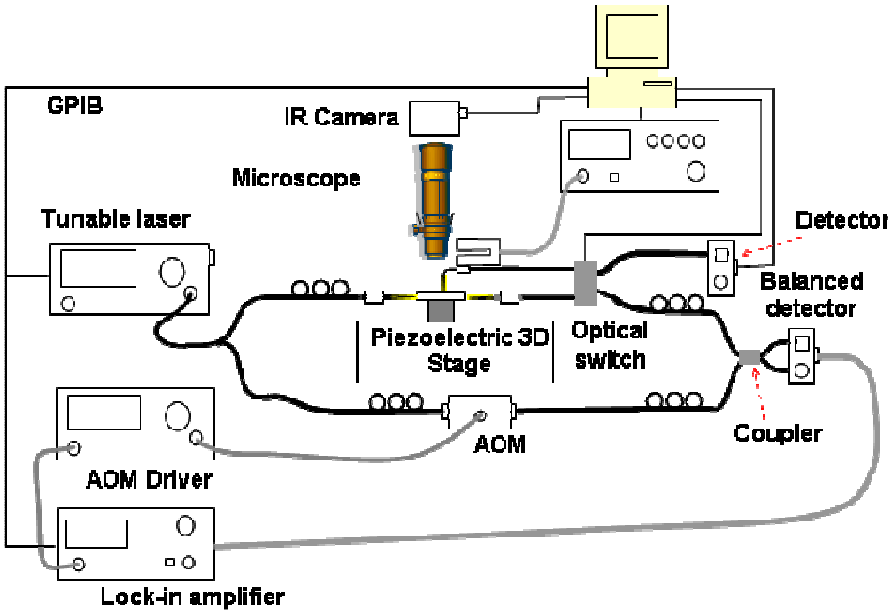

Figure 3.1: Schematic of the experimental setup for the characterization of the amplitude and the phase of the near-field optical signal. In this setup, the input light is coupled to the desired structure through the input waveguide using a tapered fiber. The output signal from the output waveguide coupled to the output tapered fiber and the light coupled to a fiber optic through the NOSM tip are measured concurrently. A two by two optical switch is used to route one of the optical outputs to a heterodyne detector and the other one to a very sensitive power detector.

In the developed setup, the input light is coupled to the desired structure through the input waveguide. The output light from the output waveguide and the light collected through the NOSM aperture are measured concurrently. A two-by-two optical switch is

used to route one of the optical outputs to the coherent heterodyne detector and the other one to a very sensitive power detector. As an alternative configuration, it is also possible to couple the light into the structure through the NSOM tip and collect the output signal from the output waveguide. This flexibility in excitation and signal collection enables us to use the NSOM system for different characterization modes, including (1) measurement of the amplitude and phase of the near-field electric signal; (2) near-field perturbation, where the tip is used as a small perturbation that perturbs the optical modes in the photonic structure; and (3) near-field excitation, where the NSOM tip is used as a dipole source to excite the optical modes in the photonic structure.

Our focus in this research is mainly on the first two approaches to enable high-resolution imaging of the near-field in integrated optics structures and to investigate the light-matter interactions in the near-field of high-Q resonators. High-resolution near-field imaging of the confined optical modes in the photonic structures requires using NSOM tips with small aperture sizes. Reducing the tip aperture size considerably reduces the coupling efficiency of the light through the NSOM tip aperture. This leads to a huge attenuation of the measurement signal. The heterodyne detection system used in the setup enables close to the shot-noise-limited detection sensitivity. An erbium doped fiber amplifier (EDFA) is used to amplify the input power from the tunable laser and, therefore, increase the tolerable transmission loss dynamic range of the system.

3.1.1 Analysis of the sensitivity and resolution of near-field measurement

The developed characterization setup is used for the characterization of the amplitude and noise of the near-field signal or optical transmission of the integrated photonic devices.

Different factors affect the accuracy of the amplitude and phase measurements using this setup.

In our setup, the reference signal goes through an AO frequency shifter, which shifts the input optical signal frequency by the frequency of the driving RF signal, f_M ($\omega_M/2\pi$). The signal in the measurement arm goes through the integrated optic device under measurement. In the ideal case, the signals in the reference and measurement arms ($E_{ref}(t)$ and $E_s(t)$, respectively) can be written as

$$E_{ref}(t) = \frac{1}{\sqrt{2}} A_{ref} e^{j(\omega_0 - \omega_M)t}, \tag{3.1}$$

and

$$E_s(t) = \frac{1}{\sqrt{2}} A_{in} t_s(\omega_0) e^{j(\omega_0 t + \phi_s(\omega_0))}. \tag{3.2}$$

In the above equations, A_{in} and A_{ref} are the normalized electric field amplitudes corresponding to the laser light at the signal and reference arms, respectively ($|A_{in}|^2 = P_{in}$ and $|A_{ref}|^2 = P_{ref}$), and ω_0 is the angular frequency of the input laser. Also, $t_s(\omega)$ and $\varphi(\omega)$ are the amplitude and phase of the photonic device transmission or near-field signal, respectively. The output of the balanced detector (i.e., the difference between the detected powers of the two balanced detectors $A_D(t) = P(D1) - P(D2)$) then can be written as

$$A_D(t) = \frac{1}{2}\left\langle \left| E_s(t) + E_{ref}(t) \right|^2 \right\rangle_t + \eta_{D1} + \eta_{P1} - \left\langle \frac{1}{2}\left| E_s(t) - E_{ref}(t) \right|^2 \right\rangle_t - \eta_{D2} - \eta_{P2}, \tag{3.3}$$

where η_{Di} and η_{Pi} are the thermal and Poisson noise of the detector i (Di). By replacing Equation 3.1 and Equation 3.2 in the above equation, the output signal ($A_D(t)$) can be written as

$$A_D(t) = A_{out} A_{ref} \cos(\omega_M t + \phi_s(\omega_0)) + \eta_{Dd} + \eta_{Pd}, \tag{3.4}$$

where $A_{out} = t_s(\omega_0)A_{in}$ ($|A_{out}|^2 = P_{out}$), $\eta_{Dd} = \eta_{D1} - \eta_{D2}$, and $\eta_{Pd} = \eta_{P1} - \eta_{P2}$ are the amplitude of the light signal at the output of measurement arm, the differential detector noise, and the overall detection Poisson noise, respectively. The equivalent-input-noise-power of each detector ($\sigma_{\eta_D} = <|\eta_{Di}|^2>^{0.5}$, for the detector used in the experiments in this thesis) is 0.3pW $Hz^{-0.5}$. Therefore, the equivalent differential detector noise power will be 0.42pW $Hz^{-0.5}$. On the other hand, assuming that the reference-arm power at the output is much higher than the signal power (i.e., $P_{ref} >> P_{out}$), the equivalent Poisson noise power at the output of the balanced detector is $\sqrt{P_{ref} E_{Photon}}$, where E_{Photon} is the energy per photon (i.e., $A_{ref}\sqrt{\hbar\omega_0}$ W $Hz^{-0.5}$). Comparing the detector and the Poisson noise contribution at the balanced detector output, for the reference-arm power larger than 1.4 μW, the Poisson noise will have the major contribution. Therefore, for the most cases in our experiments, where $P_{ref} >> 1.4\ \mu W$, the contribution of the detector-noise in the overall measurement noise is negligible and the measurements are Poisson-noise-limited. The transmission amplitude and phase of the measurement arm are measured using a lock-in amplifier, which mixes the balanced detector differential output with the reference RF signal (i.e., AOM excitation signal). The final measured amplitude signal-to-noise-ratio (SNR_{Amp}) and the estimated phase accuracy ($<|\delta\phi_s|^2>$) can be calculated as $SNR_{Amp} = t_{\text{int}} P_{out}/\hbar\omega_0$ and $<|\delta\phi_s|^2> = 1/SNR_{Amp}$, where t_{int} is the Lock-in amplifier integration time. As an example, for an integration time of 10 ms, a signal-to-noise-ratio of 20 dB and phase estimation standard deviation of 0.1 radians can be obtained with an output power of only 1.3 fW.

In the actual case, several other factors, such as input laser amplitude and wavelength stability, thermal phase drift, and leakage through the AO frequency shifter also affect the measurement sensitivity. One of the sources of the error in the measurement is the non-idealities in the AOM and the output coupler, which result in the leakage of an interference signal through the AOM and output coupler. While in the ideal case, the output of the AOM should only include the frequency shifted component of its input signal; in the actual case, a fraction of the non-diffracted signal at the original input frequency also couples to the AOM output. Therefore, the AOM output signal can be written as

$$E_{ref}(t) = A_{ref}(e^{j(\omega_0-\omega_M)t} + \alpha e^{j(\omega_0 t+\phi_a)}), \tag{3.5}$$

where α is the leakage ratio coefficient. If the output coupler be an ideal 50/50 coupler, this leaked signal will not affect the output measurement; however, in reality, the through and cross coupling coefficient of the coupler (i.e., λ and κ) are not exactly equal. Therefore, the balanced detector output can be written as

$$A_D(t) = 4\kappa\lambda A_s(t)A_{ref}\cos(\omega_M t + \phi_s(t)) + \alpha(\kappa^2-\lambda^2)\,|A_{ref}|^2\cos(\omega_M t + \phi_\alpha(t)). \tag{3.6}$$

In this equation, the first term in the right is the ideal output and the second term is the interference because of the leakage through the AOM and the output coupler. The AOFS used in this system provides an isolation factor of only about 55 dB for the input signal. Therefore, a small fraction of the signal at the original wavelength passes through the acousto-optic amplifier. On the other hand, both the fiber coupler and the balanced detectors in the coherent detection part of the system have some errors, which limit the overall common mode rejection ratio of the system to less than 30 dB. This generates an interference signal at the lock-in amplifier, only 85 dB below the power level in the

reference arm. To minimize the effect of this interference, an attenuator is used to adjust the power level in the reference arm to achieve the optimal performance based on a trade-off between the leakage interference and the coherent detection gain. To minimize the effect of the mechanical vibrations and thermal fluctuations on the phase measurement accuracy, the measurement setup is mechanically and thermally isolated from the environment.

While, the application of coherent detection enables to achieve high power sensitivity, the low coupling efficiency from the photonic device near-field to the NSOM probe still requires exciting the photonic structure with a high input optical power. However, in the case of high-Q resonators, the maximum applicable input power is limited by the threshold for nonlinear processes in the resonator. The large two-photon absorption and third-order (χ^3) nonlinearity in Si result in a low input power threshold for nonlinear processes. To avoid nonlinear stability, the input power of the waveguide should be limited to a certain threshold.

3.1.2 Characterization of the transmission amplitude and phase of high-Q resonators

Accurate measurement of the transmission amplitude and phase of the resonance-based photonic devices is essential for the characterization of their dispersive properties. Especially, in the case of microdisk resonators, the ambiguity about the over-coupling and under-coupling regimes in the transmission spectrum can only be resolved by the transmission phase spectrum [24].

Figure 3.2 shows the measured normalized transmission amplitude and phase spectrum of a coupled waveguide-microdisk resonator (CWMR) structure at wavelengths

close to the resonance wavelength of the microdisk resonator. In this structure, the coupling between the desired mode in the microdisk resonator and the waveguide mode is adjusted to achieve critical-coupling between the waveguide and microdisk resonator modes. The microdisk resonator used in this measurement has a mode with an intrinsic Q (Q_i) of 1.86 million (loaded Q of 0.93 M). The measured phase response spectrum of this device corresponds to the under-coupling regime (Figure 3.2(b)); therefore, the waveguide-microdisk resonator coupling Q (Q_c) in this structure is slightly larger than Q_i. The off-resonance variations in the transmission amplitude and phase spectrum are caused by the Fabry-Perot (FP) resonances, due to the reflections at the cleaved waveguide facets. The reference measurement, taken with a reference sample is used to model and compensate the effects of the optical path length, dispersion, and polarization mode dispersion (PMD) differences between the two arms of the interferometer on the measured phase spectrum.

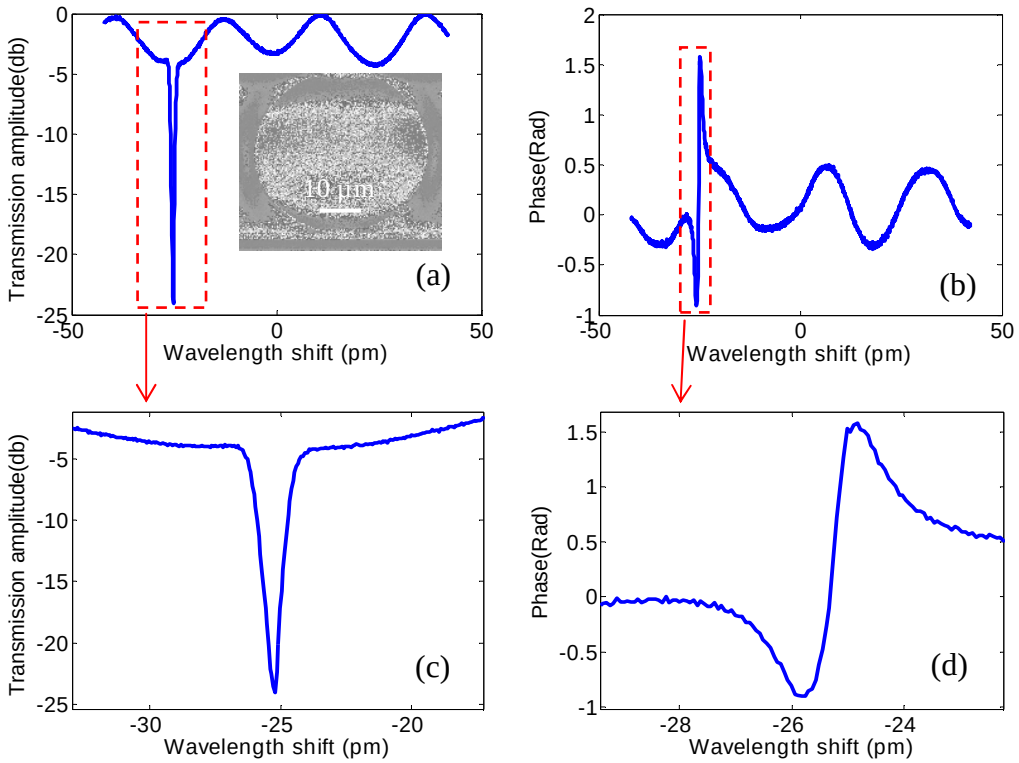

Figure 3.2: Characterization of the transmission amplitude and phase of a CWMR at close to critical-coupling regime. (a), (c): Transmission amplitude. (b), (d): Transmission phase. The center wavelength is 1549.2nm. The inset in the figure (a) shows the SEM of the microdisk resonator.

3.1.3 Near-field imaging of the optical modes in photonic structures

The developed experimental setup is used to characterize the near-field optical signal in different samples. Figure 3.3 shows the measurement results for a coupled resonator waveguide (CROW) filter. Figure 3.3(a) shows the SEM image of a CROW-based filter, fabricated by cascading four racetrack resonators. The phase and amplitude of the light in the coupling region between the input waveguide and the racetrack resonator are of interest for complete characterization of this device. An NSOM tip, with a 100 nm aperture size, is used to measure the near-field amplitude and phase in this region. A complete two-dimensional scan is done. The two red arrows in Figure 3.3(a) show the x-scan and y-scan profiles, extracted from the two-dimensional scan, along the fast and

slow scanning directions. Figure 3.3(b) shows the topography profile of the racetrack and the waveguide, separated by a 120 nm gap, along the x-scan. Figure 3.3(c) shows the field intensity profile along the x-scan direction. The input laser wavelength is selected to be in the pass band of the CROW filter. Figure 3.3(c) clearly shows the field enhancement in the racetrack resonator.

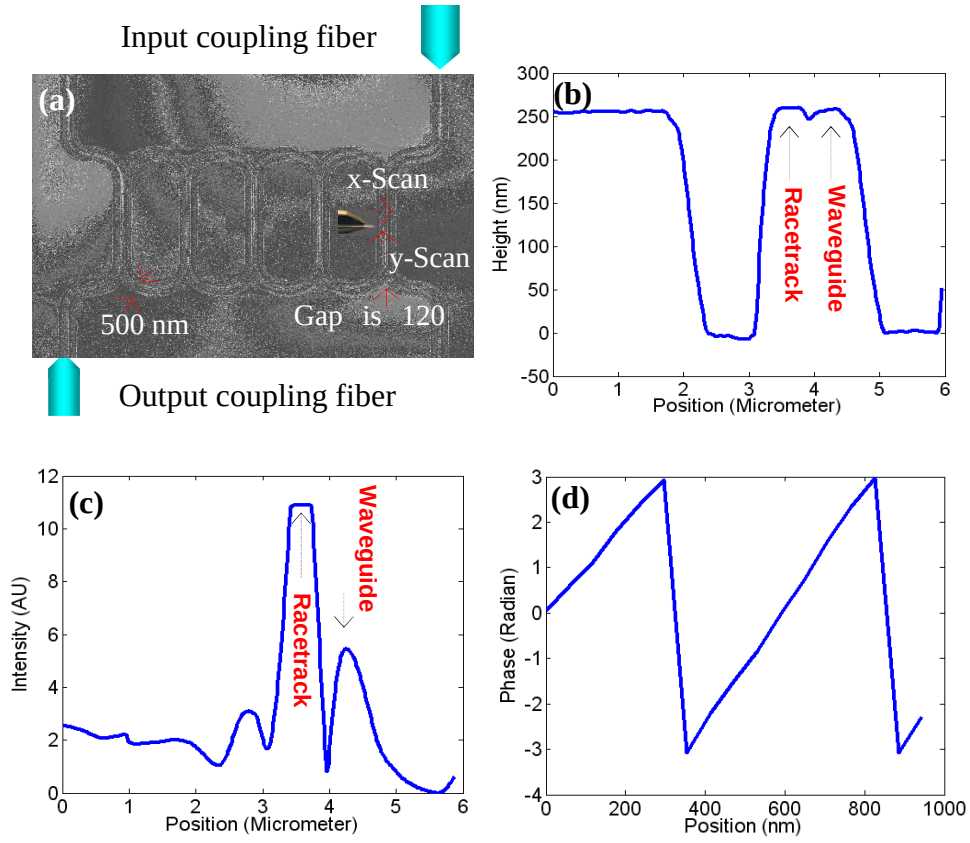

Figure 3.3: Near-field characterization of a CROW structure. (a) SEM picture of the characterized structure with input and output coupling fibers schematically shown. The x-scan shows the scanning path for figures (b) and (c) and y-scan shows the scanning path for figure (c). (b) The measured topography profile in x-scan path. The gap between waveguide and racetrack resonator can not be completely resolved and is measured as a deep between racetrack and waveguide regions. (c) Field intensity profile measured in the x-scan direction at λ= 1570 nm. (d) Phase of the near-field signal measured along y-scan direction.

The maximum coupled power to the NSOM tip, in this case, was about 55 dB less than the power inside the waveguide. The light collection efficiency through the NSOM aperture depends on many different parameters, including the field intensity at the tip

position, the size of the tip aperture, and the polarization of the light of the excited optical modes. Figure 3.3(d) shows the measured phase along the y-scan direction.

3.1.4 Near-field characterization of microdisk resonator modes

The high-Q and small mode volume of microdisk resonators have made them very attractive for a wide variety of applications, including sensing, nonlinear optics, low threshold lasing, and resonator quantum electrodynamics (QED) [56]. In most of these applications, where the interaction of the optical modes of the micro resonator and an external perturbation at the proximity of the resonator is required, knowing the near-field profile of the resonator mode is essential. We have used the NSOM system to directly image the mode profile of a microdisk resonator, side coupled to a single-mode waveguide. In this experiment, we first measure the transmission of the CWMR system to find the exact resonance wavelength of the desired mode. Then, the tunable laser wavelength is tuned to the resonance wavelength of the desired mode and the mode profile is measured.

The high-Q microdisk resonators characterized in this work are fabricated on a silicon-on-isolator (SOI) wafer using E-beam lithography and inductive coupled plasma (ICP) dry etching [29]. The structure is fabricated on an SOI wafer with a 220 nm-thick top layer silicon and a 1µm buried oxide (BOX) layer. Figure 3.4(a) shows the SEM image of the microdisk resonator. Figure 3.4(b) shows the transmission spectrum of the microdisk resonator over a narrow bandwidth around one of its resonance wavelengths. The CWMR has two high-Q modes at around 1556.25 nm. These two modes are the result of mixing (i.e., splitting) of the inherently degenerated CW and CCW modes in the resonator by the microdisk resonator surface roughness. The laser light is coupled to the

input waveguide and is tuned to the resonance wavelength of the microdisk resonator at λ=1556.2561nm. The intrinsic Q (Q_i) of this mode is about 1.8 M. In this experiment, a metal-coated NSOM tip, with an aperture size of 100 nm, is used to collect enough power from the surface of the microdisk resonator. The top microscope image of the microdisk resonator, with the NSOM tip in contact with the surface of the microdisk resonator, is shown in Figure 3.4(c). Figure 3.4(d) shows the topography image of the scanned part of the CWMR. Figure 3.4(e) and Figure 3.4(f) show the measured electric field intensity and phase of the resonator mode on the top of the structure. The measured field intensity pattern [Figure 3.4(e)] illustrates the standing wave, caused by the interference of the CW and CCW components of the split mode.

The measured field intensity pattern in Figure 3.4(e) corresponds to a first-order radial mode. However, there are still some artifacts in the intensity image, which can be attributed to the slight coupling to higher-order modes in the microdisk resonator.

The integration time for each measurement point in this experiment is 10 milliseconds. Therefore, it takes about 40 minutes to take a 512 by 512-pixel image. The variations in the environmental parameters (e.g., thermal fluctuations) result in a random drift in the laser source wavelength and the resonance wavelength of the microdisk over time. Because of the relatively long imaging time and high-Q of the microdisk resonator, a small drift in the laser source wavelength may lead to the detuning of the input laser from the microdisk resonance wavelength. Figure 3.4(e) shows the variations in the near-field amplitude, caused by the slight laser detuning.

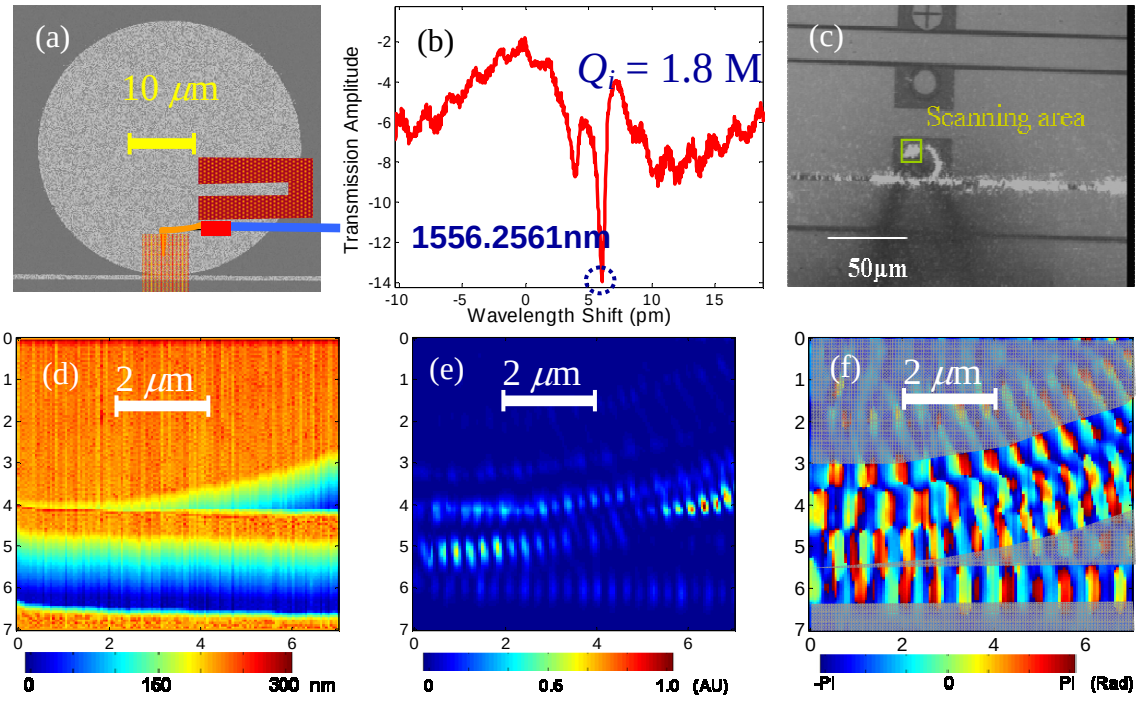

Figure 3.4: Near-field characterization of Microdisk resonator. (a) The SEM image of the microdisk resonator. The diameter of the microdisk resonator, the width of the waveguide, and the size of the gap between waveguide and the resonator are 40 µm, 400nm, and 150nm, respectively. (b) Normalized transmission of the CWMR resonator system around 1552.62nm wavelength in dB scale. (c) The top microscope image of the microdisk resonator. The laser light is coupled to the input waveguide and is tuned to the resonance wavelength of the microdisk resonator. The NSOM tip is in contact with the surface of the microdisk resonator. (d) The topography image of the part of the CWMR system. (e) The map of the optical field intensity inside the waveguide and microdisk resonator. (f) The map of the field phase in the waveguide and the microdisk resonator.

3.1.5 Near-field measurements stability

Three main factors that affect the measurement accuracy of CWMRs transmission are 1) the variation in the input and output coupling, 2) the variation in the wavelength of the input laser, and 3) the variations in the resonance wavelength of the resonator, which is caused by the microdisk resonator temperature variations. The transmission of the high-Q CWMR systems is very sensitive to the input laser-resonator wavelength detuning. Therefore, the measured transmission is very sensitive to any fluctuation in the input laser wavelength and the temperature-induced variations in the resonance wavelength of the

resonator. The high thermo-optic coefficient of the Si ($dn/dT = 1.8\times10^{-4}$ /°C) results in a high temperature-induced resonance shift of about +80 pm/°C for a microdisk resonator with a diameter of 40μm at 1550 nm. As a result, for a microdisk resonator with an intrinsic Q of 1.8×10^{6} (similar to the one used in the experiment in the previous section), a temperature variation of only 0.01°C (equivalent to a resonance shift of 0.8 pm or 100 MHz) is enough to bring the input laser completely out of the resonance. Also, the tunable laser used for near-field characterization system (Agilent 81642A) has a linewidth of 100 kHz and a typical wavelength stability of 1pm (over 24 hours). Therefore, without an effective technique for temperature control or compensation and laser wavelength locking, the laser wavelength-resonator detuning fluctuations over long measurement times are significant.

3.2 High-resolution imaging of optical modes in microdisk resonator

Conventional near-field scanning optical microscopy (NSOM) techniques are based on collecting the light from the evanescent field of the optical modes through an NSOM sub-wavelength aperture. The spatial resolution of this technique is limited by the minimum size of the aperture required to couple enough power to the NSOM probe. Furthermore, in the case of high-Q resonators, the relatively large NSOM probe size significantly perturbs the optical modes of the resonator and makes it impossible to measure the actual mode profile of the resonator e. As an alternative technique, the aperture-less NSOM technique has been proposed [44, 45, 46, 47]. The aperture-less NSOM is based on the far-field collection of the light scattered from a sub-wavelength perturbation in the near-field region of the desired mode. The aperture-less NSOM technique has also been used to characterize the mode profile of the guided mode in an optical waveguide by

measuring the transmission loss of the waveguide instead of the scattered light power [48].

We present an alternative technique for the characterization of the mode profile of high-Q resonators based on the effect of a small perturbation on the transmission amplitude and phase of the CWMR system. The small perturbation in this case is a small AFM tip that scans the surface of the resonator. The perturbation of a microdisk resonator by an AFM tip affects the resonant optical modes confined in the microdisk resonator in three different ways, namely, 1) increasing the microdisk resonator loss due to the scattering and absorption through the perturbation, 2) shifting the resonance wavelength of the resonator due to the small refractive index change, and 3) coupling the degenerate CW and CCW modes inside the microdisk resonator. Although all of these factors affect the CWMR transmission amplitude and phase at the same time and their effects scale with the field intensity at the perturbation position, their effects are completely different and depend on the resonator Q, the waveguide-resonator coupling, and the detuning of the input laser wavelength from the resonance wavelength of the unperturbed resonator.

3.2.1 Modeling the effect of a small perturbation on the microdisk resonator modes

The small perturbation caused by the AFM tip can be modeled by a small dielectric perturbation on the surface of the microdisk resonator. A dielectric perturbation affects the optical mode in the resonator in several different ways. First, a small dielectric perturbation couples the optical mode in the resonator to the propagating free space modes, hence causing loss through scattering. Second, the perturbation in the refractive index of the microdisk resonator cladding changes the effective index of the mode and, therefore, causes a shift in its resonance wavelength. The shift in the resonance of the

microdisk resonator is inversely proportional to the mode volume of the microdisk resonator. Therefore, for a high-Q and small mode volume microdisk resonator, a small perturbation may cause a large resonance shift, as compared to the spectral linewidth of the microdisk resonant modes. Furthermore, the microdisk resonator has a circular symmetry and, therefore, at each resonance wavelength, supports two degenerated CW and CCW propagating modes. The presence of a small perturbation on the surface of the microdisk resonator breaks this symmetry and couples these two modes. Figure 3.5 shows a schematic of the nanoparticle induced coupling and loss for the two degenerated modes of a microdisk resonator. The effect of the small perturbation on the CW and CCW modes in the microdisk resonator can be modeled by [57, 58]

$$\begin{aligned}\frac{da_{ccw}}{dt} &= -j\delta\omega a_{ccw} - \frac{\Gamma_c}{2}a_{ccw} + j\beta(r_0)a_{ccw} + j\beta(r_0)a_{cw} - \frac{\Gamma_p(r_0)}{2}a_{ccw} + j\sqrt{\Gamma_{in}}S_{in} \\ \frac{da_{cw}}{dt} &= -j\delta\omega a_{cw} - \frac{\Gamma_c}{2}a_{cw} + j\beta(r_0)a_{cw} + j\beta(r_0)a_{ccw} - \frac{\Gamma_p(r_0)}{2}a_{cw}\end{aligned} \quad . \quad (3.7)$$

In the above equation, a_{ccw} (a_{cw}) is the amplitude of the CCW (CW) microdisk mode, $\delta\omega = \omega - \omega_0$ is the input laser detuning from the resonance frequency of the unperturbed resonator, Γ_c is the loss rate of the unperturbed microdisk resonator modes, $\beta(r_0)$ and $\Gamma_p(r_0)$ are the coupling rate between the CCW and CW mode and the loss rate of the resonator through the dielectric perturbation (at the position r_0 in respect to the resonator), Γ_{in} is the coupling rate between the guided mode in the input waveguide and the resonant modes of the microdisk resonator, and, finally, S_{in} is the amplitude of the guide mode in the input waveguide ($|S_{in}|^2 = P_{in}$, where P_{in} is the input waveguide power).

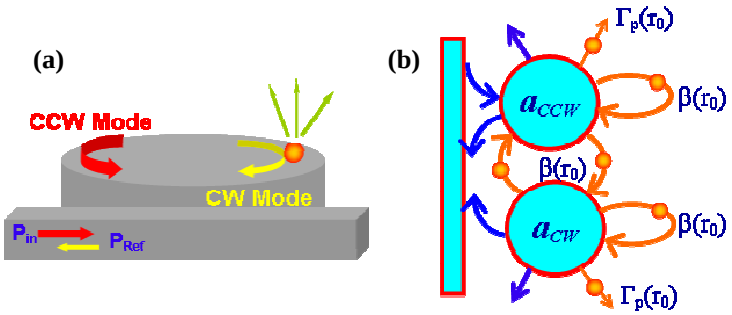

Figure 3.5: (a) An schematic of the microdisk resonator, perturbed by a nanoparticle. (b) The diagram of the nanoparticle-induced coupling and loss in a microdisk resonator with two degenerated resonant modes.

For a small dielectric particle with dimensions much smaller than the resonator resonance wavelength, the dielectric perturbation can be approximated by a single-point dipole scatterer. In this case, the perturbation-induced coupling rate between the resonant modes and the perturbation-induced loss rate in the microdisk resonator can be approximated as [59, 60]

$$\beta(r_0) = \frac{\omega\alpha_p \left|E_c(r_0)\right|^2}{2\varepsilon_c V_c \left|E_c^{\max}\right|^2}, \tag{3.8}$$

and

$$\Gamma_p(r_0) = \frac{\sigma_p c n_s \left|E_c(r_0)\right|^2}{\varepsilon_c V_c \left|E_c^{\max}\right|^2}. \tag{3.9}$$

In the above equations, α_p and σ_p are the polarizability and the scattering cross-section of the dielectric perturbation, respectively; ε_c is the microdisk resonator relative permittivity; n_s is the microdisk resonator cladding material refractive index; V_c is the microdisk resonator mode volume; and, finally, $\left|E_c(r_0)\right| / \left|E_c^{\max}\right|$ is the ratio of the electric field intensity at the perturbation location to the maximum electric field intensity in the microdisk resonator. The magnitude of the polarizability (α_p) and scattering cross-

section (σ_p) of a nanoparticle depend on the material permittivity, size, and shape of the nanoparticle. For a small spherical nanoparticle with a permittivity of ε_p and a radius of r_p, α_p and σ_p can calculated as [61]

$$\alpha_p = 4\pi \frac{\varepsilon_p - \varepsilon_s}{\varepsilon_p + 2\varepsilon_s} {r_p}^3, \tag{3.10}$$

and

$$\sigma_p = \frac{{n_s}^4 {k_0}^4}{6\pi} \left|\alpha_p\right|^2. \tag{3.11}$$

As can be inferred from Equations (3.8) to (3.11), the perturbation-induced loss to coupling ratio is proportional to the normalized volume of the nanoparticle (i.e., $\Gamma_p(r_0)/\beta(r_0) \propto (r_p/\lambda)^3$). As an example for a glass nanoparticle with a diameter of 50 nm the polarizability and the scattering cross-section are 5.38×10^{-17} cm^3 and 4.14×10^{-16} cm^2, respectively. In this case, the ratio of the perturbation-induced loss rate to the coupling rate is 1.9×10^{-4}. Therefore, for small nanoparticles, the effect of the nanoparticle scattering loss is negligible. Ignoring the effect of the nanoparticle loss, the steady-state solution for the amplitude of the CCW and CW modes inside the microdisk resonator is

$$\begin{aligned} a_{ccw} &= \frac{-j\left(j(\delta\omega - \beta(r_0)) + \Gamma_c/2\right)\sqrt{\Gamma_{in}}}{\left(j(\delta\omega - \beta(r_0)) + \Gamma_c/2\right)^2 + \beta(r_0)^2} S_{in} \\ a_{cw} &= \frac{\beta(r_0)\sqrt{\Gamma_{in}}}{\left(j(\delta\omega - \beta(r_0)) + \Gamma_c/2\right)^2 + \beta(r_0)^2} S_{in} \end{aligned}. \tag{3.12}$$

The transmission spectrum ($t(\delta\omega)$) of the perturbed CWMR system then can be calculated as

$$t(\delta\omega) = 1 - \frac{\left(j(\delta\omega - \beta(r_0)) + \Gamma_c/2\right)\Gamma_{in}}{\left(j(\delta\omega - \beta(r_0)) + \Gamma_c/2\right)^2 + \beta(r_0)^2}. \tag{3.13}$$

The transmission spectra of the perturbed CWMR in the weak-perturbation (i.e., $\beta(r_0) < \Gamma_c$) and strong-perturbation ($\beta(r_0) > \Gamma_c$) regime are depicted in Figure 3.6. As can be seen in Figure 3.6, a weak dielectric perturbation results in a small red shift in the CWMR transmission spectrum ($\Delta\omega_p = \beta(r_0)$). On the other hand, a strong perturbation results in a complete mode splitting [62].

For high-resolution imaging, we use a small AFM tip to ensure that $\beta(r_0) << \Gamma_c$ and the CWMR is in the weak perturbation regime. The spectrum transmission then can be written as

$$t(\delta\omega) \approx 1 - \frac{\Gamma_{in}}{(j(\delta\omega - \beta(r_0)) + \Gamma_c/2)} \approx t(\delta\omega) - \frac{j\Gamma_{in}\beta(r_0)}{(j\ \delta\omega + \Gamma_c/2)^2}. \tag{3.14}$$

The perturbation-induced changes in the transmission power ($\delta|t(\delta\omega)|^2$)and phase ($\delta \prec |t(\delta\omega)|$) of the CWMR then can be written as

$$\delta|t(\delta\omega)|^2 \approx \frac{\Gamma_c^2 \delta\omega}{2(\delta\omega^2 + \Gamma_c^2/4)} \frac{\omega\alpha_p}{2\varepsilon_c V_c \left|E_c^{\max}\right|^2}, \tag{3.15}$$

and

$$\delta \prec t(\delta\omega) \approx \frac{\Gamma_c}{2(\delta\omega^2 + \Gamma_c^2/4)} \beta(r_0). \tag{3.16}$$

Finally, by replacing $\beta(r_0)$ in the above equation and tuning the laser input to the resonance wavelength of the microdisk resonator, we have:

$$\delta \prec t(\delta\omega) \approx \frac{Q_c\alpha_p}{\varepsilon_c V_c} \frac{\left|E_c(r_0)\right|^2}{\left|E_c^{\max}\right|^2}. \tag{3.17}$$

Although the previous analysis is done for the specific case of a microdisk resonator, for the case of small perturbation the same result can be drawn for any resonator. In

general, the effect of a weak perturbation on a resonator can be modeled by a small red shift in the resonance spectrum of the resonator, where the shift value is proportional to the field intensity at the perturbation point.

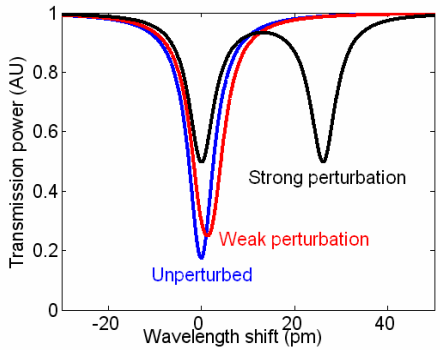

Figure 3.6: The effect of a small perturbation on the transmission spectrum of a coupled waveguide-microdisk resonator structure. The blue, red, and black curves correspond to the unperturbed, weakly-perturbed, and strongly-perturbed conditions, respectively.

3.2.2 Experimental demonstration

To experimentally investigate the effect of a small perturbation on the optical modes in a microresonator, a microdisk resonator with a diameter of 40 μm is fabricated on an SOI substrate. The thickness of the silicon slab layer is 230 nm. The light is coupled to the microdisk resonator through a pulley coupler [63]. The width of the waveguide, the gap between the waveguide and the microdisk, and the waveguide-microdisk resonator coupling length are 500 nm, 400 nm, and 60 μm, respectively. Figure 3.7(a) shows the schematic of the system. The unperturbed CWMR has a resonant mode at λ=1545.39 nm with a loaded Q of 100,000. A 100 nm metal-coated AFM tip is used to scan the surface of the microdisk resonator in the radial direction. The full transmission spectrum of the CWMR is measured at each AFM tip position. The transmission spectra of CWMR corresponding to several different tip positions are shown in Figure 3.7(b). The normalized field intensity at each tip position is estimated from the amount of the shift of

the dip in the transmission spectrum (i.e., shift in the resonance wavelength of the microdisk resonator). Figure 3.7(c) shows the estimated near-field intensity and compares it with the field pattern of the corresponding microdisk resonator mode simulated using the finite element (FE) method.

Although collecting of the transmission spectrum at each tip position provides useful information about the microdisk resonator-AFM tip interactions, it takes a relatively long time and it is not necessary for the near-field imaging. In our near-field imaging technique, the laser wavelength is fixed at a wavelength close to the resonance wavelength of the resonator. The near-field imaging is done by monitoring the tip-induced variations in the transmission amplitude and phase at a fixed wavelength.

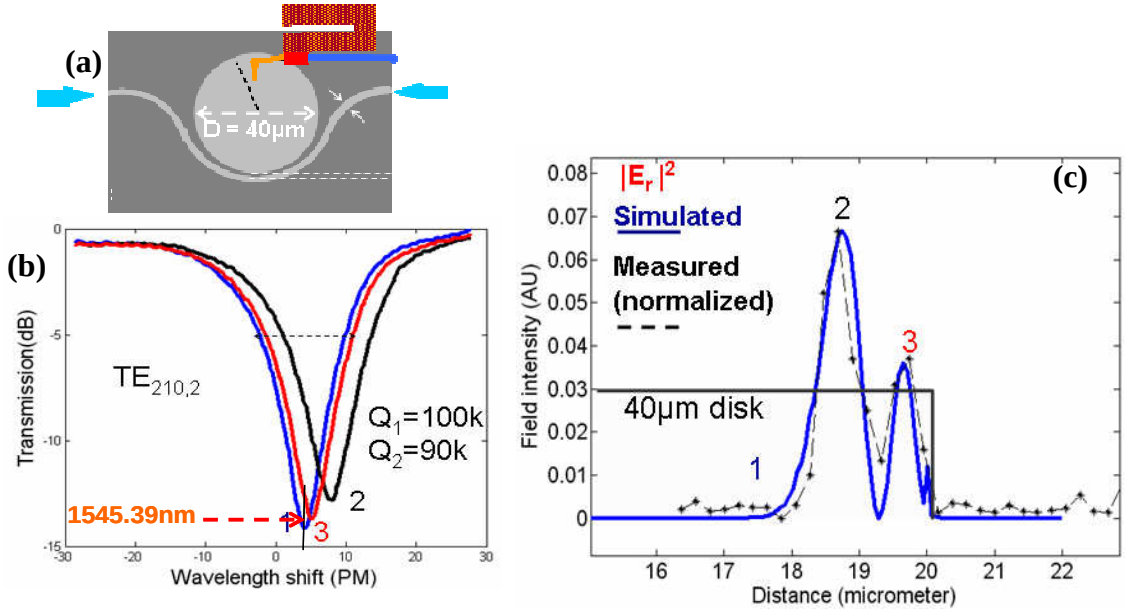

Figure 3.7: The effect of the tip perturbation on the CWMR transmission spectrum at different tip positions. (a) Schematic of the system. (b) The transmission spectrums corresponding to different tip positions. (c) The simulated (solid blue line) and measured (dashed black line) field intensity on the top surface of the microdisk resonator.

A different microdisk resonator with the same diameter (i.e., 40 μm) is used for this experiment. Figure 3.8 shows the transmission and phase spectra of the microdisk

resonator for TE polarization (i.e., the main component of the E field is in the resonator radial direction) in a small wavelength range around the microdisk resonance mode at λ=1529.71 nm. The resonant mode of the unperturbed resonator has a loaded *Q* (i.e., *Q* after coupling to the waveguide) of 233,000, corresponding to a resonance linewidth of 6.56 pm. The measured transmission phase spectra correspond to the under-coupled regime where the coupling *Q* (i.e., Q_c=796,000) is larger than the intrinsic *Q* (i.e., Q_i =329,000). The resonator mode is perturbed by a small AFM tip with a diameter of 20 nm and a tapering angle of 20 degrees [64]. The input laser is initially 0.85 pm red shifted with respect to the microdisk resonator resonant mode.

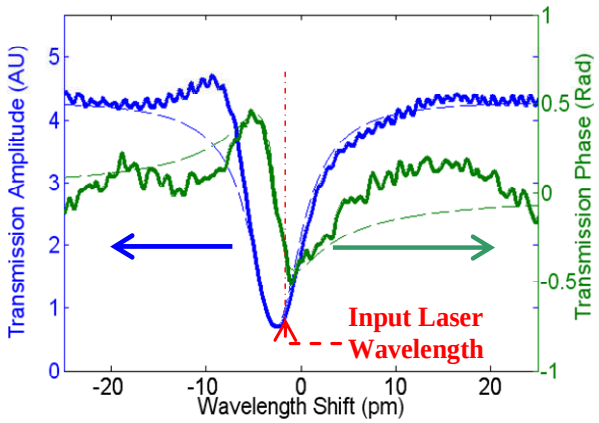

Figure 3.8: Solid (dashed) lines show measured (simulated) transmission amplitude (right) and phase (left) of the CWMR without the AFM tip perturbation.

Figure 3.9 shows the change in the transmission phase and amplitude of the CWMR as the AFM tip scans the surface of the microdisk resonator in the radial direction. The interaction between the AFM tip and the optical mode in the microdisk resonator depends on the electrical field intensity at the tip position. As can be seen from Figure 3.9, the resonant mode is a fourth-order radial mode. Considering the fact that the input laser is red shifted with respect to the unperturbed resonant mode of the microdisk resonator

(refer to Figure 3.8), the changes in the transmission amplitude and phase are mainly contributed by a red shift in the resonant mode of the resonator. The amount of the wavelength shift can be calculated from both amplitude and phase responses and in both cases results in very similar shifts of about 1.25 pm.

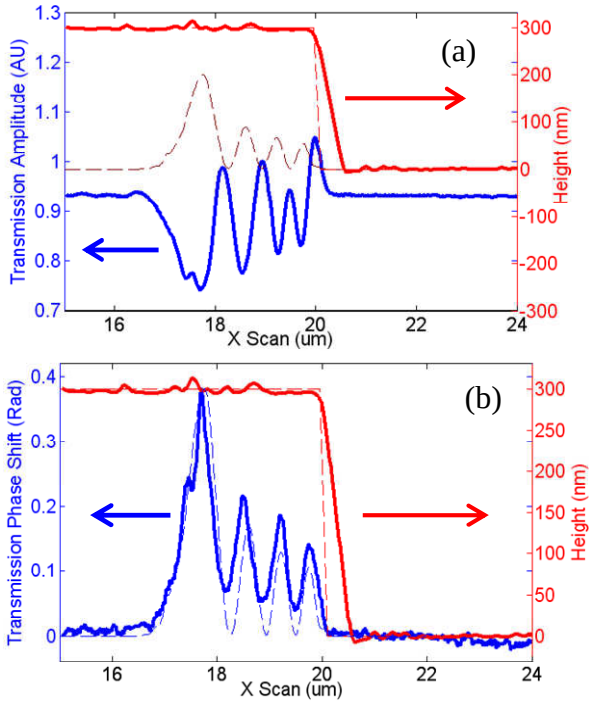

Figure 3.9: Solid blue lines (left) show the transmission amplitude (a) and phase (b) of the CWMR as the AFM tips scan the microdisk resonator in the radial direction. Dashed blue lines (left) show the radial pattern of the normalized electrical field intensity. The solid (dashed) red curves (right) show the actual (ideal) AFM topography scan.

The high sensitivity of the CWMR to any perturbation on the microdisk surface enables to achieve high near-field measurement SNRs using small AFM tips with low input laser power and short integration time. The low required input power enables to characterize the high-Q resonator in linear regime and avoid nonlinear effects in the high-Q resonator. Considering the high transmission SNR, the CWMR transmission measurement accuracy is mainly limited by the drifts in the laser wavelength and the

resonance wavelength of the resonator. Nevertheless, the relatively small required integration time enables to minimize the effect of slow variations in the laser wavelength and the resonance wavelength of the resonator by temperature variations and other environmental effects. Using over measurement setup, imaging resolutions down to 20 nm are readily obtained. Another source of the noise in imaging of the optical mode profile is the variation in the distance between the AFM tip and the resonator surface. The small decay length of the evanescent field of the microresonator (~50 nm) leads to a relatively high sensitivity to any mechanically or thermally induced variation in the AFM tip-resonator surface distance. The effect of the AFM tip-resonator surface distance variations on the transmission measurements is evident from the correlation between the measured high and transmission amplitude and phase in Figure 3.9.

CHAPTER 4

Prospect of Integrated Label-Free lab-on-a-Chip Biosensing

Optical sensors based on different phenomena have attracted exponentially increasing attention in the past several years [65, 66]. Several optical techniques have been studied for biosensing applications and proven to have a relatively high sensitivity and provide short assay times [67, 68]. Principally, in these techniques, the analyte binds specifically to a capture molecule, which is immobilized on the resonator surface. These optical sensors can be divided into two main categories: 1) mass sensors, where the presence of the captured analyte is measured by detecting the change in the refractive index or absorption, and 2) fluorescence sensors, where the emission of an immobilized fluorescently labeled analyte is measured [69]. For both mass sensors and fluorescence sensors, the signal strength increases by enhancing the optical field interacting with the analyte residing on the sensor surface. For these sensing applications, Si microresonators are particularly interesting as they provide high-Q and strong field enhancement in a small interrogation volume, which makes them more sensitive to the changes in the total bound mass. Furthermore, the small size of these resonators reduces the required fluid volume (which is comparable to the resonator volume). Integrated into a microfluidic setup, thousands of such microresonators can be lined up for multi-analyte sensing within a few square millimeters of Si chip that can be mass manufactured with low-cost CMOS technology. Finally, the thin natural oxide layer on Si resonators enables the extensive

and well-established surface chemistry processes developed for glass-based biochip arrays to be adapted directly to silicon-based biosensors.

While most of the currently available commercial optical biosensors are based on fluorescent labeling, there is a significant interest in moving toward label-free sensors in which biomolecules are detected in their natural forms [65]. Special attention has been focused on optical biosensors based on the refractive index change as the sensing transduction signal. Various optical label-free biosensing platforms have been proposed, including surface plasmon resonance [70, 71, 72, 73], waveguides [74], whispering gallery mode resonators [75, 76, 77], and photonic crystals [78, 79]. A complete comparison among different label-free sensing techniques can be found in [65].

Among all the different platforms for label-free sensing, resonator-based sensors have the potential to provide the highest sensitivity. The strong light-matter interaction in the near-field of high-Q resonators results in a high sensitivity to the changes in the refractive index of the surrounding materials. In 2002, Vollmer et al. demonstrated label-free sensing based on whispering gallery modes in a stand-alone microsphere resonator [75], which provided the sensitivity to detect a single DNA molecule. Despite the relatively large size and small refractive index unit (RIU) sensitivity of the microsphere resonators, their ultra-high-Q has enabled to achieve mass sensitivities down to single molecule detection [80, 81, 82, 83, 84]. Single molecule label-free sensing based on the thermo-optic effects has also been achieved using ultra-high-Q microtoroid resonators, which provide concentration sensitivity in the range of a few attomolar [85].

Although photonic crystal (PC) resonators usually have Qs smaller than the Qs of microsphere and microtoroid resonators, the ultra-small mode volume of PCs results in a

high mass sensitivity of the PC label-free sensors. Single particle sensitivity, for the gold nanoparticles with a diameter as small as 10 nm, has been demonstrated using PC resonators [79]. The main advantages of the biosensors based on PC resonators are their small size and their compatibility with large-scale integration. This makes it possible to fabricate an array of resonator-based sensors on the same chip. This chip can be used for parallel sensing of multiple analytes [86, 87].

Among all resonator-based biosensors, microring-based sensors have attracted the most attention [88, 89, 90, 91]. The relatively small size, relatively high-Q, and relatively high RIU sensitivity of microring resonators, in addition to their compatibility with large-scale fabrication and multiplexed sensing, has made them the preferred choice for many applications. As an alternative to conventional microring resonators, slot-microring resonators are proposed to achieve a higher RIU sensitivity [92]. An RIU sensitivity of 298 nm/RIU has been obtained for a slot-microring (as compared to 70 nm/RIU for conventional microrings); however, this improvement comes at the price of a reduction in the resonator quality factor.

One of the main advantages of the integrated photonic sensors is the possibility of multiplexing a large number of sensors on the same chip in a small foot print. A multiplexed label-free sensor can be used to study the interactions between the bio-molecules in input analyte with those immobilized on the sensor surface. This, not only has applications in the sensing in areas, such as point-of-care (POC) diagnosis, detection of hazardous materials for homeland security applications, and environmental and food safety testing, but also provides a platform for investigation of molecular interactions, which are the key technology for the drug discovery. The study of biomolecular

interaction finds applications in many different fields. The performance of a multiplexed-label-free sensor is evaluated based on several different criteria, including the degree of multiplexability (i.e., the maximum number of sensor that can be integrated on the same device) sensor sensitivity, resolution, limit-of-detection (LOD), selectivity, dynamic range, and throughput. Different other parameters, such as the sensor size, weight, and power consumption; the cost of the sensor and the cost per test; and the required sample volume for each test are also important.

In this chapter, I review the basic concepts and achievable performance of the resonator-based label-free sensors. I also present the basic concepts that determine the efficiency of sample delivery to the sensor surface and provide a basic design for the required microfluidic system. I also experimentally study the efficiency of our experimental setup for characterization of the resonance wavelength shift in the sensing resonators and provide some solutions for the improvement of the resonance shift measurement accuracy based on comparison of the sensing elements with on-chip reference resonators. Finally, I provide some initial experimental results for bulk refractive index sensing and biomolecule binding detection using compact microdisk resonators.

4.1 Resonance-enhanced refractive index sensing

A resonator-based refractive index sensor is a label-free sensor that detects the target analytes by monitoring the changes in the resonance wavelength of the resonator, caused by the analyte binding to the resonator surface. High-Q resonators provide high sensitivity to the changes in the refractive index of their surrounding environment, as a small shift in their resonance wavelength leads to a considerable change in their

transmission characteristics, at wavelengths close to the resonator resonance wavelength. A resonant-based refractive index sensor in its simplest form is a waveguide-coupled resonator or a mach-zehnder (MZ) interferometer with a resonator coupled to one or both its arms. Figure 4.1 shows the schematic of a resonator-based refractive index sensor. The shift in the resonance wavelength manifests itself in the changes in the transmission of the sensor device and can be estimated by measuring the changes in the transmission of the sensor device at a certain wavelength or over a range of wavelengths.

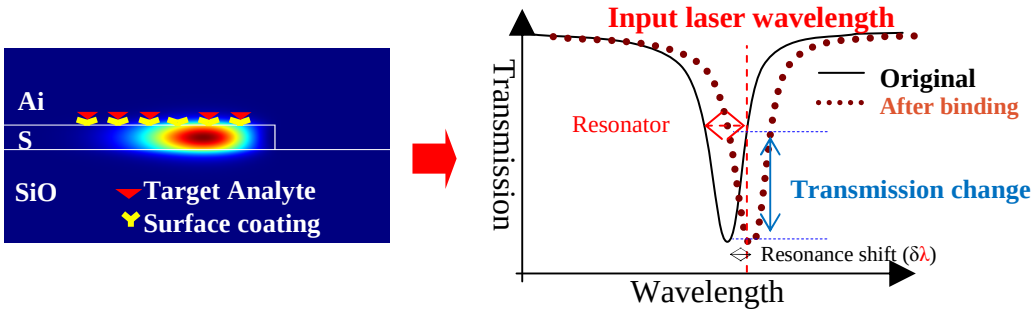

Figure 4.1: Schematic of the refractive index sensing by measurement of the resonance shift of a resonator caused by the analyte binding to the resonator surface. By biasing the input laser at wavelength with maximum transmission slop, a small shift in the resonance wavelength of the high-Q resonator translates to a large change in the transmission amplitude.

The resonator refractive index sensitivity is usually referred to the bulk refractive index sensitivity, which is quantified by the ratio of the shift in the resonator to the change in the refractive index of the cladding (e.g., nm/RIU). The bulk refractive index sensitivity depends on the ratio of the resonant mode of resonator resonant mode field energy in the cladding material to the total resonator stored energy. However, in the sensors based on the surface sensing, the sensor LOD is determined by the sensor surface refractive index sensitivity, which is the change in the resonator wavelength caused by the change in the refractive index of a thin film on top of the sensor. The sensitivity in this case depends on the field intensity on the resonator surface rather than the total field

energy in the cladding material. The large vertical field confinement in the resonators in thin SOIs enables to achieve a large refractive index contrast as compared to lower refractive index material platforms such as doped oxide and SiN on oxide.

Figure 4.2 shows the refractive index sensitivity of the first two radial order mode TE-polarized and the first-radial-order TM-polarized resonant modes of microdisk resonators with different diameters, at resonance wavelengths close to 1550nm. As is evident form this figure, for both polarizations, microdisk resonators with smaller diameters provide higher refractive index sensitivities as compared to the microdisk resonator with larger diameters. Furthermore, TM-polarized modes provide higher refractive index sensitivities as compared to TE-polarized mode, since they have a larger portion of their energy in the cladding material.

Table 1 compares the refractive index sensitivity for several different resonator types, dimensions, and polarizations. The numbers in Table 1 are calculated using FEM simulation for sensors designed for IR wavelengths at around 1.55 μm. The surface refractive index sensitivity is defined as the shift in the resonator resonance wavelength (in nm unit) caused by a thin layer of coating material on the sensor surface with a thickness of 1nm per unit refractive index difference between the coated material and the fluidic cladding material. As it is evident from this table, while SiN resonators provide a higher bulk refractive index sensitivity for the TM-polarized resonant mode. The higher confinement in the Si microdisk resonators results in a higher surface refractive index sensitivity in these resonators as compared to their SiN counterpart.

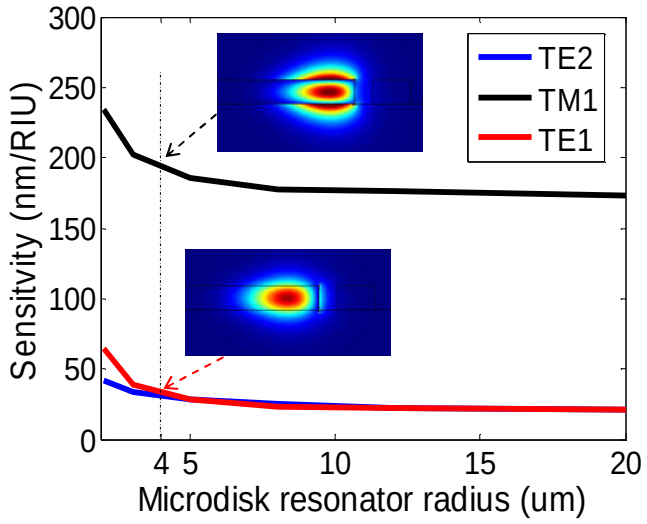

Figure 4.2: Refractive index sensitivity for the first two radial-order-mode TE-polarized and the first-radial-order TM-polarized resonant modes of a microdisk resonator at resonance wavelength close to 1550nm. The inset figures show the simulated electric-field distribution of the first radial-order-mode TE-polarized and TM-polarized resonant modes of a 4μm diameter Si microdisk resonator with a thickness of 230 nm on oxide substrate and with water cladding.

The figure of merit (FOM) of the resonator-based refractive index sensors is commonly defined as the ratio of the bulk refractive index sensitivity to the resonator resonance linewidth. The relatively high refractive index sensitivity of Si and SiN microdisk resonators, especially for TM-polarized resonant modes and the high Qs (Qs > 10^5 [24]) that can be achieved using this resonator enable to achieve very high FOMs (FOMs > 10^4).

Table 1: Comparison of refractive index sensitivity of different resonator structures

Resonator type	Resonator radius (um), Thickness (nm),Width (nm)	Polarization	Bulk refractive index sensitivity (nm/RIU)	Surface refractive index sensitivity (nm/nm/RIU)	FSR (nm)
Si Microdisk	2,220	TE	41.5	0.52	54
Si Microdisk	5, 220	TE	28.1		23
Si Microdisk	5, 220	TM	185.0		22
Si Microdisk	8, 220	TE	25.9	0.41	15
Si Microdisk	8, 220	TM	179.2	1.8	13.5
SiN Microdisk	8, 400	TE	103.9	0.67	24
SiN Microdisk	8, 400	TM	286.0	1.45	25
Si slot ring	20, 230 (500, 100)	TE	495.0		7.5
Si Microring	4, 220 (400)	TE	81	1.1	
Si Microring	20, 230 (500)	TE	59.0		4.8
Si Microring	20, 230 (500)	TM	219.0		5.3

4.1.1 Multiplexed refractive index sensing

The small footprint of the resonator-based refractive index sensors enables to develop highly-multiplexed refractive index sensors by integrating a large number of resonator-based sensors on the same chip. This multiplexing can be done either in spectral or in spatial domain. In spectral domain multiplexing, many microresonators, each with a different resonance wavelength, are coupled to the same input waveguide to form a resonator array. Each individual resonator in the array can be interrogated independently by monitoring the sensor device transmission at its corresponding wavelength range. Figure 4.3 shows the schematic of a multiplexed refractive index sensor composed of several different resonator, each at a different resonator wavelength, coupled to a common interrogating waveguide. The resonant wavelength of each resonator is adjusted by tailoring their geometry (i.e., inner and outer radiuses). Each resonator is coated with a different surface coating to specifically detect a certain analyte.

In the spatial domain multiplexing, an array of separate waveguide-coupled resonators is used. The resonator in this case can be designed to have similar resonance wavelengths. In this case, to interrogate each sensor, the output signal of its corresponding waveguide should be measured. The main advantage of the spectral domain multiplexing is that all sensing elements can be interrogated using a single pair of input and output; however, the maximum number of sensing channels that can be multiplexed in spectral domain is limited by the required resonance wavelength shift dynamic range of each sensing channel form one hand and the maximum FSR of the resonators in the array. The large single mode FSR of high-Q and compact microdisk resonators enables to achieve a large multiplexing degree. For example, using microdisk

resonators with a radius of 2μm and an FSR of ~ 54 nm, and assuming a maximum required resonance wavelength shift dynamic range of 600 pm, up to 90 different channel can be multiplexed on the same waveguide. A larger multiplexing degree can be obtained by combining spectral and spatial multiplexing.

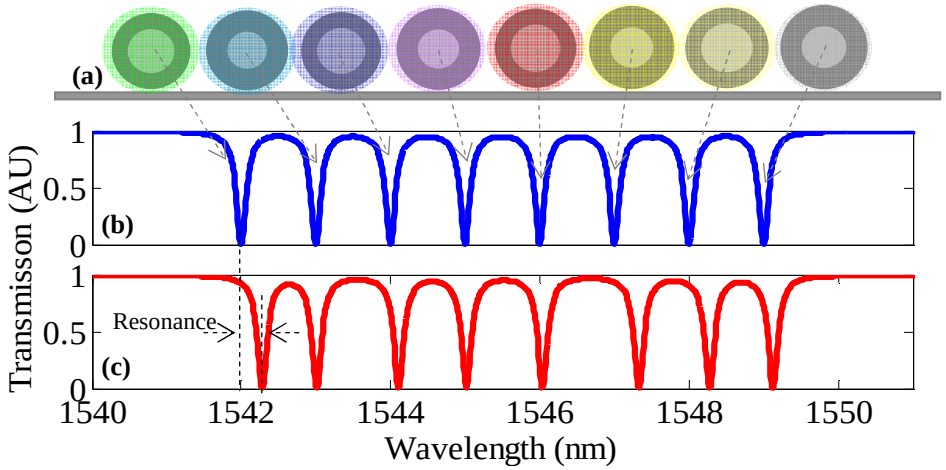

Figure 4.3: (a) Schematic of a multiplexed refractive index sensor composed of several different resonator, each at a different resonator wavelength, coupled to a common interrogating waveguide. The resonant wavelength of each resonator is adjusted by tailoring its geometry (i.e., inner and outer radiuses). Each resonator is coated with a different surface coating to specifically detect a certain analyte. (b) and (c) The transmission spectrum of the resonator array before and after exposing to the target input sample.

4.1.2 Sensitivity analysis

The LOD of detection of a resonator-based refractive index sensor is usually quantified either by the minimum detectable concentration of the desired molecule in the input analyte in the ng/mL or nano Molar units, or by the minimum detectable mass density bound to the sensor surface in pg/mm^2 unit. The second measure has the advantage that is independent of the surface coating performance and provides a fair measure for the comparison of different sensor devices. The limit of detection of a resonator-based refractive index sensor depends on different parameters including the resonator shift sensitivity to refractive index, the minimum detectable resonance shift that by itself

depends on the resonator Q, the measurement SNR, the input laser stability, and the variation in the refractive index of the resonator caused by undesired factors such as thermal variations.

The variation in the transmission power (ΔP_{out}) caused by a small change in the resonance wavelength is proportional with the resonator Q and we have:

$$\Delta P_{out} = \frac{\delta\lambda}{0.5\Delta\lambda} P_{out}^{Max} + \eta = \frac{\delta\lambda}{\lambda / 2Q} P_{out}^{Max} + \eta , \tag{4.1}$$

Where $\Delta\lambda$ is the resonator linewidth, P_{out}^{Max} is the maximum output power, and η is the output signal noise Therefore, the standard deviation of the estimated wavelength shift ($\sigma_{\delta\lambda}$) can be calculated as

$$\sigma_{\delta\lambda} = \frac{\lambda}{2Q} \frac{1}{SNR_{out}\sqrt{T}} . \tag{4.2}$$

The accuracy in the measurement of the changes in the output power is limited by both the detector noise and shot noise. The maximum input power in SOI devices is limited by the thermal instability of the resonator device. The relatively high two-photon absorption and third-order (χ^3) nonlinearity in Si and the high field enhancement in the high-Q resonators lead to a relatively low power threshold for nonlinear processes. The threshold power (P_{Th}) for the thermal instabilities in a high-Q resonator on SOI platform is inversely proportional to fourth power of the loaded Q of the resonator (i.e., $P_{Th} \propto Q^{-4}$). Therefore, the sensor sensitivity should be optimized based on a trade-off between the resonator input power and the target Q of the sensor.

A typical detector (similar to the one used for experiments in this thesis, Thorlabs PDB150C) can have a maximum gain of 70 dB and an input equivalent noise of 0.3pW $Hz^{-0.5}$. Assuming a resonator input power of 100μW and an output coupling insertion loss

of 10 dB, the sensor output measurement equivalent-shot noise, at 1.55μm wavelength, will be 1.1pW $Hz^{-0.5}$. In this case, the measurement signal-to-noise-ratio is shot noise-limited. However, even with this moderate input power, an optical output SNR of about 70 dB can be obtained. Using a resonator with a moderate Q of only 10k and an output integration time of only 10 ms, a wavelength shift measurement standard deviation of 0.08 fm (i.e., a LOD of 0.4 fm with better than 99% detection probability) can be obtained. This shift measurement accuracy is much higher than the typical laser wavelength stability and thermally-induced variations in the resonator resonance wavelength of the resonator, which are both independent of the input power and the resonator Q. Using a thermo-electric cool (TEC) stage the temperature of the resonator can be stabilized with in 1m°C of the target temperature. However, even this much variation results in a resonance wavelength variation in the other of 80 fm which is three orders of magnitude higher than the calculated wavelength shift measurement standard deviation. Also, the slow binding kinetics in refractive index sensors based on surface binding usually results in long measurement time (e.g., 20 minutes to a few hours). With this long measurement time, the long-time laser stability will also affect the shift measurement accuracy. A typical laser (Tunable laser) has a long-term wavelength variation of about 1pm/24 hour. This corresponds to a wavelength variation of more than 100 fm over a measurement time of only 20 minutes.

The mass sensitivity (S_M) for protein detection can be simply calculated from the sensor minimum detectable wavelength shift (δλ) and its surface refractive index sensitivity ($\partial\lambda/\partial d$, where d is thickness of added layer of material on top of the resonator with a refractive index similar to that of the protein, i.e., $n_L=1.45$), $S_M = \rho_p \delta\lambda/(\partial\lambda/\partial d)$

where ρ_p is the density of the protein (ρ_p = 1.3g/cm^3). As an example, for a sensor based on a 8 μm-diameter microdisk resonator, the surface refractive index sensitivity (i.e., $\partial\lambda / \partial d$) of the first- order TE and TM modes are 49 pm/nm and 216 pm/nm, respectively. Assuming $\delta\lambda=10fm$, the sensor mass sensitivity will be 26 pg/cm^2 and 6.0 pg/cm^2, respectively. For a typical surface coating kinetics ($K_{on}=2.5\times10^5 M^{-1}s^{-1}$, $K_{off}=10^{-3}s^{-1}$, $C_{S0}=2\times10^{12}\ cm^{-2}$) this corresponds to a concentration sensitivity of 32.0 pg/ml and 7.3 pg/ml, respectively.

As we already discussed, the performance of the resonator-based refractive index sensors is primarily limited by the effect of the thermal variation and the laser instability on the measurement sensitivity. In a multiplexed sensing platform, one solution to minimize these effects is to use a differential sensing device. In this architecture, the shifts in the resonance wavelength of the sensing resonators are compared with a series of reference resonators on the same platform. The surface of the reference resonators can be coated with alternative coatings that do not specifically bind with any molecule in the input analytes or is saturated with a buffer input. In this architecture, the relative resonance wavelength shifts of the sensing and reference resonators indicate the amount of the shift in the sensing resonators caused by the analyte attachment. In a multiplexed sensing platform, to minimize the relative wavelength estimation error, a series of reference sensing resonators are scrambled with the sensing elements in the spectral frequency domain. At each laser scan, the reference resonators will be used to estimate the laser-resonators differential wavelength, bias, drift, and drift rate and the sensing resonators measurement will be calibrated based on these measurements. This calibration enables to compensate for any wavelength variations caused by the combined effect of

the input laser wavelength instability and thermal resonance wavelength shifts that has a dynamics slower than the tunable laser scanning rate.

4.2 Sample delivery and binding kinetics

The performance of a refractive index sensor for biosensing applications not only depends on the sensor sensitivity, but also depends on the rate of biomolecule migration to the sensor surface. In this section, we study the dynamics of the biomolecule migration and binding to sensor surface in a fluidic environment.

The biomolecules reaction with the sensor is a reversible binding process that is governed by the rate equation:

$$\frac{\partial C_s}{\partial t} = K_{on} C_w (C_{s0} - C_s) - K_{off} C_s , \tag{4.3}$$

where C_s is the bound biomolecules density on the sensor surface, C_w is the analyte concentration in the microfluidic channel close to the sensor surface, and C_{s0} is the binding site density on the surface sensor. Also, K_{on} and K_{off} are the binding molecules association and dissociation rate constants with the $M^{-1}s^{-1}$ and s^{-1} units, respectively. At the equilibrium condition, the density of bound molecules (C_s) can be calculated as

$$C_s(\infty) = \frac{K_{on} C_w C_{s0}}{K_{on} C_w + K_{off}} = \frac{C_w / K_D}{1 + C_w / K_D} C_{s0} , \tag{4.4}$$

where $K_D = (K_{off} / K_{on})$ is the equilibrium dissociation constant with the molar (M) unit and is equivalent to the analyte concentration, where half of the binding sites on the surface are field with the bound molecules. If $C_w << K_D$ the number of bound molecules to the surface in the steady state condition is proportional to the input analyte concentration. On the other hand, if $Cw >> K_D$, all the surface binding sites will be filled and the sensor response will saturate. The binding time constant (τ) also depends on the C_w

($\tau = (K_{on}C_w + K_{off})^{-1}$). Figure 4.4 shows resonant shift response of a microdisk resonator sensor to the input analyte with different concentrations.

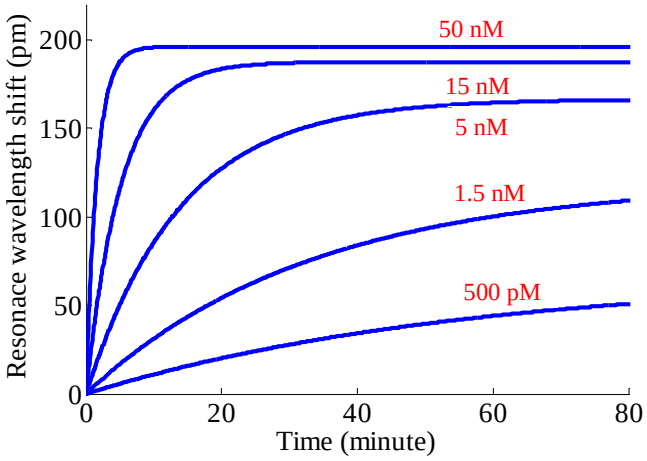

Figure 4.4: The resonance wavelength shit caused by the analyte binding to the surface a compact 2-μm diameter microdisk resonator with a TE-polarized resonant mode at round 1550 nm, for different input analyte concentrations. In this simulation, K_{on}, K_{off}, C_{s0} are $2\times10^{5}M^{-1}s^{-1}$, $10^{-3}s^{-1}$, and $2\times10^{12}\ cm^{-2}$, respectively. In this simulation we have assumed that the concentration of the analyte at the surface of the resonator remains constant.

The binding rate to the sensor surface not only depends on the binding kinetics, but also depends on the molecules migration to the surface sensor in the fluid environment. The analyte transport in the fluid environment is generally governed by the following transport equation [93]:

$$\frac{\partial C_w}{\partial t} = \nabla.(-D\nabla C_w + \bar{\nu}\, C_w) + R, \tag{4.5}$$

where D is the diffusion constant of the target molecules in the fluid, $\bar{\nu}$ is the velocity vector profile of the fluid, and R is the rate of the analyte generation or annihilation. The main transport mechanisms for the migration of the molecules to the sensor surface are through the convection and diffusion processes. The sample delivery to the sensor surface may be done using a simple reservoir, where the analyte transport will be completely through diffusion process or through a microfluidic channel where the input sample is

flown toward the sensor surface to expedite the analyte transport by convection process. In a reservoir environment, the binding of the molecules to the sensor surface depletes the sensor surrounding form the free molecules. This results in a reduction of analyte concentration in the sensor surface proximity. This vacancy then is filled by molecules diffusing toward sensor surface from other areas.

4.2.1 Diffusion versus binding kinetics

The reaction of the input analyte with the immobilized molecules on the surface (surface coating) usually has a slow kinetics (especially at low input analyte concentrations). However, in many cases, the binding process is even slower as it is limited by the rate of analyte diffusion to the sensor surface rather than the surface reaction rate. The surface binding reaction and diffusion limitations on the sensor response can be simply evaluated by comparing the diffusion and binding time constants.

Assuming a uniform concentration in an analyte reservoir over the sensor (assuming a fast diffusion), the binding reaction time constant can be calculated as $\tau_r = (K_{on}C_w + K_{off})^{-1}$. On the other hand the diffusion time constant can be calculated as $\tau_D = h^2 / D$, where h ($h = Cs(\infty)/C_w$) is the equivalent height of the fluid that contains the number of analytes equivalent to the number of final bound molecules on the sensor. For a typical protein-antibody interaction ($K_{on}=2.5\times10^5 M^{-1}s^{-1}$, $K_{off}=10^{-3}s^{-1}$, $C_{S0}=2\times10^{12}$ cm^{-2}, $D=100$ $\mu m^2/s$), and input analyte concentration equivalent to K_D ($C_w=4nM$), the reaction and diffusion time constants (i.e., τ_r and τ_D), are $500s$ and $1.72\times10^5 s$ (i.e., two days) , respectively. This means that, for a sensor in a fluid reservoir, the binding process is highly diffusion-limited. The condition becomes even worse in lower analyte

concentrations; therefore, there is a need for a mechanism to bring the input analyte to the sensor surface in faster rates.

4.2.2 Design of the micro-fluidic channel for sample delivery to the sensor surface

To achieve the optimal sensor response a model should include the effect of all playing processes, namely, reaction kinetics, diffusion, and convection to optimize the rate of the analyte attachment to the sensor surface.

The main design goals in the design of a microfluidic channel is to increase the rate of the molecules attachment to the senor surface to minimize the total assay time required for sensing and also to minimize the total required sample volume by maximizing the probability of the analyte attachment to the sensor surface. We assume a pressure-driven incompressible flow in a micro-fluidic channel with a height and width of h and w, respectively, where $w>>h$.

The limitations on the binding rate in a microfluidic channel can be evaluated by comparing the time for different interplaying process. At low analyte concentrations, the ratio of the analyte diffusion time across (from top to bottom) the channel (h^2/D) to the time constant of analyte depletion in the channel by surface binding ($h/K_{on}C_{s0}$) is called Damköhler number (Da) [93], $D_a = K_{on}C_{s0}h/D$. When $Da>>1$, the binding process is strongly diffusion limited. On the other hand, when $Da<1$, the binding process becomes surface reaction-limited; therefore, further reduction of the microfluidic channel height (h) does not improve the binding process. For the typical binding kinetics, the microfluidic channel height that correspond to the $Da=1$ (i.e., $h = D/K_{on}C_{s0}$) is much smaller than the typical microfluidic channel heights and, therefore, even in a microfluidic channel the binding process is usually diffusion limited (i.e., $Da>>1$).

In a microfluidic channel, convection is used to flow the analyte close to the sensor surface to reduce the analyte diffusion time. However, the analyte should get enough time over sensor to diffuse to the sensor surface rather than flying over the sensor in the microfluidic channel. Assuming an overall flow rate of *Q*, the average time for an analyte to pass over the sensor (τ_c) in the microfluidic channel is L/U_0, where $U_0=Q/wh$ is the average fluid velocity in the microfluidic channel. The ratio of the analyte diffusion time across the channel to the analyte convection time over the sensor can be found as

$$\frac{\tau_D}{\tau_c} = \frac{h^2 / D}{Lwh / Q} = \frac{1}{\lambda} Pe_H , \tag{4.6}$$

where $\lambda = L / h$ is the length of the sensor normalized to the microfluidic channel height and $Pe_H = Q / wD$ is Péclet constant. If $Pe_H >> \lambda$, the analyte will be swept from the sensor area before it gets the chance to migrate toward the sensor surface. Therefore, the binding process will be diffusion-limited and only a small fraction of the input analytes will be captured on the sensor surface. On the other hand, if $Pe_H << \lambda$, the binding will be transport-limited. A very small Pe_H enables a large analyte collection efficiency, but in the expense of a very long assay time. On the other hand, increasing Pe_H for values larger than λ will result in a very slow increase in the overall binding rate while considerably reduces the binding probability for an input analyte.

To numerically analyze the performance of the microfluidic sample delivery and optimize the sensor performance, we have modeled and simulated the analyte convection, diffusion, and surface binding processes in a microfluidic channel using the FEM. We have assumed a pressure-driven incompressible laminar flow, where the input samples with certain analyte concentration is flown through the sample. Our main target

performance measures for the evaluation of a sample delivery system performance are analyte capturing efficiency and the biomolecules binding rate to the sensor surface. Then, the sensor assay time, for any target input analyte concentration sensitivity can be calculated by dividing the minimum number of captured biomolecules that can be detected by the sensor device to the biomolecules binding rate to the sensor surface.

Figure 4.5 (a) and 4.5 (b) show the analyte capturing efficiency and the biomolecules binding rate to the surface of the sensor versus the normalized Péclet constant (Pe_H / λ) in the simulated microfluidic channel. Figure 4.5 (c) shows the schematic of the simulated microfluidic channel. The microfluidic channel used in this simulation has a height and width of 10 μm and 3 μm, respectively. The embedded sensor device in the microfluidic channel is assumed to be a waveguide with the height and width of 220 nm and 500 nm, respectively, which guides the light at the direction normal to the flow direction. Therefore, the coated surface of the sensor has a length and width of 0.5 μm and 10 μm, along and normal to the flow direction, respectively. The microdisk in Figure 4.5 (c) is not considered in the simulation. The surface of the waveguide is assumed to be coated with a surface coating material with $K_{on}=2.5\times10^{5}M^{-1}s^{-1}$, $K_{off}=10^{-3}s^{-1}$, and $C_{S0}=2\times10^{12}$ cm^{-2}. The diffusion constant of the biomolecules in the fluidic environment is also assumed to be $D=100\ \mu m^2/s$. In these simulations, the normalized Péclet constant range of 0.01 to 1000 correspond to an input flow rate range of 0.1 pL/min to 10nL/min for the envisioned microfluidic channel. The concentration of the input analyte for this simulation is assumed to be 1nM. As it is evident from Figure 4.5 (b) the variation of the analyte binding efficiency with the normalized Péclet constant (i.e., input flow rate) is very slow for the normalized Péclet constants smaller than one and larger than 100.

However, for normalized Péclet constant between one and 100, there is a trade-off between the analyte capture efficiency and the rate of analyte binding to the sensor surface. In this case, the selection of the input flow rate depends on different parameters of the specific application, such as the available sample volume, target assay time, and the device sensitivity.

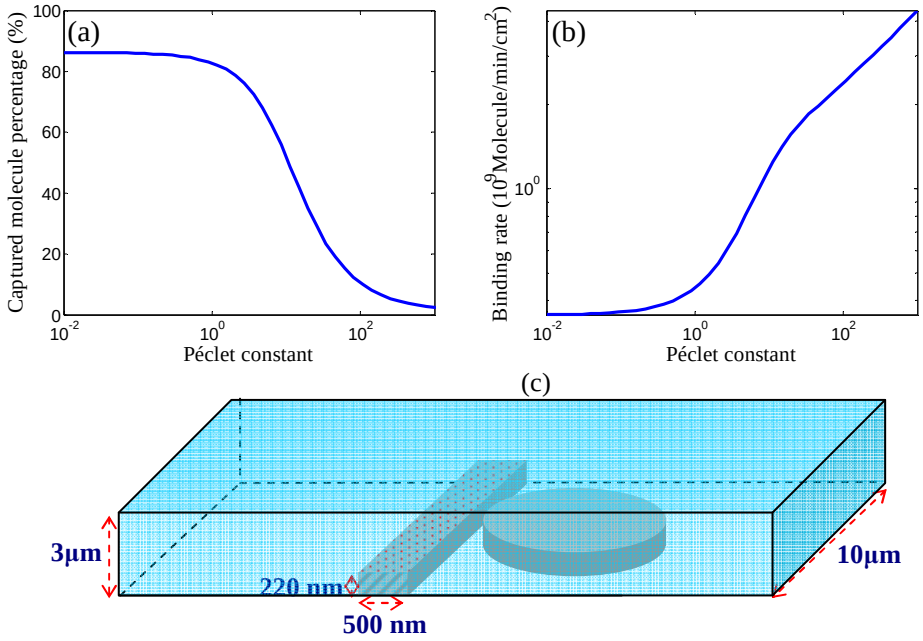

Figure 4.5: The analyte capturing efficiency (a) and the biomolecules binding rate to the sensor surface (b), in a microfluidic channel versus the normalized Péclet constant (Pe_H / λ). Theses results are done for a microfluidic channel with the height and width 10 µm and 3 µm, respectively (Figure (c)). The sensor device is assumed to be a waveguide with the height and width 220 nm and 500 nm, respectively (The microdisk in this Figure is not considered in the simulation). The surface of the waveguide is assumed to be coated with a surface coating material with $K_{on}=2.5\times10^{5}M^{-1}s^{-1}$, $K_{off}=10^{-3}s^{-1}$, and $C_{S0}=2\times10^{12}\ cm^{-2}$. The diffusion constant of the biomolecules in the fluidic environment is also assumed to be $D=100\ \mu m^2/s$. The normalized normalized Péclet constant range of 0.01 to 1000 in this simulation correspond to an input flow rate range of 0.1 pL/min to 10nL/min for the envisioned microfluidic channel. The concentration of the input analyte in this simulation is assumed to be 1nM.

In a pressure driven microfluidic channel, in addition to the analyte capturing efficiency and the biomolecules binding rate to the sensor surface, the required pressure to flow the sample through the microfluidic channel is also an important design

parameters. In the absent of any limit for the input pressure, one may consider narrowing down the microfluidic channel to surface reaction-limited region (i.e., *Da~=1*), while keeping the input flow rate constant. However, the pressure drop per unit length (P_L) in microfluidic channel, for a constant input flow rate (Q), is inversely proportional to the third power of the channel height (assuming h< w):

$$P_L = \frac{12\eta}{h^3 w} Q, \tag{4.6}$$

where η is the viscosity of the fluid in the microfluidic channel. The maximum pressure that can be applied to a typical microfluidic channel is typically limited to a few tens of milibars. Therefore, in he the design of a microfluidic sample delivery system the microfluidic channel geometry should be adjusted so that the required pressure does not exceed this pressure limit for the range of the target input flow rates.

Figure 4.6 shows the simulation of the analyte capturing efficiency, the biomolecules binding rate to the sensor surface, and the pressure drop in a microfluidic channel. The microfluidic channel geometry, biomolecule specimen, and the surface chemistry used in this simulation are the same as those of Figure 4.5. As it is evident from Figure 4.6(c), a pressure drop rate less than 10 mbar/mm can be obtained for input flow rate less than 1nL/min (i.e., $Pe_H / \lambda < 100$)). Figure 4.6(d) shows the distribution of the analyte in the proximity of sensor surface for four different input flow rates, as they are marked on Figure 4.6 (b). As can be inferred from this figure, by increasing the input flow rate, the size of the analyte depleted region on the top of the sensor surface shrinks and the effective analyte concentration on top of the sensor increases. However, the concentration

of the analyte at the microfluidic channel outlet increases that is an indication a lower analyte capturing efficiency.

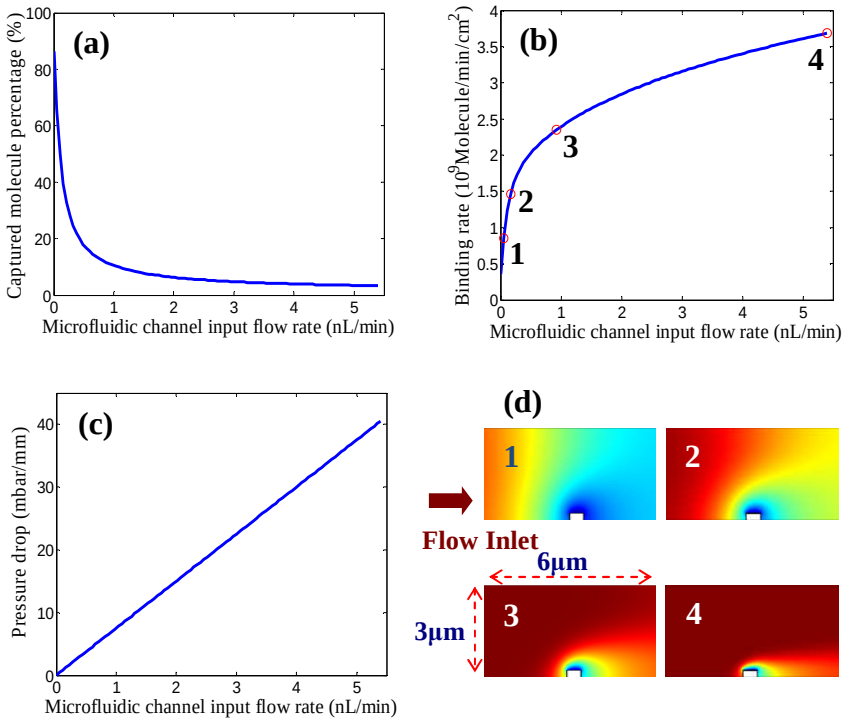

Figure 4.6: The simulation of the analyte capturing efficiency (a), the biomolecules binding rate to the sensor surface (b), and the pressure drop in a microfluidic channel. The microfluidic channel geometry, biomolecule specimen, and the surface chemistry used in this simulation are the same as those of Figure 4.5. Figure (d) shows the distribution of the analyte in the proximity of sensor surface for four different input flow rates, as they are marked on Figure (b).

4.3 Initial experimental investigation of refractive index sensing

To experimentally investigate the resonator-based refractive index sensing, we have developed an experimental setup to continuously measure the changes in the resonance wavelength of sensing resonators. The photonic devices that are used in these experiments are fabricated using ePixfab foundry. The devices are fabricated in a 220 nm thick SOI wafer. Figure 4.7 shows the microscope image and the transmission spectrum of an array of 64 2µm-radius microdonut resonators designed to show the possibility of dense multiplexing of resonator-based refractive index sensors. Each resonator in the

array is designed to have a slightly different resonance wavelength. The microresonators in the array are designed to have a uniform resonance spacing of 0.6 nm over the 54 nm FSR of the resonators; however, because of the fabrication imperfections the actual resonance spacing varies.

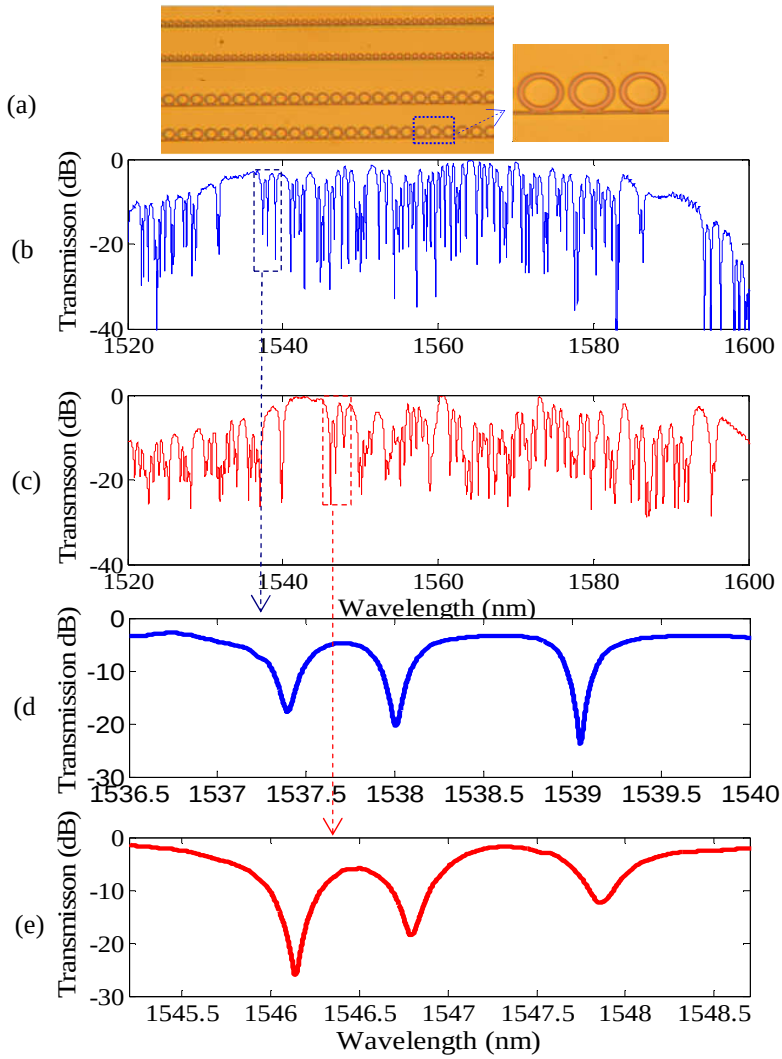

Figure 4.7: Microscope image of a microresonator array composed on compact microresonators coupled to a common interrogating waveguide. (b) and (c) the transmission spectrum of an array of 64 2μm-radius microdonut resonators with air and water claddings. This sample is fabricated using ePixfab foundry service. The microresonators are designed to have a 0.6 nm resonance spacing; however, because of the fabrication imperfections the actual resonance spacing varies. The FSR of the resonators in the array is 54 nm. (d) and (f), the transmission spectra of three of the resonators in the array. The resonance wavelength of the samples with the water cladding is shifted by 9 nm that correspond to a refractive index sensitivity of 27 nm/RIU (the surface of the resonator sample is covered with a 10 nm-oxide layer).

The resonators are initially characterized by measuring their transmission spectra using a tunable laser source. The sample is placed on a thermoelectric cooler (TEC) stage to stabilize the sample temperature variation. The light input and output coupling to the photonic structure is done through a set of two grating using two cleaved single-mode fibers. The resonator devices transmission spectra are measured by scanning the wavelength of the tunable sensor at a speed of 500 pm/sec (the minimum allowable rate with our available laser). The detector output is then collected by an analog to digital convertor (ADC), synchronized with the laser scan through a trigger signal. Using a sampling rate of the 20 ks/s, the measured spectrum resolution is 25 fm. The measured spectrum is then filtered to reduce the effect of the measurement noise on the measurement of the resonance wavelength.

In our experiments in this thesis, we have used a reservoir on top of the sensor device rather than using a microfluidic channel. A thin SU8 layer is spin coated and patterned to define the reservoir window. A Thick PDMS film with similar opening window is then bound on the SU8 layer to achieve the desired total reservoir volume. The whole reservoir is then capped with another PDMS layer to prevent the evaporation of the fluid in the reservoir during the experiment.

4.3.1 Analysis of the resonance wavelength shift measurement stability

As we already discussed, the main factors that affect the sensitivity of refractive index sensing based on scanning laser source are the repeatability of the laser wavelength during scan and thermal variations. To characterize the stability of the measured refractive index sensing based on a single resonator sensing element, we have measured the transmission spectrum of a resonator over time scales comparable to our actual

sensing time. While, in ideal cases, we expect that the transmission spectrum remain the same over the time, in reality the transmission spectrum undergoes variations caused by the variations in the tunable laser wavelength and the resonator resonance wavelength (caused mainly by the thermal fluctuations). These variations put the limit on the minimum detectable resonance wavelength shift without using on-chip reference resonators. Figure 4.8 shows the variation in the measured spectra and variations in the resonance wavelength of a 2μm-radius microdonut resonator with phosphate buffered saline (PBS) cladding measured over a time interval of 90 minutes. These measurements show a drift in the detuning between the laser and the resonator resonance wavelength of 0.044 pm/minutes and random fluctuations with a standard deviation of 0.257 pm.

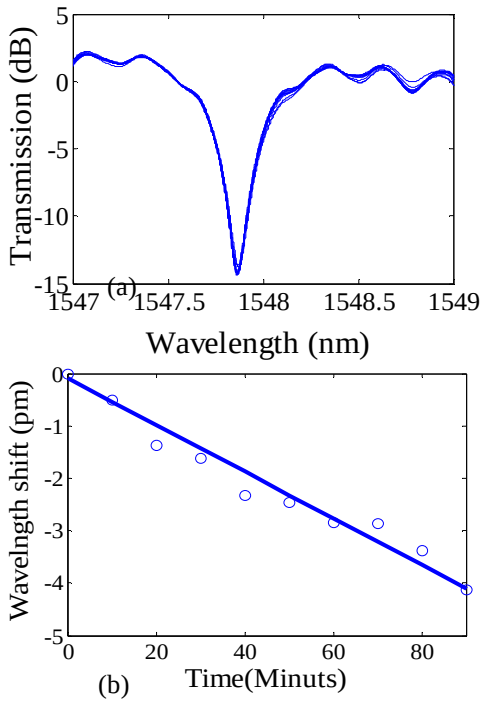

Figure 4.8: The test for the resonance wavelength stability. (a) The transmission of a 2 μm-radius microdisk resonator, coupled to a side waveguide. The transmission spectrum of the resonator is recorded every 5 minutes over about 90 minutes. (b) The variation in the resonance wavelength. The resonance wavelength shift caused by the combined effect of the laser instability and thermal fluctuation shows a drift of 0.044 pm/minutes and random fluctuations with a standard deviation of 0.257 pm.

4.3.2 Measurement of the bulk sensitivity of the resonator-based refractive sensors

To benchmark the sensitivity of the refractive index sensitivity of the resonator-based sensors, we first measure their bulk refractive index sensitivity using a series of different cladding materials with different refractive index. The bulk refractive index sensitivity is measured in terms of nm/RIU by dividing the shift in the resonance wavelength of the resonator to the change in the refractive index of the cladding material. To control the refractive index of the resonator cladding material, we have used different glucose solutions with different concentrations. The refractive index of the glucose solution can be related to its concentration by $n_g(C)=0.2015C+1.3292$ [94], where $n_g(C)$ is the solution refractive index at the concentration in term of weight percentage. Figure 4.9 shows the transmission spectra of a microring resonator with a radius of 4 μm for different glucose concentration in the cladding water (the width and thickness of the microring are 400 nm and 220 nm, respectively). Different curves correspond to different concentrations from 0% to 5%.

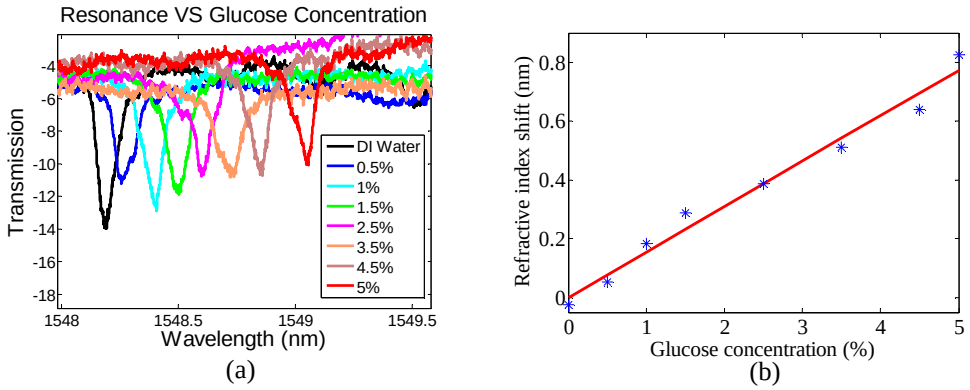

(a) (b)

Figure 4.9: (a) Transmission spectra of a microring resonator with a radius of 4μm and width andfor different glucose concentration in the cladding water (the width and thickness of the microring are 400 nm and 220 nm, respectively). Different curves correspond to different concentrations from 0% to 5%. (b) the shift in the refractive index with the glucose concentration showing a resonance shift of 0.155 nm / %. Using the model for the glucose solution refractive index, this corresponds to a refractive index sensitivity of 77 nm/RIU for the microring resonator.

The shift in the refractive index with the glucose concentrations shows a resonance shift of 0.155 nm / %. Using the model for the glucose solution refractive index, this corresponds to a refractive index sensitivity of 77 nm / RIU for the microring resonator, which is close to 81 nm/RIU refractive index sensitivity, calculated using FEM simulation.

4.3.3 Proof of concept demonstration of label-free biosensing

The proof of concept demonstration of the microresonator-based sensors is done by using streptavidin-biotin binding. Streptavidin has a very high affinity for biotin ($K_{on}=6.5\times10^{7}$ $M^{-1}s^{-1}$ and K_d = 1fM) that is the strongest know binding between a protein and a ligand. In our experiment, we first immobilize biotin on the sensor surface. The streptavidin solution in PBS is then introduced to the coated sample through the fluidic reservoir on top of the sensor surface. The biotin and streptavidin molecular weights are 244 Da and 68kDa, respectively. In this respect, streptavidin is a much larger molecule that can be modeled with nanosphere with a diameter of 6.2 nm. The diffusion constant of the streptavidin in the buffer solution is 430 $\mu m^2/s$.

Figure 4.10 shows the changes in the resonance wavelength of the resonator versus time, caused by the binding of the streptavidin molecules to the resonator surface. A maximum shift of 80 pm is observed for the addition of 20 uL of a streptavidin solution with a concentration of 10μg/mL in a reservoir, already filled with 20 uL of PBS. Because of the high concentration of the streptavidin solution in this experiment, we expect that all the binding sites on the sensor surface are filled with streptavidin molecules. The measured shift of 80 pm corresponds to a streptavidin molecules density of 1.19×10^{12} cm^{-2}. This is in contract to a binding density of 2.6×10^{12} cm^{-2} and a resonance shift of *175* pm that

correspond to the case when streptavidin molecules saturate the surface by forming a closely packed coating on the sensor surface. The surface binding time constant for this experiment can be estimated to be around 5 minutes that is mainly limited by the rate of the streptavidin molecule diffusion to the sensor surface.

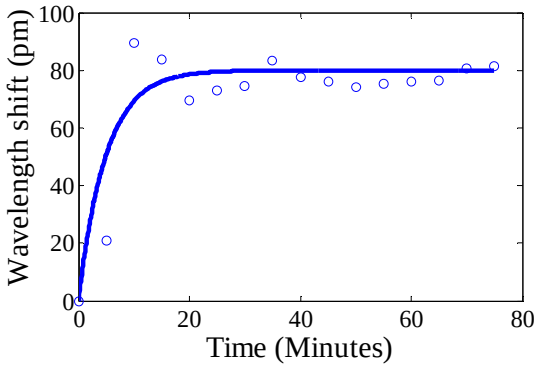

Figure 4.10: The shift in the resonance wavelength of the microdisk resonator, caused by the streptavidin binding to the sensor surface versus time. The concentration of the input streptavidin solution is ~5μg/mL.

CHAPTER 5

Simultaneous Trapping and Sensing of Dielectric Nanoparticles in Microdisk Optical Trap

Optical tweezers [95, 96, 97, 98] are very efficient tools for trapping and manipulating particles and have become a common tool in medicine and biology. Current commercial optical tweezers based on the gradient force on a single focused beam in free space tend to be bulky and expensive. It is highly desirable to miniaturize optical traps on a planar platform, which is compatible and integratable with low-cost microfluidic chips. On the other hand, conventional optical tweezers can trap particles with sizes in the range of several micrometres to a few hundred nanometres. However, manipulation of nanoparticles with much smaller sizes, as required in sensing applications, demands much higher field intensities and larger field gradients, which can only be obtained using near-field optics [99, 100]. Recently, several different near-field methods have been developed [101, 102, 103, 104], where the evanescent extension of the field in the surrounding fluidic environment is used to manipulate (i.e., trap or guide) nanoparticles. Optical particle transport in waveguide-based optical structures [103, 105] and nanoparticle trapping in the localized field of the plasmonic nanostructures [106, 107] are examples of these works. However, the required power levels in these works are too high to enable real lab-on-a-chip application. The large enhancement of the near-field intensity in high-Q and small-mode-volume dielectric resonators can considerably relax the input power level requirement for stable nanoparticle trapping. In the past few years, the

possibility of trapping atoms and nanoparticles in high-Q dielectric resonators has been studied by several groups. In [108] a PC resonator-based optical trap is theoretically investigated. A theoretical analysis of the possibility of simultaneous atom trapping and detection in microdisk resonators is also presented in [109]. Very recently, Arnold et al. have demonstrated the possibility of simultaneous optical trapping and sensing of nanoparticles using whispering gallery modes in stand-alone silica microspheres [110]. In this work, polystyrene nanoparticles with a diameter less than 300 nm are trapped in the resonator optical trap.

In this chapter, the possibility of trapping small nanoparticles in compact microdisk resonators optical traps is studied. Furthermore, I have developed a model for the analysis of the effect of the optical trapping on the analyte concentration and the nanoparticle trapping lifetime in the vicinity of a resonator.

5.1 Optical forces in the near-field of a micro-resonator

In general, the exerted optical force on a nanoparticle in an electromagnetic field can be split into two parts, namely, the gradient force (f_{grad}) and the propulsive force (f_p) [111, 112, 113]. The gradient force corresponds to the change in the total stored electromagnetic energy in the field caused by a nanoparticle movement. Therefore, the gradient force attracts the nanoparticle to the high intensity parts of the field and depends on the gradient of the electric field intensity:

$$f_{grad} = \frac{1}{4}\nabla_r \left|E(r)\right|^2 \Re(\alpha), \tag{5.1}$$

where α is the nanoparticle polarizability by the electromagnetic field. The propulsive force corresponds to the transfer of the momentum from a photon to the nanoparticle caused by the photon absorption or scattering;

$$f_p = \frac{n_{eff}}{c} S\sigma_{ex}, \tag{5.2}$$

where n_{eff} is the effective refractive index, S is the electromagnetic field Poynting vector, and σ_{ex} is the nanoparticle extinction cross-section (i.e., summation of absorption (σ_a) and scattering (σ_s) cross-sections, $\sigma_{ex} = \sigma_s + \sigma_a$). In the case of a nanoparticle interaction with a resonator, the change in the total stored energy in the resonator (ΔU_c) can be manifested by the change in the resonance frequency ($\Delta\omega$) of the resonator $\Delta U_c = U_c(\Delta\omega/\omega)$, where U_c is the total stored energy in the microresonator, and ω is the resonance frequency of the unperturbed resonator. Therefore, the gradient optical force, alternatively, can be written in terms of the perturbed resonator resonance frequency gradient with respect to the nanoparticle position (i.e., $\nabla_r\omega$) [114]:

$$f_{grad} = -\frac{U_c}{\omega}\nabla_r\omega\,. \tag{5.3}$$

5.2 Simultaneous trapping and sensing of the dielectric nanoparticles on high-Q silicon micro-resonators

The small mode volume and high-Q of compact Si micro-resonators result in a considerable enhancement of the light-matter interactions in their near-field. This enhanced interaction of the microdisk resonators with their surrounding material provides a very sensitive and powerful device for the label-free sensing applications based on the optical interrogation of nanoparticles. However, because of the small effective sensing area of microdisk resonators and low affinity and slow binding kinetics of the chemical binding surface coatings, the effectiveness of these devices is limited by the slow transport rate of the nanoparticles to the surface of the microdisks [21]. One possible

solution for this issue is to use the intense field in the near-field of the microdisk resonators to attract nanoparticles toward the microdisk resonator. The nanoparticles then can be trapped on the microdisk resonator surface at the positions where the maximum sensitivity can be obtained. This, not only can improve the rate of the nanoparticle binding to the surface of the microdisk resonator, but also enables a selective reversible binding process, where optical trapping can be used to capture and analyze a particle and then release it. By turning the input laser source off for a short time (or by a small detuning of the laser from the microdisk resonance), the trapped nanoparticle can be released from the microdisk resonator surface and the same microdisk can be used to interrogate another nanoparticle.

The slow binding kinetics of the molecular interaction on the sensor surface results in a long binding time. As a results, a molecule on the sensor surface may be pulled away from the sensor surface by the Brownian motion (i.e., diffusion process) before it gets the chance to bind to the immobilized molecules on the surface. In fact, a molecule may hit the sensor surface many times before it is captured on the surface by the surface coating. As an example, assume a particle with a diameter of 80 nm (it can be a single virus or a DNA, diffusion constant $(D) = 5\ \mu m^2/s$) is in a 100 nm-proximity of the surface of a sensor that is coated with a typical antibody surface coating ($K_{on}=5\times10^4 M^{-1}s^{-1}$, $K_{off}=10^{-3}s^{-1}$, $C_{S0}=10^{12}\ cm^{-2}$). In this case, the time constant for the surface reaction is 0.12s; however, the average time that the nanoparticle spends in the 100 nm-proximity of the sensor surface before it is pulled away by the Brownian motion is only 4 ms. This means that the nanoparticle may get in and out of the 100 nm-proximity of the sensor surface 30 times before it is actually captured.

The optical trapping can assist the binding process by increasing the time that the particle spends in the proximity of the sensor surface. By using a resonator-based optical trap, when a particle approaches the surface of the sensor (i.e., sensor) it will be trapped there for a long time. Therefore, it can get enough time to interact with the immobilized molecule on the surface and bind to the sensor surface before escaping from the trap.

5.3 Optical force and microdisk resonator optical trap stability

When a nanoparticle approaches the surface a high-Q and small-mode-volume microdisk resonator, the localized and intense near-field of the microdisk confines the nanoparticle in the radial and vertical directions. However, because of the traveling nature of the resonant modes in the microdisk resonators, a repulsive force along the traveling direction of the light in the resonator is also exerted on the nanoparticle. Therefore, while the nanoparticle will be trapped at the position with the highest electrical field in the radial-vertical plane, it will be forced to move along the microdisk resonator perimeter by the propulsive force. Figure 5.1 shows a schematic of the different forces exerted on a nanoparticle in a microdisk optical trap.

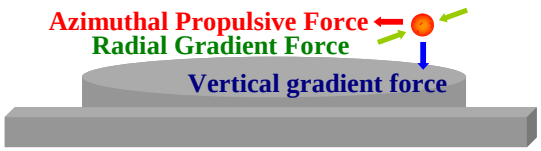

Figure 5.1: A nanoparticle in a Si microdisk resonator optical trap. Different optical forces, exerted on a nanoparticle in a microdisk resonator optical trap, are shown.

In a microfluidic environment, in addition to the optical forces, a nanoparticle also undergoes Brownian forces that may force the nanoparticle out of the microdisk resonator optical trap. The optical trap stability depends on the random thermal energy of the

nanoparticle due to Brownian motion and the energy required to move the nanoparticle out of the trap (W_{trap}):

$$W_{trap} = -\Delta U_c = -U_c \Delta\omega_p / \omega\,, \tag{5.4}$$

where $\Delta\omega_p$ is the total shift in the resonator resonance frequency caused by the nanoparticle. The optical trap stability is usually quantified by the trap stability number (S_t) [115]:

$$S_t = W_{trap} / K_B T\,, \tag{5.5}$$

where K_B is the Boltzmann constant, and T is the system temperature. As can be seen from the above equations, the trap stability scales with $\Delta\omega_p$, the stored power in the resonator depends on the input waveguide power (P_{in}), the resonator quality factor (Q_c), and amount of input laser detuning from the resonance wavelength ($\Delta\omega$). For a microdisk resonator critically coupled to the input waveguide we have:

$$U_c(\Delta\,\omega) = \frac{U_c(0)}{1+(\Delta\omega/\Delta\omega_c)^2} = \frac{2P_{in}Q_c}{\omega}\frac{1}{1+(\Delta\omega/\Delta\omega_c)^2}\,, \tag{5.6}$$

where $\Delta\omega_c = 0.5\omega/Q_c$ is the resonator half linewidth and $\Delta\omega = \Delta\omega_0 + \Delta\omega_p$ ($\Delta\omega_0$ is the initial frequency detuning of the unperturbed resonator). The trap stability factor (S_t) then can be found as

$$S_t = -\frac{P_{in}}{\omega K_B T}\,\frac{\Delta\omega_p/\Delta\omega_c}{1+\left(\dfrac{\Delta\omega_0+\Delta\omega_p}{\Delta\omega_c}\right)^2}\,. \tag{5.7}$$

For a fixed input laser initially tuned to the resonator resonance frequency ($\Delta\omega_0$), the maximum trap stability depends only on the input power and the resonance frequency. Therefore, although for small nanoparticles the microdisk resonator trap stability

increases with the nanoparticle polarizability (α) (i.e., size and/or refractive contrast to the environment), there is an optimum trap stability factor that corresponds to a certain magnitude of the nanoparticle polarizability. However, for a fixed nanoparticle, the trap stability is proportional to the quality factor to mode volume ratio:

$$S_t \propto \Delta\omega_p / \Delta\omega_c \propto Q_c / V_c . \tag{5.8}$$

The small mode volume and high Q of compact microdisk resonators enable us to stably trap nanoparticles with much smaller sizes compared to those trappable in conventional optical traps. To provide numerical evidence for the strength of the microdisk resonators optical trap, we have numerically simulated the trap stability and optical forces for a 4 μm diameter microdisk resonator fabricated on an SOI wafer with a top silicon layer thickness of 220 nm. The coupling of the microdisk resonator with the input waveguide is adjusted to obtain a critical coupling. The resonant modes of the microdisk resonator are calculated by solving auxiliary symmetric Maxwell equations using the FE method. Figure 5.2 shows the mode profile, the trap stability factor, and the gradient optical forces in the vertical and radial directions exerted on a 50 nm diameter gold nanosphere. The microdisk resonator mode in this example is the first-order radial TE mode at the λ=1.547μm (λ is the resonance wavelength of the microdisk resonator). The coupled power to the input waveguide is assumed to be 1mW. The overall Q of the microdisk resonator in assumed to be 50,000 [24]. Figure 5.2 (a) shows the microdisk resonator mode profile of the radial component of the electric field (Er). Figure 5.2(b) shows the trap stability factor at different nanoparticle positions. As can be seen from this figure, trap stability factors as high as 40 and 60 can be obtained. Figure 5.2 (c) and

Figure 5.2(e) show the profile of the vertical and radial force components exerted on the gold nanospheres in the vertical-radial plane.

The cross-sections of the gradient forces on the microdisk resonator surface are shown in Figure 5.2 (d) and Figure 5.2 (f). As can be seen from these figures, there are four different stable traps on the surface of the microdisk resonator. The two main stable traps on the top surface and the edge of the microdisk are marked as T1 and T3 in Figure 5.2 (d) and Figure 5.2 (f), respectively. The other two traps (marked as T2 and T4) have a very small trapping range.

One important feature of an optical trap, especially for sensing applications, is the trapping strength, which can be quantified by the root mean square displacement (RMSD) of the particle position from the optical trap center caused by the Brownian forces. The RMSD in an optical trap (i.e., $\sqrt{\langle \xi(t)^2 \rangle}$, where ζ is the particle displacement in the radial-vertical plane, along the resonator surface) depends on the trap spring constant (i.e., $k_t = \partial f_{grad} / \partial \xi$) [116, 117]:

$$\sqrt{\langle \xi(t)^2 \rangle} = \sqrt{\frac{k_B T}{k_t}} . \tag{5.9}$$

The trap spring constant for the T1 and T3 traps (refer to Figure 5.2) are 22 pN/um and 7 pN/um, respectively. This results in an RMSD of 14 nm for the T1 trap and an RMSD of 24 nm for the T3 trap. The vertical and lateral forces for the T1 and T3 traps are 0.9 pN and 0.6 pN, respectively.

The scattering cross-sections of the nanoparticles scale with the square of their volume [61]. Therefore, usually the propulsive force is much less than the gradient force. However, when a nanoparticle approaches the surface of a microdisk resonator, it couples

the degenerated modes inside the microdisk resonator. The nanoparticle-induced reflection of the CW mode of the microdisk resonator into its CCW counterparts transfers a large momentum to the nanoparticle. The propulsive forces caused by the nanoparticle scattering and mode coupling are depicted in Figure 5.3(a) and Figure 5.3(b), respectively.

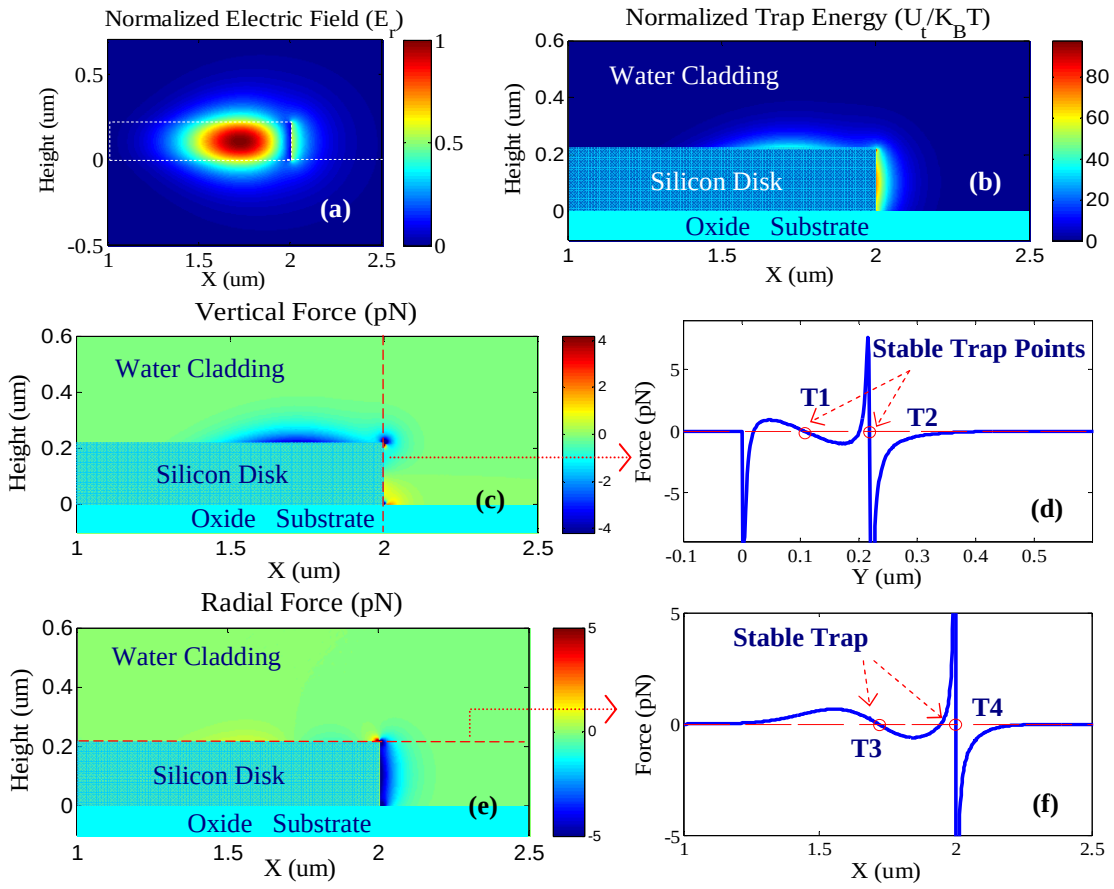

Figure 5.2: A nanoparticle in a Si microdisk resonator optical trap. (a): The electric field (Er) distribution for a resonant TE mode of the 4μm diameter Si microdisk resonator. (b): The optical trap stability factor (Ut/KBT) as a function of the position for a 50 nm diameter gold nanoparticle. (c) and (e): The vertical and radial force component exerted on the 50nm diameter gold nanosphere versus the nanoparticle position. (d) and (f): The gradient force cross-sections along the lines, marked in figures (c) and (e). The locations of different stable trap points are marked in the figures (d) and (f). The resonant mode of the microdisk resonator is a first order radial TE mode (TE18,1) resonating at λ=1.547μm. The quality factor of the microdisk resonant mode is assumed to be 50,000. The coupled power to the input waveguide is assumed to be 1mW.

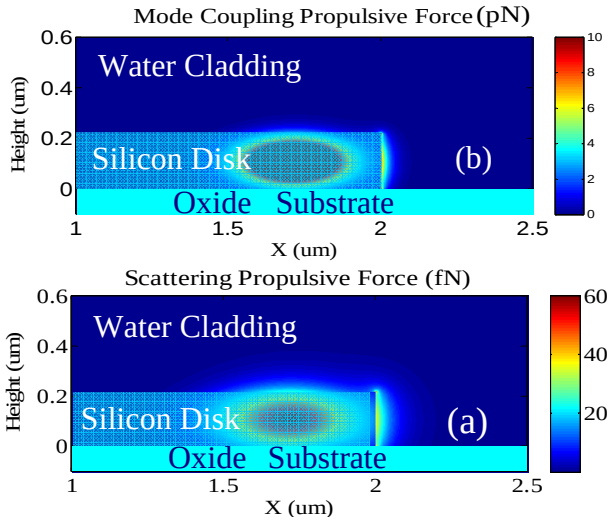

Figure 5.3: The map of the repulsive forces, in the azimuthal direction, exerted on a nanoparticle in a microdisk resonator optical trap. (a): The map of the repulsive force caused by the light scattered through the nanoparticle. (b): The map of the repulsive force caused by coupling to the reflection mode (i.e., CCW mode) through the nanoparticle. All of the device parameters are similar to those of Figure 5.2.

As can be seen from Figure 5.3, at the regions close to the microdisk resonator, the propulsive force caused by the nanoparticle-induced mode coupling is a few orders of magnitude larger than the scattering repulsive force. This repulsive force (f_p) speeds up the nanoparticle along the microdisk resonator azimuthal with a relatively high speed. The nanoparticle azimuthal speed (v_p) can be calculated as $v_p = f_p /(6\pi\eta r_p)$, where η is the fluid viscosity and r_p is the nanoparticle radius. Assuming a viscosity similar to that of water for the fluid environment (i.e., $\eta = 1\times10^{-3}\ Ns/m^2$), this repulsive force causes the nanoparticle to spin around the microdisk resonator with a frequency as high as 300 Hz. However, it should be noted that in this analysis we considered a microdisk resonator that does not have any inherent mode splitting. In practice, because of the surface roughness, most of the high-Q modes of small microdisks are split [118]. Mode splitting mixes the CW and CCW modes. This considerably reduces the overall azimuthal

repulsive force. Furthermore, the resulting standing wave generates a gradient force in the azimuthal direction, which leads to a three-dimensional trap for the nanoparticle.

The resonance frequency shift caused by the trapped nanoparticle manifests itself in changes in the transmission amplitude and phase of the coupled waveguide-microdisk resonator structure. These variations not only can be used to detect a trapping event, but also provide some information about the nanoparticle properties such as size and refractive index. Our study in this section shows that small nanoparticles, with diameters as low as 20 nm, can be stably trapped on a microdisk resonator at relatively low input power (e.g., 1mW). However, the mass sensing detection limit can potentially be even smaller than this. As an example, for a microdisk resonator with a resonance wavelength at 1.55 μm, a stability factor of 8 corresponds to a normalized resonance shift ($\Delta\omega_p / \Delta\omega_c$) of about 0.01 (refer to Equation 5.7) corresponding to a resonance wavelength of 0 .31 pm (for the microdisk resonator with the 50,000 Q). This resonant shift results in a change in the output power about 0.01 of the input power (i.e., 10 μW for 1mW input power).

5.4 Analyte mass transport in the presence of optical trapping

As it was already mentioned, in addition to the external forces (such as optical force), a nanoparticle in a fluidic enviroment undergoes Brownian forces, a random force that is caused by the interactions between the nanoparticle and the fluid molecules. The equation that govern the nanoparticle movement in the fluid can be written as

$$m\frac{\partial^2 \bar{r}}{\partial t^2} = -\gamma\frac{\partial \bar{r}}{\partial t} + f_e(\bar{r}) + \xi\,, \tag{5.10}$$

where m is the nanoparticle mass, $\gamma=6\pi\eta a=k_BT/D$ is the viscous damping force, $f_e(\bar{r})$ is the external force (e.g., optical force) at the position $\bar{r}$, and finally ξ is the white noise Brownian force ($<\xi^2>=2\ \gamma k_BT$). For small nanoparticles, the inertial forces are largely overwhelmed by the viscous forces. Therefore, the particle can be accurately described by the following equation:

$$\frac{\partial \bar{r}}{\partial t} = (f_e(\bar{r}) + \xi)/\gamma . \tag{5.11}$$

As a result, the particle exercises a Brownian motion and a drift motion with a velocity proportional to the applied external force. Therefore, in a solution the total particle flux (J) can be written as

$$J = \frac{D}{k_BT} f_e(\bar{r})C - D\nabla C , \tag{5.12}$$

where C is the nanoparticle density in the fluid. In the above equation, the first term on the right is the flux caused by the external force and the second term is the diffusion flux (i.e., the flux due to the Brownian motion of nanoparticles). The density of the nanoparticle in the fluid then can be shown by the Nehrnst-Planck [117] equation as follows:

$$\frac{\partial C}{\partial t} = -\nabla . J = -\nabla . \left(\frac{D}{k_BT} f_e(\bar{r})C - D\nabla C \right). \tag{5.13}$$

The main optical force that is exerted on a nanoparticle in an optical trap is the gradient force that can be written as $f_e(\bar{r}) = \beta \nabla I$, where ($\beta = \Re(\alpha)/4$), and $I = \left|\bar{E}(r)\right|^2$. The equation (5.13) then can be written as

$$\frac{\partial C}{\partial t} = -\nabla . \left(\frac{D}{k_BT} (\beta \nabla I)C - D\nabla C \right). \tag{5.14}$$

This equation can be simplified by defining W as

$$W = \exp\left(\frac{\beta}{k_B T} I\right). \tag{5.15}$$

By replacing I with W in the equation (5.14) we have:

$$\frac{\partial C}{\partial t} = -\nabla . - D\left(-\frac{\nabla W}{W} C + \nabla C\right). \tag{5.16}$$

Now, by defining the weighted nanoparticle density (M) as $M = C/W$, the solution for the weighted nanoparticle density can be found by solving a simple diffusion equation as

$$W\frac{\partial M}{\partial t} = -\nabla . - DW\nabla M\,, \tag{5.17}$$

and the nanoparticle flux (J) can be found as $J = -DW\nabla M$. In the steady state condition in a fluid reservoir (i.e., $J=0$), we will have :

$$\nabla M = 0 \Rightarrow C = C_0 W\,, \tag{5.18}$$

where C_0 is nanoparticle concentration far from the optical trap where, $I = 0$ (i.e., $W = 1$). This means the nanoparticle concentration in an optical trap is increases by a large factor, which exponentially increases by the trap stability factor ($S_t = \beta I / k_B T$). For example, a trap stability factor of only 5 leads to an effective increase of 148 in the effective concentration of the nanoparticles on the resonator surface.

One important aspect on an optical trap is the nanoparticle lifetime in the trap. The nanoparticle lifetime is the average time that a trapped nanoparticle spends in the trap before escaping from it. To calculate nanoparticles lifetime in the optical trap, we assume nanoparticles are injected in the trap by a constant rate. A boundary is defined for the optical trap. If a nanoparticle crosses this boundary, it has escaped the optical trap. Then, the nanoparticle lifetime can be calculated by dividing the total number of the

nanoparticles in the trap to the rate of nanoparticles escaping from the trap. The density of the nanoparticle in the trap generated by the injected nanoparticle can be calculated by solving the diffusion equation (equation 5.17) for steady state condition.

$$W\frac{\partial M}{\partial t} = -\nabla . - DW\nabla M = 0 . \tag{5.19}$$

Assuming nanoparticles can not return to the trap once passing through the trap boundary, the nanoparticle concentration on the trap boundary should be forced to zero. At this condition, the rate of nanoparticle escaping from the trap (I_s) is equal to the rate of the inject nanoparticles in the trap. The number of total nanoparticles (N_{np}) in the trap also can be estimate by integrating over the nanoparticle concentration ($C=MW$) over the trap volume ($N_{np}= \int_{V_{trap}} MWdV$). Then, the nanoparticle lifetime in the trap (τ) can be calculated as

$$\tau = \frac{N_{np}}{I_s} = \frac{\int_{V_{trap}} MWdV}{\int_{S_{trap}} JdS}, \tag{5.20}$$

where $J = -DW\nabla M$ is the nanoparticle flux in the trap and the integrations in the numerator and denominator (of the fraction in the right side of the above equation) are calculated on the total trap volume (V_{trap}) and the trap boundary surface (S_{trap}), respectively.

For the simplified case of an evanescent field trap with a field energy density decay rate of d, the trapping lifetime in the proximity of the trap with a maximum distance of b for (S_t>>1) can be approximated by (refer to Appendix A),

$$\tau = \frac{b^2}{D}\left(\frac{1}{2} + \frac{d}{b}\left(\frac{e^{S_t} - S_t - 1}{S_t}\right)\right). \tag{5.21}$$

Figure 5.4 depicts the optical trapping lifetime versus the trap stability factor for an 80 nm diameter nanoparticle in an evanescent field optical trap. In this figure, the evanescent field energy density decay rate (d) and the trap size (b) are assumed to be 50 nm and 150 nm, respectively (i.e., $b = 3d$). As it is evident from this figure, for a maximum trap stability factor of eight, the nanoparticle can be trapped for half a second. If we double the stability factor ($S_t=16$), the nanoparticle trapping lifetime will exceed 12 minutes.

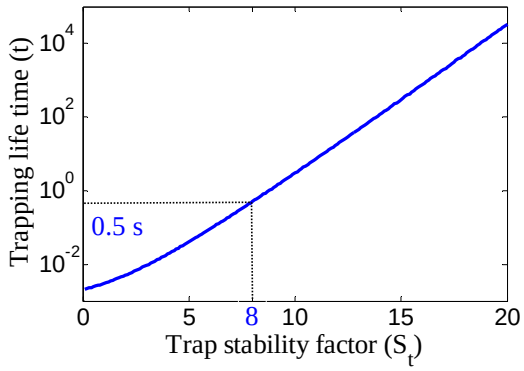

Figure 5.4: The trapping lifetime of an 80 nm-diameter nanoparticle in an evanescent wave optical trap with the energy density decay rate of 50 nm.

To simulate the effect of the optical trapping on the nanoparticle concentration in a microdisk optical trap, we have used FEM to concurrently solve for the resonant mode of the microdisk resonator and the analyte concentration in the resonator optical trap. The optical trap potential is calculated from the field energy distribution of the microdisk resonant mode and the analyte concentration is calculated by solving for the developed model in Equation 5.17 using axial symmetry in cylindrical coordinate. Figure 5.5 shows the effect of the optical trapping on the local concentration of analytes at the vicinity of the microdisk resonator surface. Figure 5.5 (a) shows the distribution of the field energy of the resonant mode of the microdisk resonator. Figure 5.5 (b) shows the distribution of the gold nanoparticle concentration (50-nm gold nanoparticle) in the proximity of a microdisk resonator. The microdisk resonator in this simulation has a diameter and

thickness of 2 μm and 230 nm, respectively. The loaded Q of the microdisk resonator is assumed to be 15,000. In this simulation, the initial concentration of the analytes outside the optical trap (imposed by the analyte concentration on the reservoir boundary) is one. Figure 5.5(c) shows the change in the concentration of the nanoparticle concentration in the optical traps as a function of the resonator input power. As is evident from Figure 5.5 (c), the nanoparticle concentration, at the steady-state condition, can be increased by several orders of magnitudes using moderate resonator input powers.

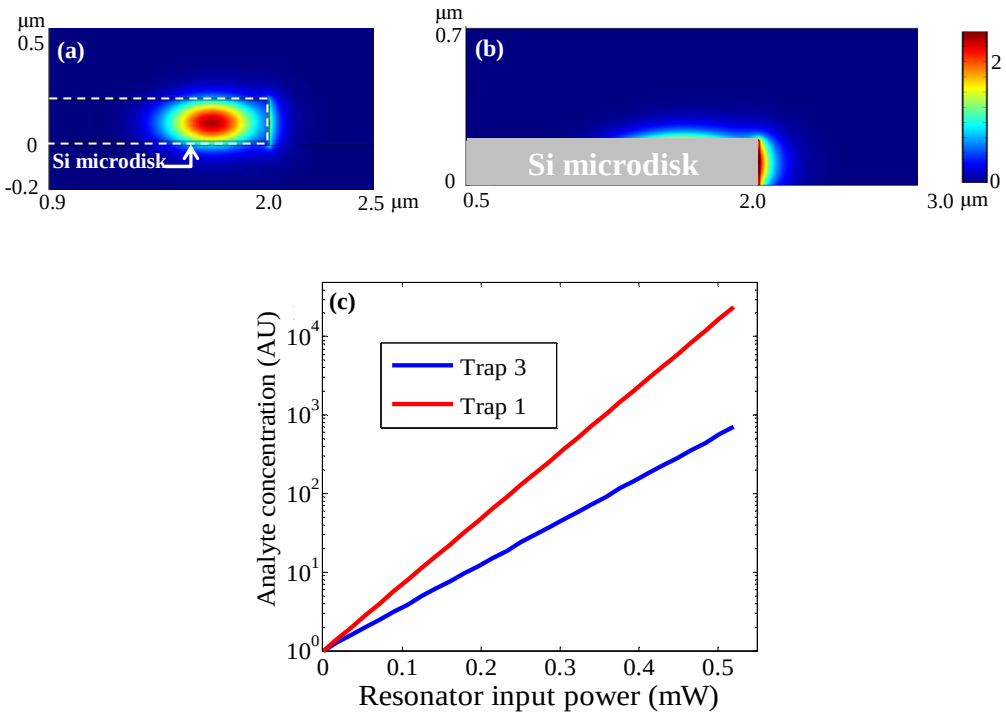

Figure 5.5: Simulation of the nanoparticle (50 nm diameter gold nanoshpere) concentration in a microdisk resonator optical trap. (a), the distribution of the field energy in the microdisk resonator, substrate, and water cladding. (b), the steady state nanoparticle concentration distribution (in logarithmic scale) for an initial analyte concentration (C_0) of one (C_0 = 1). The microdisk resonator input power is assumed to be only 200μW. (c), the nanoparticle concentration in the center of the two microdisk resonator optical traps (i.e., traps T1 and T3 in Figure 5.2) versus the microdisk resonator input power. The microdisk resonator in this simulation has a diameter and thickness of 2 μm and 230 nm, respectively. The loaded Q of the microdisk resonator is assumed to be 15,000.

To calculate the trapping lifetime in our FEM simulation, we inject nanoparticles at the trap position with a certain rate and monitor the analyte concentration for different

microdisk resonator input power. Figure 5.6 shows the distribution of the nanoparticle concentration in the microfluidic reservoir, caused by a nanoparticle source at the center of the optical trap, on top of the microdisk resonator (corresponding to the trap T3 in Figure 5.2), for different microdisk resonator input powers. Figure 5.6 (a) shows the nanoparticle distribution when the optical trap is off and the nanoparticle distribution is only governed by the nanoparticle diffusion in the fluid environment. When the microdisk optical trap is turned on, the optical force attracts the nanoparticle toward the microdisk resonator surface. Therefore, nanoparticles spend a longer time in the vicinity of the microdisk resonator and the effective concentration of the nanoparticles at the resonator optical trap is increased. By increasing the optical trap strength (i.e., increasing the microdisk resonator input power (P_{in})), the nanoparticle trapping lifetime increases; therefore, the concentration of nanoparticle at the trap region increases as well. In our simulated microdisk resonator optical trap, Trap T1 has a higher strength; however, the source is placed in Trap T3. As is evident from the Figure 5.7 at lower trapping strengths (i.e., lower resonator input powers), which the concentration is mainly determined by the nanoparticle diffusion, we have a higher concentration at the Trap T3. However, at higher trapping strengths, nanoparticles diffuse faster between the two traps; therefore, the distribution of the analyte concentration is mainly determined by the trapping potential. At this situation the analyte concentration at the Trap T1 will exceed that of Trap T3.

Figure 5.7 shows the calculated trapping lifetime for thte Traps T1 (Figure 5.2). The trapping lifetime time enhancement is calculated as the ratio of the time that nanoparticles stays in the vicinity of the microdisk resonator to the time that it takes to

scape from the trapping region by Brownian motion. As is evident from this Figure 5.7, trapping lifetimes up to 25 seconds can be obtained with input powers less than 0.5 mW.

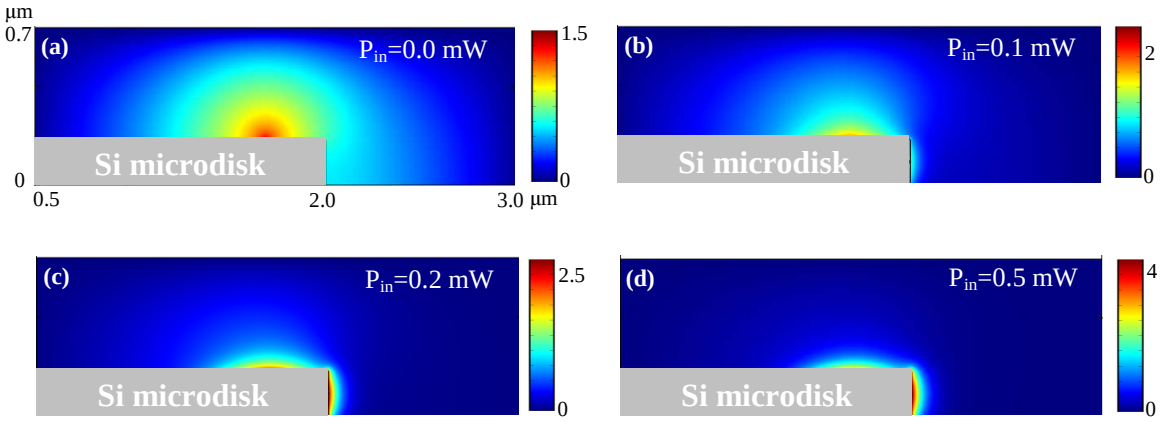

Figure 5. 6: The analyte concentration (in logarithmic scale) in an optical trap generated by a source on the top of the microdisk resonator for different microdisk resonator input power. The analyte concentration on the reservoir boundaries (C_0) are set to one (C_0=1). The microdisk resonator input power for Figures (a), (b), (c), and (d) are 0.0 mW, 0.1 mW, 0.2 mW, and 0.5 mW, respectively. The microdisk resonator and nanoparticle used in these simulations are similar to those of Figure 5.5.

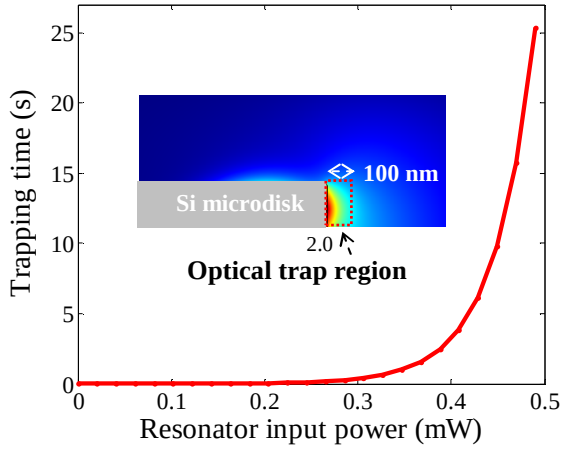

Figure 5.7: the simulated trapping lifetime for a 50 nm-diameter gold nanoparticle in the Trap T1 of the microdisk resonator versus the microdisk resonator input power. The microdisk resonator trap is assumed to extend 100 nm from the sensor surface. The simulation conditions are similar to those of Figure 5.6. The inset figure shows the defined optical trap geometry.

CHAPTER 6

Theoretical Modeling of the Interactions between Resonant Nanoparticles and Microresonators

While biosensors based on fluorescent labeling and label-free refractive index sensing do not provide any specific information about the captured analyte by themselves, Raman spectroscopy provides unique information about the molecular structure of the sensing analyte. Typical Raman cross-sections of the molecules are too low to allow for high-sensitivity sensing; however, the development of SERS techniques [119, 120, and 121] has made it possible to achieve sensitivity levels down to single molecule detection [122, 123, and 18].

The combination of SERS enhancement with the local field enhancement in the near-field of integrated waveguide and resonators can lead to a considerable improvement in the SERS sensitivity. In recent years, several efforts have focused on integrating SERS sensing with on-chop microfluidic-based platforms. Two examples are [124] and [125], which proposed to combine the SERS enhancement with the field enhancement in the core of a micro-structured fiber and a hollow waveguide. Recently, White et al. have reported resonator-enhanced SERS using a liquid core optical ring resonator (LCORR) [126]. The LCORR is a micro-sized glass capillary with a thin wall [127]. The gold nanoparticles flow through the capillary channel and the optical signal is coupled to the whispering gallery mode, which is resonating around the channel. The local field

enhancement in the near-field of the microring resonator in this experiment has led to an enhancement factor of 15 in the emitted SERS signal.

The combination of SPR field enhancement in the metallic nanoparticles with the field enhancement in the integrated high-Q and low-mode-volume microdisk resonator can considerably increase the effective Raman scattering cross-section of the target molecules. The improved Raman scattering cross-section will relax the requirements on high pump laser power and long integration time for SERS based sensing.

The integration of metallic nanoparticles with a microdisk resonator can be done in two different ways. One possible solution is to fabricate a metallic nanostructure on top of the microdisk resonator [128, 129]. The target molecule then should be bound to the surface of the fabricated nanostructure. In the second solution, the target molecule is first bound to a metallic nanoparticle. Then, the metallic nanoparticle is bound to the surface of the microdisk resonator. The small area of the fabricated nanostructures in the first approach leads to a considerable reduction in the binding rate of the target molecules to their surface. On the other hand, the main challenge of the second approach is the variations in the position and orientation of the nanoparticles attached to the resonator surface that may result in a large uncertainty in the nanoparticle-microresonator coupling rate.

In this chapter, I develop a theoretical model for the interaction of the metallic nanoparticles with a high-Q microdisk resonator. I specifically focus on the interactions between colloidally-synthesized metallic nanoparticles with High-Q resonators in a fluidic environment. As an example for the metallic nanoparticles, in this work, I use gold nanorods as they provide the flexibility to tune their resonance wavelength over a

wide range of wavelengths [130]. I investigate the possibility of SERS enhancement using a combined metallic nanoparticle-microdisk resonator and study the possibility of trapping and alignment of gold nanorods in microdisk resonator traps.

6.1 Numerical modeling of the resonant modes in gold nanorods

In contrast to the gold nanospheres, gold nanorods provide a high flexibility in the tuning of their resonance wavelength. By adjusting the geometry of gold nanorods, the longitudinal surface plasmon resonance (LSPR) mode of the nanoparticle can be tuned over a wide range of wavelengths from visible (i.e., 540 nm) to infrared (IR) (i.e., 1400 nm). The first step in the calculation of the nanoparticles properties such as cross-section, field enhancement, and coupling to a microdisk resonator is to find their resonant mode wavelength and mode profile. Different techniques such as the discrete dipole approximation (DDA) [131], generalized multi-pole technique (GMT) [132], and finite difference time domain (FDTD) method [133] have been used to solve for the resonant modes of the nanoparticle. In this work, I have used the FE method to solve the auxiliary symmetric Maxwell equations for the dipole mode of circularly symmetric nanoparticles in the frequency domain. The main advantage of this technique is its ability to provide accurate solutions with relatively low computational cost. The perfectly matched layer (PML) boundary condition is used to prevent reflections at the simulation domain boundaries. The nanoparticle in this analysis is excited by a dipole source. The frequency of the dipole source is swept to scan the desired bandwidth.

The SPR wavelength of the gold nanorods can be tuned in a wide wavelength range by adjusting their geometrical dimensions. For the SERS applications usually it is more desirable to work at NIR wavelengths, where comparing to the visible wavelengths, the

interfering fluorescent emission is much less. Also, gold nanorod resonators can provide a higher absorption quality factor in NIR wavelengths. On the other hand, smaller gold nanoparticles are preferred, as they provide a much longer stability in the microfluidic environments. Figure 6.1 shows the calculated radiation pattern, field pattern, and the normalized polarizability of LSPR mode for two gold nanorods with diameters of 10 nm and 50 nm and lengths of 42 nm and 100nm, respectively. The simulated gold nanorod with smaller dimensions (Figures 6.1(b) and 6.1(c)) has a resonance wavelength at 770 nm with a quality factor larger than 50. The free space polarizability and cross-section along z direction (i.e., α_{zz} and σ_{zz}), and field enhancement factor of this nanorod, at the resonance wavelength, are 2.62×10^{-15} $cm^3\varepsilon_0$, $1.6\times10^{-10}cm^2$, and 199, respectively. The larger gold nanorod (Figures 6.1(d) and 6.1(e)) has a resonance wavelength at 660 nm with a quality factor around 6. (the details of the formulation for the calculation of the surface plasmon nanoparticles cross-sections and polarizabilities are in Appendix B).

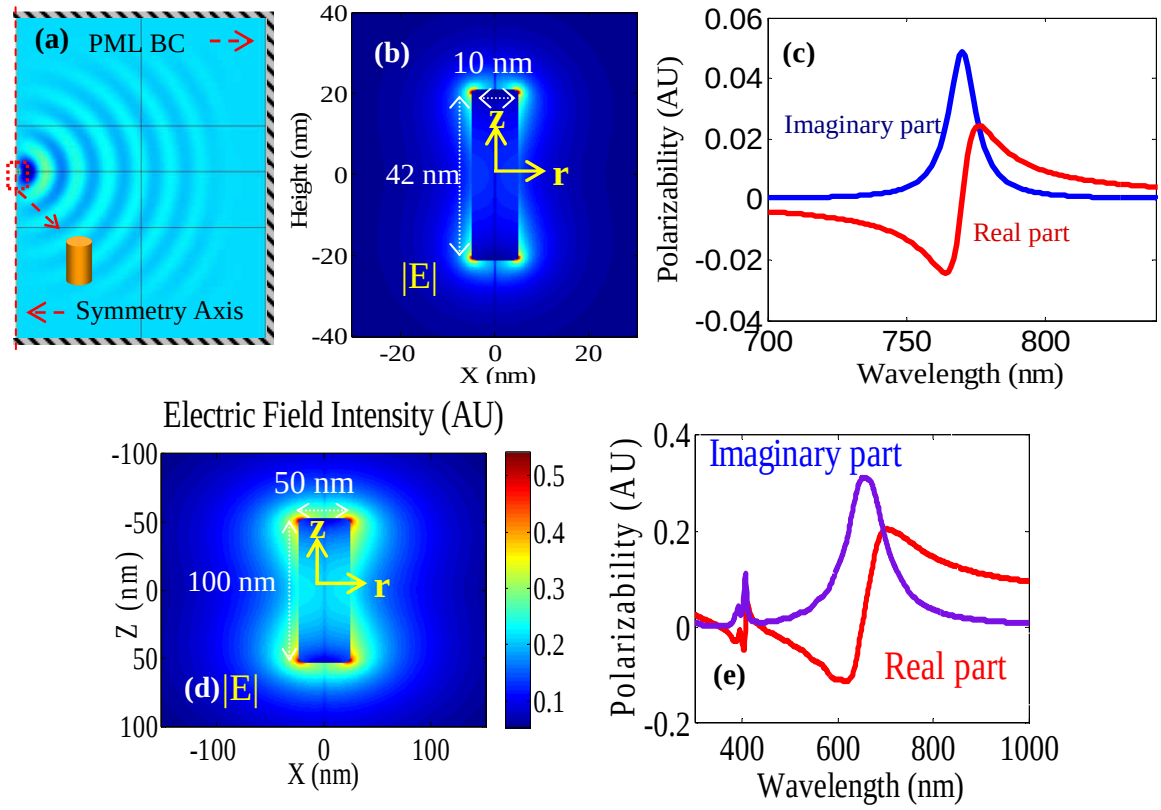

Figure 6.1: Simulation of the resonant mode of two gold nanorods, excited by dipole sources, using axial symmetric FEM wit PML boundary condition (a), schematic of the nanorod rod radiation pattern. (b), and (c) show the normalized electric field pattern (|E|) and the normalized polarizability spectrum of a 10 nm-diameter and 42 nm-long gold nanorod, respectively. (d) and (e) show the normalized electric field pattern (|E|) and the normalized polarizability spectrum of a 50 nm-diameter and 100 nm-long gold nanorod, respectively. In Figure (c) and Figure (e), the real and imaginary components of the nanoparticle normalized polarizability are shown by red and blue curves.

6.2 Waveguide-nanoparticle interactions

The coupling between the resonant mode of a nanoparticle and the guided modes of a waveguide can be modeled using simple coupling mode theory. The equations that govern the coupling between the resonant mode of the nanoparticle (a_{np}) and the forward and backward modes of the waveguide (S^F, and S^B) can be modeled as [25],

$$\frac{da_{np}}{dt} = (-j\delta\omega_{np} - \Gamma_{np}/2 - \kappa_{np}^2)a_{np} + j\kappa_{np}S_{in}^F + j\kappa_{np}S_{in}^B, \tag{6.1}$$

$$S_{out}^{F} = S_{in}^{F} + j\kappa_{np} a_{np}\,, \tag{6.2}$$

and

$$S_{out}^{B} = \lambda S_{in}^{B} + j\kappa_{np} a_{np}\,. \tag{6.3}$$

In the above equations, a_{np} is the amplitude of the surface plasmon resonant mode of the nanoparticle, S_{in}^{F} (S_{in}^{B}) and S_{out}^{F} (S_{out}^{B}) are the forward (backward) input and output signals of the waveguide (Figure 6.2), $\Delta\omega_{np} = \omega_0 - \omega_{np}$ is the detuning between the input light frequency and the surface plasmon resonance frequency of the nanoparticle (ω_{np}), Γ_{np} is the loss rate of the nanoparticle resonant mode, and finally, k_{np} is the coupling coefficient between the waveguide and resonant nanoparticle. The waveguide-nanoparticle coupling coefficient can be found as [24]

$$k_{np} = -\frac{\omega_0}{4}\int_{V_{np}} \Delta\varepsilon_{np} \frac{E_{np}^{*}}{\sqrt{U_{np}}} \frac{E_w e^{-j\beta z}}{\sqrt{P_w}} dV\,. \tag{6.4}$$

In the above coupling integrals, $\Delta\varepsilon_{np}$ is the permittivity perturbation caused by the resonant nanoparticle. Also, U_{np} and P_w represent the stored energy in the nanoparticle and the propagating power of the waveguide guided mode, respectively.

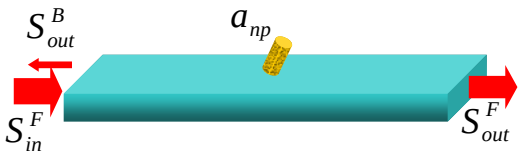

Figure 6.2: Schematic of a waveguide-gold nanorod coupling.

Figure 6.3 shows the coupling coefficient between a gold nanorod (with a diameter of 50 nm and length of 100 nm, similar to the one in Figure 6.1 (d)) coupled to a SiN waveguide on oxide substrate (with a thickness of 200 nm and the width of 500 nm). As it is evident from Figure 6.3, at the maximum coupling rate (when the nanorod touches

the waveguide surface at the point with the maximum electric field), a coupling coefficient (κ_{np}) of $4.25\sqrt{THz}$ can be obtained.

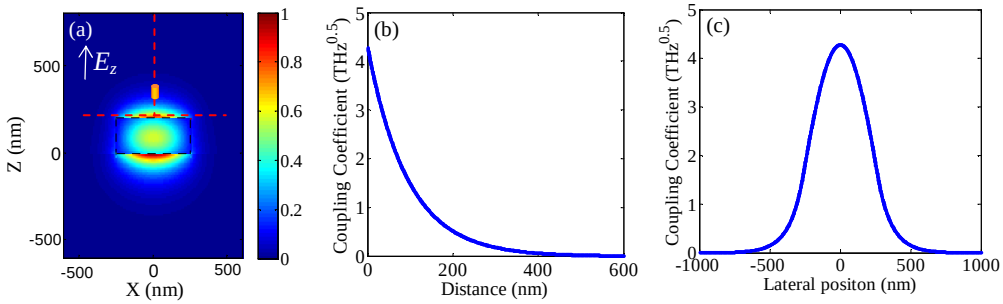

Figure 6.3: The coupling coefficient between a SiN waveguide and a resonant gold nanorod (k_{np}). The width and thickness of SiN waveguide are 500 nm and 200 nm, respectively. The diameter and length of the gold nanorod are 50 nm and 100 nm, respectively. (a) The electric field pattern of the SiN waveguide. (b) and (c), The absolute value of coupling coefficient ($|k_{np}|$) along the vertical and horizontal dashed line shown in (a).

Using Equation 6.1 to Equation 6.3 at the steady state, the resonant nanoparticle field amplitude, and the transmission (T_{np}) and reflection (R_{np}) of the coupled waveguide and the resonant nanoparticle can be found as

$$a_{np} = \frac{+ j\kappa_{np}}{j\delta\omega_{np} + \Gamma_{np}/2 + \kappa_{np}^2} S_{in}^F, \tag{6.5}$$

$$R_{np} = \frac{S_{out}^B}{S_{in}^F} = \left(\frac{-\kappa_{np}^2}{j\delta\omega_{np} + \Gamma_{np}/2 + \kappa_{np}^2} \right), \tag{6.6}$$

and

$$T_{np} = \frac{S_{out}^F}{S_{in}^F} = \left(1 - \frac{\kappa_{np}^2}{j\delta\omega_{np} + \Gamma_{np}/2 + \kappa_{np}^2} \right). \tag{6.7}$$

As it is evident from the Equation 6.5, the efficiency of the coupling from the waveguide to the nanoparticle and the nanoparticle broadening due to the coupling to the waveguide depend on the ratio between the square of the coupling coefficient and the nanoparticle loss rate (i.e., $\kappa_{np}^2/\Gamma_{np}$). In typical structures, $\kappa_{np}^2 << \Gamma_{np}$; therefore, coupling to the waveguide will not cause a significant broadening in the spectral linewidth of the

nanoparticle. Figure 6.4 shows the transmission and reflection spectra for the coupled gold nanorod and SiN waveguide (Figure 6.3), at maximum nanoparticle-waveguide coupling condition ($\kappa_{np} = 4.25\sqrt{THz}$). At this condition, at the resonance wavelength 14 percent of the waveguide input power is coupled to the nanoparticle and lost through scattering and absorption. However, only 0.5 % of the waveguide input power is reflected through coupling to the backward propagating mode of the waveguide. Figure 6.4 (c) show the achieve field enhancement, defined as the ratio of the maximum nanoparticle electrical field strength to the maximum field strength on the top of the waveguide.

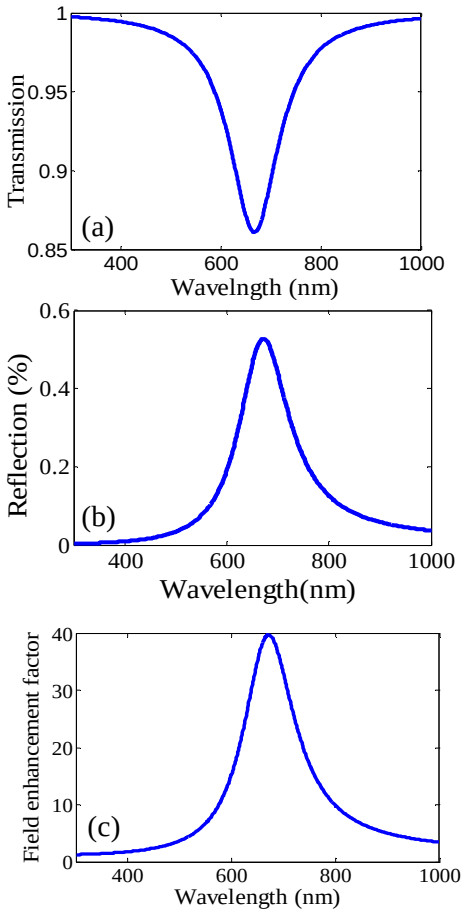

Figure 6.4: (a) and (b), the spectra of the transmission (a) and reflection (b) of a nanoparticle coupled to a waveguide, when nanoparticle is sited on the top of the waveguide at the point with maximum field strength. The nanoresonator and waveguide used for these simulations are the same as Figure 6.3. (c), the maximum field enhancement in the resonator as compared to the field strength on the top of the unperturbed waveguide.

6.3 TWR resonator-nanoparticle interactions

The light interaction with a resonant nanoparticle can be considerably enhanced by using a traveling-wave microresonator to locally enhance the electromagnetic field that is interacting with the nanoparticle. The interactions between a plasmonic nanoparticle and a TWR can be modeled using the coupled-mode equations between the two degenerated modes of the TWR and the surface plasmon resonant mode of the nanoparticle. These coupling equations can be modeled either in space domain using transfer matrix method (TMM) or in time domain using time domain coupled-mode analysis.

6.3.1 Nanoparticle-resonator coupling using transfer matrix method (TMM)

In TMM, the effect of the coupled nanoparticle on the travelling wave in the resonator can be modeled by its frequency dependent transmission, $T_{np}(\omega)$, and reflection, $R_{np}(\omega)$, as it was calculated in the Section 6.2 for the case of a waveguides. Therefore, the amplitude of the resonant CW and CCW propagating modes of the TWR can be calculated by solving the space domain coupled-mode equations as follows:

$$a_{ccw}(\omega) = \lambda\gamma T_{np}(\omega) e^{jk(\omega)L} a_{ccw}(\omega) + \lambda\gamma R_{np}(\omega) e^{jk(\omega)L} a_{cw}(\omega) + jk_{wc} S_{in}^{F}, \tag{6.8}$$

$$a_{cw}(\omega) = \lambda\gamma R_{np}(\omega) e^{jk(\omega)L} a_{ccw}(\omega) + \lambda\gamma T_{np}(\omega) e^{jk(\omega)L} a_{cw}(\omega), \tag{6.9}$$

$$a_{np}(\omega) = \frac{+ j\kappa_{np}}{j\delta\omega_{np} + \Gamma_{np}/2 + \kappa_{np}^{2}} (a_{ccw}(\omega) + a_{cw}(\omega)), \tag{6.10}$$

$$S_{out}^{F} = \lambda S_{in}^{F} - j\kappa_{wc} a_{ccw}, \tag{6.11}$$

and $$S_{out}^{B} = -j\kappa_{wc} a_{cw}. \tag{6.12}$$

By combining Equation 6.5 and 6.7 with Equations 6.8 to 6.12, the amplitude of the resonant modes of the TWR and the nanoparticle can be calculated. The simulation results for a coupled microring resonator-gold nanorod over a wavelength range that

includes several microring resonant modes with different azimuthal orders are shown in Figure 6.5. Figure 6.5 (a) shows the schematic of a coupled microring resonator and gold nanorod. The microring resonator in this simulation has a diameter of 8 μm and the width and thickness of the microring are 500 nm and 200 nm, respectively (similar to the waveguide in Figure 6.3). The nanoparticle used in this simulation is also the same as the one used in Figure 6.3 (a gold nanorod with a diameter and length of 50 nm and 100 nm, respectively). The microring resonator coupling to the waveguide is adjusted to maximize the input light coupling to the microring resonator at the microring resonance wavelengths close to the gold nanorod resonance wavelength. The microring resonator intrinsic and coupling Qs in this simulation are *20,000* and *5,000*, respectively.

Figure 6.5 (b) to Figure 6.5 (f) show the stored energy in the nanorod resonator, the stored energy in the CCW mode (corresponding the forward propagation in the waveguide) of the microring resonator, the stored energy in the CW mode (corresponding the backward propagation in the waveguide) of the microring resonator, the transmission of the coupled system, and the reflection of the coupled system, respectively. Figure 6.5 (b) shows the stored energy in nanorod resonator versus the input laser wavelength. In this figure, the stored energy envelope corresponds to the nanoparticle resonance line-shape, which is modulated by the microring resonator resonances. Coupling between the nanoresonator and waveguide may result in the broadening of the nanoparticle resonance. The high confinement of the guided optical mode in the waveguide results in a high density of the guided modes in the waveguide. Therefore, as the resonator approaches the surface of the waveguide, the coupling between the nanoparticle and the waveguide modes results in a higher rate of loss for the nanoresonator and, therefore, broadening of

the nanoparticle line-shape. On the other-hand, the nanoparticle-induced loss due to the scattering loss and coupling to the degenerated mode in the cavity results in the broadening of the line-shape of the TWR resonant modes.

Figure 6.5 (c) shows the stored energy at the CCW mode of the microring resonator. As is evident from this figure, the total stored energy in the resonator in reduced when the resonator is in resonance with the nanoparticle as compared to the off-resonance wavelengths. This reduction in the CCW resonant mode energy is an indication of the microring resonator loading by the interactions with the resonant nanoparticle. The increased loss rate of the CCW mode of the resonator is due to the power absorbed or scattered by the nanoparticle and coupling to the degenerated CW mode of the microring resonator through the nanorod. Figure 6.5 (d) shows the energy in the CW mode of the resonator. As can be seen from this figure, coupling between the CW and CCW mode of the resonator is considerably enhanced at the wavelengths close to the resonance wavelength of the nanoparticle. Even though the coupling between the two degenerated mode is considerably enhanced at the nanorod resonance, the coupling rate is still less that the loss rate of the CCW mode and the total energy of the CW mode does not exceed 20% of the CCW mode energy. Therefore, by definition the CCW and CW modes of the microring resonator, are weakly coupled. This is in contrast with the strong coupling regime, where the coupling rate is much larger than the loss rate and the two degenerated mode carry similar powers in the resonator. The weak coupling condition is mainly due to the relatively large size of the gold nanorod and relatively low coupling Q of the microring resonator.

Figure 6.5 (e) and Figure 6.5 (f) show the transmission and reflection spectrum of the coupled nanorod-microring resonator. The coupling between the waveguide and the microring resonator is adjusted to achieve close to critical-coupling at the wavelengths close to the nanorod resonance; therefore, at the off-resonance wavelength, the microring resonator is over-coupled. The critical coupling condition at the nanorod resonance indicates the input power of microring resonator has been absorbed, scattered, or coupled to the reflection mode by the nanorod resonator with 100% efficiency.

While the coupled microring-nanorod transmission reaches its minimum at the resonance condition, its reflection reaches its maximum value of about 25% (corresponding to -6 dB) at the resonant condition. This high reflection is in contrast to the only 0.5 % reflection induced by a nanoparticle interacting with a waveguide (Figure 6.4). The high coupling to the reflection mode is an indication of high coupling between the gold nanorod and the resonant mode of the resonator. Since all the input power of the microring is coupled to the nanorod and then absorbed, scattered, or coupled to the reflection mode, a reflection coefficient of 25% also mean that the loss rate of the nanorod is increased by 33% at the resonance condition. Figure 6.6 shows the shift in the resonance wavelength of the coupled microring resonator, induced by the gold nanorod interaction. As is evident from Figure 6.6, the induced resonance shift depends on the nanoparticle resonance detuning from the resonator resonance wavelength. The resonant nanoparticle-induced shift is zero at the zero wavelength detuning and can cause both red and blue shifts at different detuning in respect to the nanorod resonance wavelength. This is in contrast to the non-resonant dielectric nanoparticle perturbations, which always result in a red shift in the resonance wavelength of the resonator.

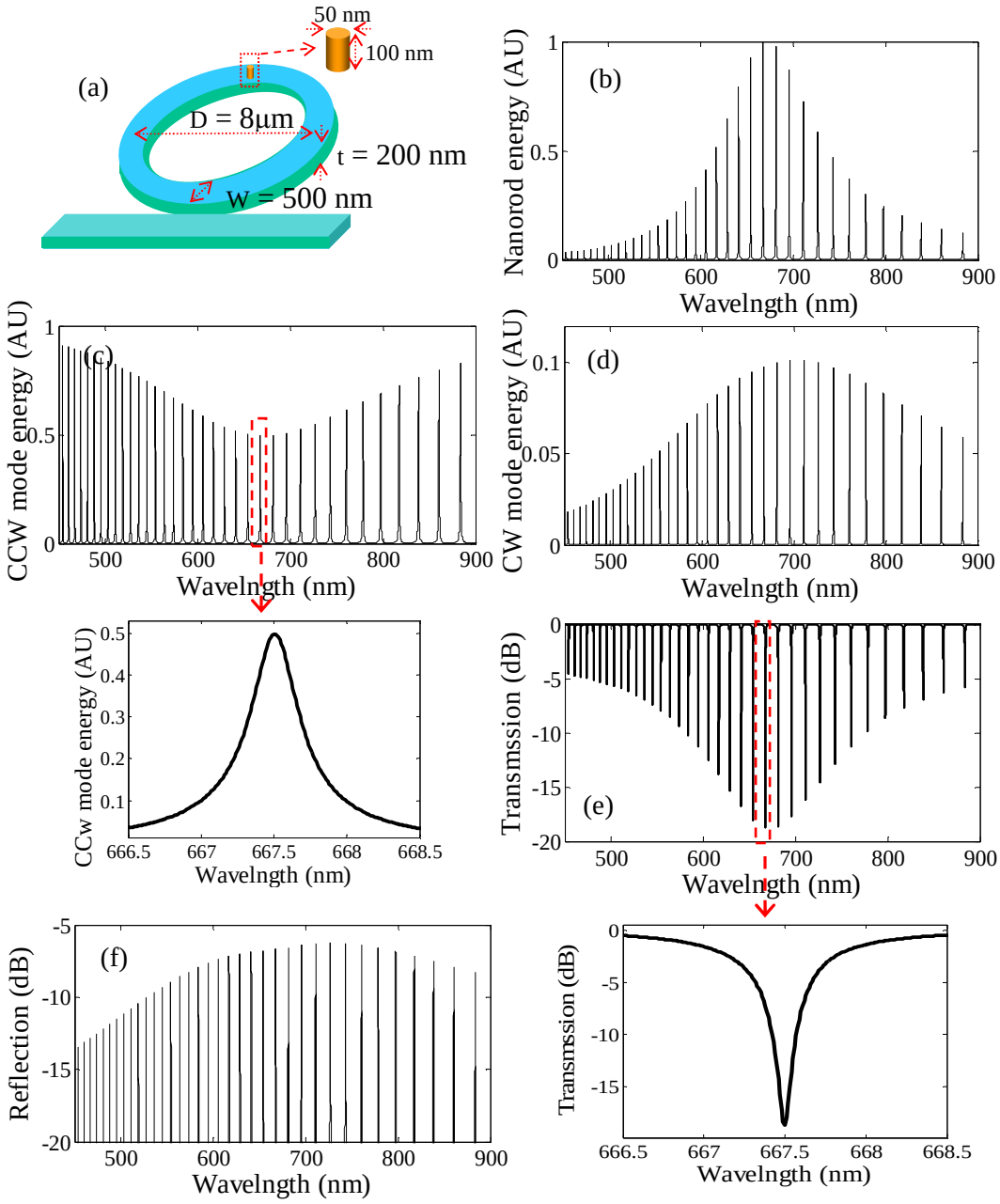

Figure 6.5: The interaction of a gold nanoparticle with a SiN microring resonator. Figure (a) shows the schematic of the coupled microring resonator and gold nanorod. The nanoparticle of this figure is the same nanoparticle as the one in Figure 6.4. The SiN microring resonator is this simulation has a diameter, width, and thickness of 8 μm, 500 nm, and 240 nm, respectively. Figures (b) to (f) show the stored energy in the nanorod resonator, the stored energy in the CCW mode (corresponding the forward propagation in the waveguide) of the microring resonator, the stored energy in the CW mode (corresponding the backward propagation in the waveguide) of the microring resonator, the transmission of the coupled system, and the reflection of the coupled system, respectively.

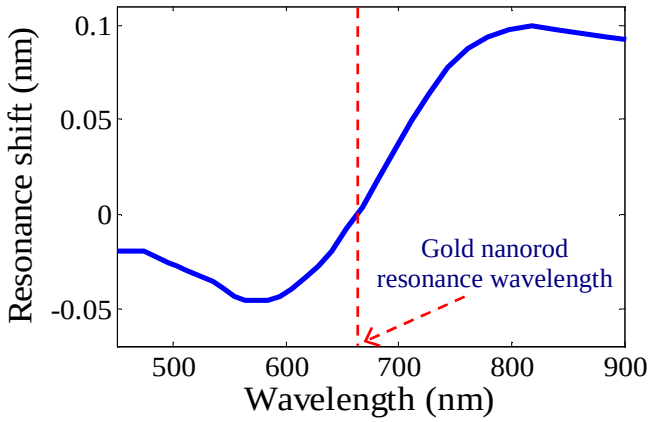

Figure 6.6: The shift in the resonance wavelength of the microring resonator coupled with the gold nanorod, as compared to the original microring resonator resonance wavelength.

6.3.2 Nanoparticle-resonator coupling using time domain coupling analysis

While TMM provides a powerful technique for the analysis of the TWRs and resonant nanoparticle over a wide bandwidth, time domain analysis provides a more general formulation that can be used for any resonator geometry at wavelengths close to the resonator resonance wavelength. Furthermore, the time domain analysis directly deals with the stored energy in the resonator and nanoparticle and provides more insights on the effect of different parameters on the interactions between the resonator and the nanoparticle. Assuming the input signal is coming from the waveguide coupled to the microdisk resonator, the equations that govern the coupling between the plasmonic nanoparticle and the resonant modes of the microdisk resonator can be written as

$$\frac{da_{ccw}}{dt} = \left(- j\delta\omega - \frac{\Gamma_c}{2} \right) a_{ccw} + j\kappa^* a_{np} + j\sqrt{\Gamma_{in}} S_{in},$$

$$\frac{da_{cw}}{dt} = \left(- j\delta\omega - \frac{\Gamma_c}{2} \right) a_{cw} + j\kappa^* a_{np}, \tag{6.13}$$

and

$$\frac{da_{np}}{dt} = \left(- j\left(\delta\omega + \Delta\omega_{np}\right) - \frac{\Gamma_{np}}{2} \right) a_{np} + j\kappa a_{ccw} + j\kappa a_{cw}.$$

In the above equation, a_{np} is the amplitude of the surface plasmon resonant mode of the nanoparticle, κ is the coupling rate between the nanoparticle and the microdisk resonator modes, $\Delta\omega_{np} = \omega_c - \omega_{np}$ is the detuning between the resonance frequency of the microdisk resonator and the surface plasmon resonance frequency of the nanoparticle (ω_{np}), and finally Γ_{np} is the loss rate of the nanoparticle resonant mode. All other parameters are similar to those of Equation 3.1 in Chapter 3. In contrast to the case of a non-resonant nanoparticle that we studied in Chapter 3, the coupling between the resonant modes of the microdisk is dominantly through the nanoparticle resonance ($\kappa >> \beta$). Therefore, in the above equations, the effect of the non-resonant coupling between the CW and CCW modes of the microdisk through the nanoparticle are ignored. The nanoparticle-microdisk resonator coupling rate (κ) can be found as

$$\kappa = -\frac{\omega}{2}\frac{\int_{V_{rod}} (\varepsilon_m - \varepsilon_i)\, E_c(r)\, E_{np}^*(r) dV}{\sqrt{\varepsilon_c V_c}\left|E_c^{\max}\right|\sqrt{\varepsilon_i V_{np}}\left|E_{np}^{\max}\right|}. \tag{6.14}$$

In the above equation, the integral in the numerator is over the nanoparticle volume (V_{rod}), ε_m and ε_i are the nanoparticle and the microdisk cladding environment permittivity, respectively, and $E_{np}^*(r)/\left|E_{np}^{\max}\right|$ is the ratio of the nanoparticle electric field at the position *r* to the maximum absolute value of the nanoparticle electric field. Finally, V_{np} is the nanoparticle mode volume, which can be calculated using the following formula:

$$V_{np} = \frac{\int \bar{\varepsilon}(\omega, r)\left|E_{np}(r)\right|^2 dV}{\varepsilon_i\left|E_{np}^{\max}(r)\right|^2}. \tag{6.15}$$

In the above equation, the integral in the numerator is over the whole space and $\bar{\varepsilon}(\omega, r)$ is the effective dispersive permittivity, i.e., $\bar{\varepsilon}(\omega, r) = \partial\omega\varepsilon(\omega, r)/\partial\omega$ [134].

Using Equation 6.13, when the microdisk resonator and the plasmonic nanoparticle have zero detuning (i.e., $\Delta\omega_{np} = 0$), the amplitude of the nanoparticle resonant mode can be found as

$$a_{np} = \frac{-\kappa\sqrt{\Gamma_{in}}}{-\delta\omega^2 + 0.25\Gamma_c\Gamma_{np} + 2\kappa^2 + j0.5\delta\omega\Gamma_{np}} S_{in}. \tag{6.16}$$

Considering the fact that the nanoparticle loss rate is much larger than the microdisk resonator loss rate and the microdisk resonator-nanoparticle coupling rate (i.e., $\Gamma_c, \kappa << \Gamma_{np}$), the frequency detuning ($\delta\omega$) that maximizes the coupled power to the nanoparticle [i.e., $\delta\omega = Arg_{\delta\omega}\max(|a_{np}|^2)$] is zero (i.e., $\delta\omega = 0$). The couple stored energy in the nanoparticle, thereby, is

$$\left|a_{np}\right|^2 = \frac{\kappa^2\Gamma_{in}}{(0.25\Gamma_c\Gamma_{np} + 2\kappa^2)^2} P_{in}. \tag{6.17}$$

Using Equation 6.17, the optimal coupling rate (κ_{opt}), that maximizes the energy stored in the surface plasmon nanoparticle, can be found as $\kappa_{opt} = \sqrt{\Gamma_c\Gamma_{np}/8}$, and the stored energy in the nanoparticle, at the optimum coupling condition, can be written as

$$\left|a_{np}\right|^2 = \frac{\Gamma_{in}}{2\Gamma_c\Gamma_{np}} P_{in}. \tag{6.18}$$

Now, let's consider two different coupling scenarios. In the first case, assume the waveguide is critically coupled to the unperturbed resonator [i.e., $\Gamma_c = (\Gamma_0 + \Gamma_{in}) = 2\Gamma_{in}$ where Γ_0 is the intrinsic loss rate of the microdisk resonator]. In this case, the stored

energy in the nanoparticle (U_{np}) and the total power extinction through the nanoparticle (P_{np}) can be calculated as

$$U_{np} = \frac{Q_{np}}{4\omega} P_{in} \Rightarrow P_{np} = \Gamma_{np} \frac{Q_{np}}{4\omega} P_{in} = \frac{1}{4} P_{in} . \tag{6.19}$$

As is clear from the above equation, in this case one fourth of the input power (~25%) is coupled to and scattered or absorbed by the nanoparticle. In the second case, assuming $\Gamma_0 << \Gamma_{in}$, we have:

$$U_{np} = \frac{Q_{np}}{2\omega} P_{in} \Rightarrow P_{np} = \Gamma_{np} \frac{Q_{np}}{2\omega} P_{in} = \frac{1}{2} P_{in} . \tag{6.20}$$

The coupled power to the nanoparticle, in this case, is twice that of previous case and 50% of the input power is coupled to and scattered or absorbed by the nanoparticle. Comparing this with the effective cross-section of the nanoparticle in free space, this corresponds to a huge enhancement. To obtain the optimal condition, the coupling between the nanoparticle and the microdisk resonator should be adjusted to its optimal value (i.e., κ_{opt}). One solution to adjust the coupling rate (κ) is to put a spacer layer (e.g., a thin layer of oxide) on top of the microdisk resonator and adjust the thickness of this layer to achieve the desired coupling. As an alternative approach, the waveguide-microdisk resonator coupling can be adjusted to achieve the optimal operation at the maximum coupling ($\kappa_{\max}$), when the nanoparticle is directly bound to the microdisk resonator surface. The optimal input coupling (Γ_{in}^{Opt}), in this case, can be calculated as $\Gamma_{in}^{Opt} = 8\kappa_{\max}^2 / \Gamma_{np}$.

6.4 Simultaneous trapping and SERS sensing

Although the large refractive index of metallic nanoparticles (e.g., gold nanorods) enables to trap small metallic nanoparticles in infrared wavelength [135,136], stable trapping of gold nanoparticles in three dimensions is difficult. There are a few reports on plasmon resonance-based trapping of gold nanoparticles using conventional optical trapping systems [137, 138]. Simultaneous trapping and SERS sensing requires the gold nanoparticle to be trapped in the wavelengths close to the plasmon surface resonance of the nanoparticle. At this wavelength range, the strong surface plasmon resonance of the metallic nanoparticles results in a large enhancement in the nanoparticle polarizability. However, as we mentioned, the interaction between the gold nanoresonator and the TWR resonator at the nanoresonator resonance wavelength does not lead to any detuning in the resonance wavelength of the TWR (refer to Figure 6.6). Therefore, no gradient force is exerted on the plasmonic nanoparticle (refer to Equation 5.1 in Chapter 5). This result was already expected, as the nanoparticle polarizability at the resonance wavelength is purely imaginary. However, while the real part of the nanorod polarizability at its resonance frequency is zero, it can take large positive or negative values at small detuning from the nanoparticle surface Plasmon resonance. As a result, the resonance wavelength of a resonator, coupled with a resonant nanoparticle, may undergo a positive or negative resonance wavelength shift (Figure 6.6) that can lead to an attractive or repulsive force on the nanoparticle. Again, using Equation 21 and assuming $\gamma_c << \gamma_{np}$ and $\delta\omega, \gamma_c << \Delta\omega_{np}$ we have:

$$a_{np} = \frac{-\kappa\sqrt{\Gamma_{in}}}{-\delta\omega\Delta\omega_{np} + 0.25\Gamma_c\Gamma_{np} + 2\kappa^2 + j0.5\delta\omega\Gamma_{np} + j0.5\Delta\omega_{np}\Gamma_c} S_{in} . \qquad (6.21)$$

The input laser source detuning from the microdisk resonator (i.e., $\delta\omega$), corresponding to the maximum nanoparticle energy [i.e., $\delta\omega = Arg_{\delta\omega}\max(|a_{np}|^2)$], can be derived as

$$\delta\omega = \frac{2\kappa^2\Delta\omega_{np}}{(\Delta\,\omega_{np}^2 + 0.25\Gamma_{np}^2)}\ . \tag{6.22}$$

As can be seen from this equation, the detuning in the microdisk resonator resonance frequency has the same sign as the nanoparticle resonance detuning $\Delta\omega_{np}$. Therefore, to achieve an attractive force, we should have, $\Delta\omega_{np} = \omega_c - \omega_{np} < 0$ (refer to Equation 5.5 in Chapter 5). This corresponds to a red detuning of the of the microdisk resonator resonance wavelength in respect to the nanoparticle resonance. Assuming a detuning equal to half of the nanoparticle linewidth (i.e., $\Delta\omega_{np} = -0.5\Gamma_{np}$), the induced shift in the resonance frequency of the microdisk resonator is

$$\delta\omega = -\frac{2\kappa^2}{\Gamma_{np}}. \tag{6.23}$$

The stored energy in the nanoparticle, also, can be calculated as

$$U_{np} = |a_{np}|^2 = \frac{\kappa^2\,\Gamma_{in}}{2\,(\kappa^2 + 0.25\Gamma_{np}\Gamma_c)^2}\,P_{in}. \tag{6.24}$$

The optimal coupling rate, in this case, is $\kappa_{opt} = \sqrt{\Gamma_c\Gamma_{np}}\,/\,2$. The stored energy in the nanoparticle and the total power extinction through the nanoparticle can be calculated as

$$U_{np} = |a_{np}|^2 = \frac{1}{2\Gamma_{np}} \Rightarrow P_{np} = \Gamma_{np}U_{np} = \frac{1}{2}P_{in}. \tag{6.25}$$

Although the required coupling between the nanoparticle and the microdisk resonator, I this case, is higher than that of the case with zero detuning, at the optimum condition (for

the over-coupling condition, i.e., $\Gamma_c \approx \Gamma_{in}$) the same fraction of the input power (i.e., 50%) is coupled to the nanoparticle.

6.4.1. Optical force and nanoparticle trapping and alignment

The plasmonic nanoparticle-induced shift in the microdisk resonator resonance frequency results in a gradient force that attracts the nanoparticle toward the microdisk resonator surface. The amount of the nanoparticle-induced resonance shift, using the single point approximation can be calculated as,

$$\delta\omega = -\frac{\Re(\alpha)\left|E_c(r_0)\right|^2}{2\varepsilon_c V_c \left|E_c^{\max}\right|^2}\omega\,. \tag{6.26}$$

At the optimal coupling condition (i.e., $\kappa_{opt} = \sqrt{\Gamma_c \Gamma_{np}}/2$) the trap working energy (i.e., $W_{trap} = -\Delta U_c$) can be obtained as

$$W_{trap} = \frac{\delta\omega}{\omega}U_c = \frac{\Gamma_c}{\omega}\frac{2Q}{\omega}P_{in} = \frac{2P_{in}}{\omega}\,. \tag{6.27}$$

The polarizability of non-spherical or birefringent nanoparticles depends on the exciting field polarization. Therefore, perturbation in the electrical field energy depends on the nanoparticle orientation in the field. This dependence leads to a torque, which tends to align the main nanoparticle polarizability axis with the polarization of the electric field [139]. Gold nanorods at their longitudinal surface plasmon resonance have a strongly polarization-dependent polarizability, as they only can be excited with the light polarization, whose electric field is along the nanoparticles axis. This phenomenon has been used to demonstrate the simultaneous optical trapping and alignment of gold nanorods in conventional optical trapping systems [137].

When a nanorod interacts with an external field, because of its anisotropic polarizability, it undergoes an optical torque (τ). The exerted torque per unit volume on a nanoparticle in an electromagnetic field can be found as [140]

$$\tau = P \times E^{*} + r \times (P.\nabla)E^{*}, \tag{6.28}$$

where E is the incident electric field and P is the induce polarization in the nanoparticle. For a small nanoparticle, the second term on the right side of the above equation is negligible. By integrating over a nanoparticle using single point approximation we have:

$$\tau = (\alpha E) \times E^{*}, \tag{6.29}$$

where α is the nanoparticle polarizability. Figure 6.7 shows a schematic of a nanorod in the near-field of a microdisk resonator. The exerted torque on the nanoparticle in the radial-vertical plane ($\tau_{\xi\eta}$) can be found as

$$\tau_{\xi\eta} = \Re(E_{\xi} E_{\eta}^{*}) \, \Re(\alpha_{\xi} - \alpha_{\eta}) \ , \tag{6.30}$$

where α_{ξ} and α_{η} are the longitudinal and transverse components of the polarizability, respectively. Also E_{ξ} and E_{η} are the electric field components along and normal to the nanorod main axis. At the longitudinal surface plasmon resonance (LSPR) modes the longitudinal components of the polarizability is much larger than its transverse counterpart (i.e., $\alpha_{\xi} >> \alpha_{\eta}$). Therefore, replacing the electrical field components based on the input power and the microdisk resonators parameters, $\tau_{\xi\eta}$ can be calculated as,

$$\tau_{\xi\eta} = \frac{Q_c \left|E_c(r)\right|^2}{\varepsilon_c \omega V_c \left|E_c^{\max}\right|^2} Sin\,(2\,\theta - \varphi(r)) \, \Re(\alpha_{\xi}) \, P_{in} \ , \tag{6.31}$$

where $\left|E_c(r)\right|$ is the magnitude of the microdisk resonator electric field and $\varphi(r)$ is the angle between electric field vector and vertical direction, at the nanorod location. In the

above equation, θ is the angle between the nanorod main axis and the vertical direction (refer to 13). Combining Equation 6.26 and Equation 6.31, the exerted torque on the gold nanoparticle, in term of the induce resonance wavelength shift, can be calculated as

$$\tau_{\xi\eta} = -\frac{2Q_c}{\omega}\frac{\delta\omega}{\omega} Sin(2(\theta-\varphi))P_{in} \ . \tag{6.32}$$

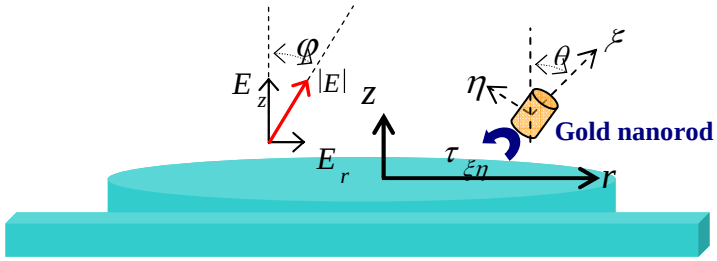

Figure 6.7: Schematic of a gold nanorod in a SiN microdisk resonator optical trap. The optical mode in the microdisk resonator exerts a torque on the nanorod to align its ling axis with the direction of the electrical field in the microdisk resonator.

6.4.2. Numerical investigation of the interaction of a gold nanorod with a SiN microdisk

To provide a numerical evidence for the possibility of the gold nanorod trapping, alignment, and field enhancement in a microdisk resonator trap, the interaction of a gold nanorod and a SiN microdisk resonator is simulated. The microdisk resonator, in this study, is a 12 μm diameter microdisk, fabricated on a SiN on oxide wafer with a top SiN layer thickness of 240 nm. The resonant modes of the microdisk resonator are calculated by solving auxiliary symmetric Maxwell equations using FE method. Figure 6.3(a) shows the mode profile of the first order radial TM mode (main component of the electric field is in the vertical direction) of the SiN microdisk at λ_c=780 nm (corresponding to an azimuthal mode order on 77). The gold nanoparticle, in this case study, is a 10 nm diameter and 42 nm long gold nanorod with a SPR at λ_{np}=770 nm (refer to Figure 6.1). The detuning between the SiN microdisk resonator and the gold nanorod, in this case, is

$0.83\Gamma_{np}$ (i.e., $\Delta\omega_{np} = -0.83\Gamma_{np}$), which is slightly higher than the optimum detuning. Using Equation 6.25 and Equation 6.26, it can be shown that the optimum coupling rate, in this case, can be found as $\kappa_{opt} = 0.678\sqrt{\Gamma_c\Gamma_{np}}$. Figure 6.8 (b) shows the microdisk resonator-gold nanorod coupling rate as a function of the gold nanorod position. In the simulations for this figure, the main axis of the gold nanorod is assumed to be aligned with the vertical direction. At the maximum coupling rate (i.e., $\kappa_{\max} \approx 1.6THz$), the optimum loaded Q of the microdisk resonator ($Q_c^L \approx \omega/\Gamma_{in}$) is about 30k. The intrinsic Q of the microdisk resonator is assumed to be considerably higher than this (e.g., $Q_i > 150k$). At the maximum coupling condition, the microdisk resonator detuning, caused by the gold nanorod perturbation, is about 20 pm. Figure 6.8(c) and 6.8 (d) show the lateral and vertical forces exerted on the gold nanorod, assuming $Q_c^L = 30k$ and the input laser power is 100 μW. As can be seen from Figure 6.3, there is only a single strong optical trap on top of the microdisk. For this optical trap, trap stability factors, as large as 15, can be obtained, with input laser power levels as low as 100 μW. The nanoparticle alignment strength can be quantified by nanorod alignment deviation, caused by the Brownian motion ($\delta\theta$). Similar to Equation 5.9 in Chapter 5, the nanoparticle alignment root mean square alignment deviation (RMSAD) ($\sqrt{\langle\delta\theta^2\rangle}$) can be found as

$$\sqrt{\langle\delta\theta^2\rangle} = \sqrt{\frac{k_B T}{k_\theta}}, \tag{6.40}$$

where k_θ is the nanorod alignment trap spring constant, which can be found as (Equation 6.32)

$$k_\theta = \frac{4Q_c}{\omega}\frac{\delta\omega}{\omega}P_{in}. \tag{6.41}$$

Using the same parameters as before (i.e., maximum coupling rate condition with Q_c=*30k* and P_{in} = 100 μW), the nanorod RMSAD in the trap is about 10˚. A misalignment of 10˚ results in only 3% reduction in the microdisk resonator-nanorod coupling. By increasing the input power to 1mW, the nanorod RMSAD in the trap will further reduce to about 3˚.

Combining the field enhancement in the gold nanorods and the microdisk resonator-enhanced effective cross-section of the gold nanorods, single molecule Raman efficiencies in the order of 10^{-9} can be obtained. This considerably relaxes the input laser power and the integration time requirements for the SERS-based single molecule detection.

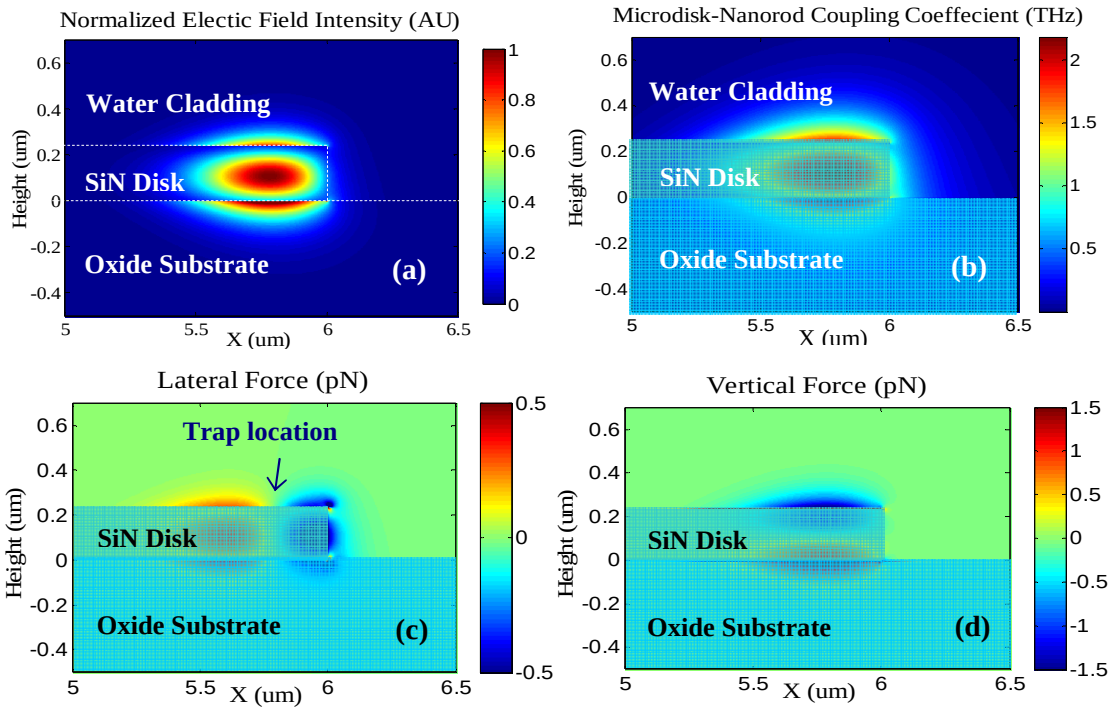

Figure 6. 8: A gold nanorod in a SiN microdisk resonator optical trap. (a): The electric field intensity profile of the first order radial TM mode (main component of the electric field is in the vertical direction) of the SiN microdisk at λ=780 nm. (b): The microdisk resonator-gold nanorod coupling rate as a function of the gold nanorod position. The main axis of the gold nanorod is assumed to be aligned with the vertical direction. (c), (d): Lateral and vertical components of the gradient force exerted on the gold nanorod. This figures correspond to a loaded quality factor of 30k for the SiN microdisk resonator (i.e., $Q_c^L = 30k$) and an input laser power of 100 μW.

6.5 Conclusions

In this chapter, I studied the interactions between a resonant nanoparticle and a traveling-wave resonator. I developed a simple model based of axial symmetric finite element method for the calculation of the resonance mode of plasmonic nanorods. I studied the interaction of a gold nanorod with an integrated travelling-resonator using both space domain and time domain techniques and conditions to optimize the field enhancement in gold nanorods. Finally, the possibility of simultaneous trapping and SERS sensing in microdisk resonator traps was investigated.

CHAPTER 7

Future Directions

The main focus of this PhD research has been on the physics, modeling, and implementation of different applications based on light-matter interaction in the vicinity of high-Q resonators in SOI and SiN platforms. In the continuation to or as an extension of the work in this thesis, there are many interesting research directions that can be suggested as future directions. In this chapter, I present a list of a few of the suggested future research project/directions.

7.1. Near-field characterization of the interaction of a high-Q resonator with a resonant nanoparticle using NSOM system

In this thesis, we have developed a model for the interaction of a resonant nanoparticle with a high-Q resonator. While our main application is the interaction of a colloidal gold nanoparticle with a microdisk resonator, the same interactions can be studied using a controlled nanoparticle. In this schema, an AFM tip with a metallic nanoresonator at its tip is used. The coupling between the nanoparticle and the microdisk resonator can be controlled by controlling the distance between the AFM tip and the micro-resonator surface. The effect of the nanoparticle-microresonator interactions on the coupled waveguide-microresonator transmission amplitude and phase will be investigated. To comply with our main target application for SERS sensing at NIR and visible wavelengths, at the first step the current characterization system should be modified to operate at NIR or visible wavelengths. The AFM probe with a nanoparticle at its tip can

be fabricated by either direct fabrication of the nanoparticle at the tip of the AFM probe or by attaching a colloidally fabricated nanoparticle to the tip of an AFM tip.

7.2. Near-field characterization of optical force in high-Q microdisk resonators

Similar to the case of a nanoparticle, when an AFM/ NSOM tip approached to the near-field region of a high-Q the interaction between the tip and optical field in the micro-resonator may lead to an attractive or repulsive force on the tip. Therefore, the NSOM tip can be used as a controllable perturbation that can be used to monitor the optical forces at the near-field of a microdisk resonator. Although AFM systems have been extensively used for the characterization of the surface forces [141, 142], the minimum measurable force is limited by the thermal noise and the measurement of small optical forces that are usually in the range of a few piconewtons is quite challenging. I propose a technique based on the resonant energy transfer to the AFM tip, which can improve the force measurement sensitivity.

The proposed technique is based on resonance excitation of mechanical vibrations of an AFM tip using the optical forces of a high-Q resonator. The sensitivity of the proposed force measurement technique is mainly limited to the AFM tip vibrations, caused by the thermal noises. To calculate the force measurement sensitivity we calculate the amount of the coupled energy from the optical forces to the mechanical vibrations in the AFM tip and compare it with the amount of the thermal noise energy. The gradient optical force is proportional to the input optical power. Therefore, assuming a modulated input signal [$P_{in} = P_0\ (1+\cos(\omega_m t\ ))\ /\ 2$], we have:

$$F_z = F_0\ (1+\cos(\omega_m t))/2\ . \qquad (7.1)$$

In the above equation, F_0 is the steady state optical force in the vertical direction that corresponds to the input power P_0 and ω_m is the modulation angular frequency of the input laser (i.e., the resonance angular frequency of the AFM tip). Assuming the tip is vibrating at the resonance frequency ($f_m = \omega_m / 2\pi$) with a small vibration amplitude z_r ($z_r <<$ optical field delay length), the vertical force remains almost constant in the whole vibration period. Therefore, the average coupled energy from the optical field to the AFM tip (P_{in_M}) can be written as

$$P_{in\_M} = \langle F_z v_z \rangle_t = \omega_m z_r F_0 / 4 . \tag{7.2}$$

The total stored mechanical energy in the AFM tip at the resonance frequency (E_{T_M}) also can be written as

$$E_{T\_M} = \frac{k_m z_r^{\,2}}{2}, \tag{7.3}$$

where k_m is the AFM tip spring constant. The stored energy and the average input power of the AFM tip are related by the tip quality factor (Q_m):

$$E_{T\_M} = P_{in\_M} \frac{2Q_m}{\omega_m} . \tag{7.4}$$

Combining Equation (7.2) to (7 4), the amplitude of the mechanical vibrations, induced by the optical force, can be calculated as

$$z_r = F_z \frac{Q_m}{k_M} . \tag{7.5}$$

The force resolution of the AFM tip is limited to the thermal noise induce energy $P_{Th} = 0.5 k_B T$. Therefore, the amplitude of the vibrations induced by the thermal

noise (δz_{Th}) can be calculated as $\delta z_{Th} = \sqrt{k_B T / k_m}$. Finally, the resolution of the AFM system for the characterization of the optical forces (F_r) can be calculated as

$$F_r = \frac{\sqrt{k_B T}\sqrt{k_m}}{Q_m}. \tag{7.6}$$

Assuming a spring constant $k_m = 1N/m$ and quality factor of $Q_m = 500$ (typical numbers for the currently available AFM tips), a force measurement resolution less than 0.15 pN can be obtained. This corresponds to AFM tip vibration amplitude of 0.075 nm.

Figure 7.1 shows the schematic of the characterization setup for the near-field optical force measurement. In this schema, the wavelength of the tunable laser source is tuned to the resonance wavelength of the microdisk resonator. The laser light is amplified using an EDFA and modulated using a modulator at a frequency close to the mechanical resonance frequency of the AFM tip. The AFM tip scans the surface of the microdisk resonator in the tapping mode. The frequency of the tip excitation, in the tapping mode, is selected to be slightly different from the laser modulation frequency. When the tip is in the near-field of the microdisk resonator, the optical force excites the mechanical vibrations of the resonating tuning fork attached to the tip. Then, the amplitude of the induced tip vibrations can be measured either from the AFM piezoelectric feedback signal or from the variation in the transmission phase of the coupled waveguide microdisk resonator, caused by the tip perturbation. The measurement of the variation in the transmission of the microdisk resonator provides a higher signal to noise ratio (SNR) as compared to the piezoelectric feedback signal.

A lock-in amplifier is used to lock the output optical signal to the laser modulation frequency to suppress the effect of the noise and out of band vibrations (i.e., vibrations at

the tip tapping frequency). An AFM tip with the desired size is selected to achieve the maximum optical force. The force measurement sensitivity of this system is inversely proportional to the square root of the AFM tip stiffness factor (k); therefore, a relatively low-k tip should be used for this experiment.

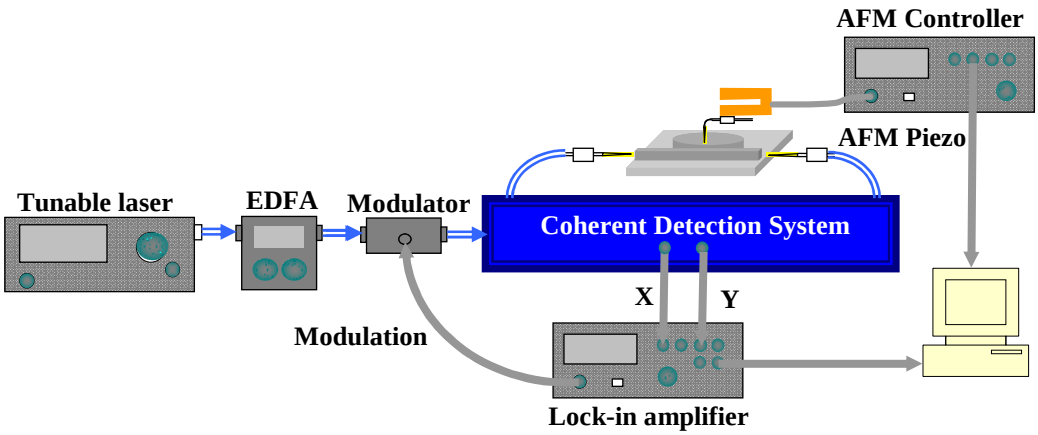

Figure 7.1: Schematic of the characterization setup for near-field optical force measurement.

7.3. Differential refractive index sensing based on laser locking

Figure 7.2 shows the schematic of the measurement set up for the characterization of refractive index sensing using a coherent detection scheme. In this architecture, a single side band (SSB) optical modulator modulates the laser input signal to generate two optical tones (i.e., carrier and signal) separated by frequency shift equivalent to the modulator frequency. The carrier and the signal tone are then locked to the reference and sensing resonators, respectively, by adjusting the laser wavelength and the modulation frequency of the modulator using a phase-locked loop. The shift in the resonance wavelength of the sensing resonator can be measured by monitoring the changes in the frequency of the RF signal driving the SSB modulation, which corresponds to the frequency difference between the sensing and reference resonators. The application of this locking technique compensates for the effect of the laser wavelength drift and the

common thermal resonance wavelength shifts of the sensing and reference resonators and enables sub-100 kHz (i.e., sub-fm) resonance wavelength shift sensitivity.

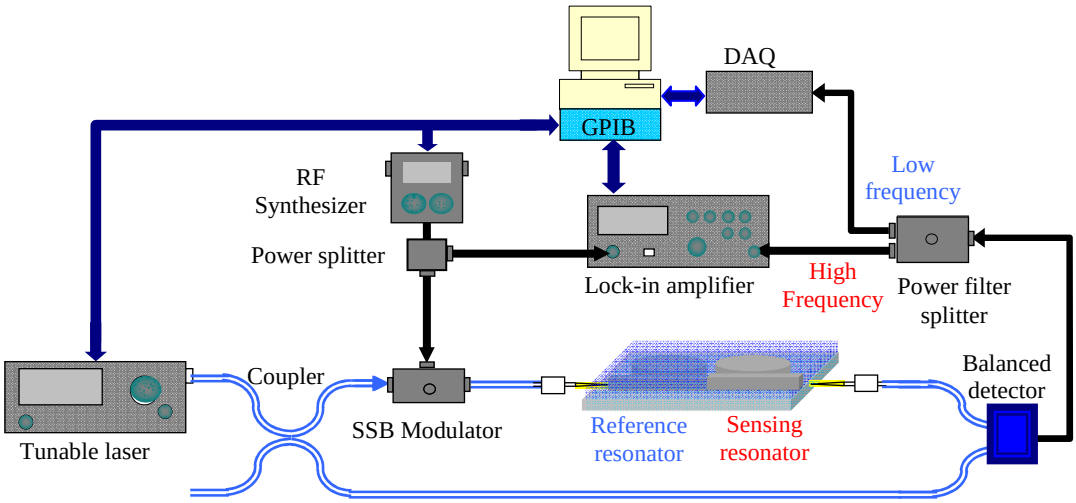

Figure 7. 2: Schematic of the differential sensing set up for continuous measurement for the resonance wavelength shift.

7.4. Large scale label-free microarrays for drug discovery

In this thesis, I studied the principals of the refractive index sensing using compact microdisk resonators. The main advantage of the compact microdisk resonators is their large free spectral range that enables large scale spectral multiplexing. A large scale label-free microarray with up to thousands of sensing spots can be implemented by combining both spectral and spatial multiplexing. This large scale microarray system will find applications in diverse areas, including researches to discover new biomarkes, and investigation of the drug molecules interaction with different biomaterials for drug discovery.

7.5 Experimental demonstration of the simultaneous trapping and sensing of the dielectric particles on high-Q silicon microdisk

The local gradient and propulsion forces in microdisk resonators are proportional to the quality factor to the mode volume ratio (Q/V). The intrinsic Q of the microdisk resonators is limited by the surface absorption and surface scattering [143]. By reducing the microdisk radius in these structures both the intrinsic Q and the resonator mode volume decrease. However, the achievable Q/V ratios for a wide range of radiuses (e.g., from 2 μm to 20 μm) remain almost constant [24]. The trap strength and stability can also be increased by increasing the input power. However, the maximum input power in high-Q Si microdisks is limited to the input power threshold for the thermal and free carrier instabilities. The narrow linewidth of larger microdisk resonators with high-Qs makes them much more susceptible to thermal and free carrier optical nonlinearities. As a result, their input optical power threshold is much smaller than those of the small microdisks [24]. To avoid this issue in our work we have focused on small high-Q microdisks with diameters less than 10 μm.

To demonstrate the possibility of nanoparticle trapping and sensing, a small fluid reservoir is fabricated on the top of the optical structures. The reservoir is filled with a dilute solution of nanoparticles to assure the possibility of single nanoparticle trapping at a time. The nanoparticle and resonator interactions are monitored by monitoring the variations in the CWMR transmission as well as the nanoparticle-induced out-of-plane scattering. Figure 7.3 shows the schematic of the characterization setup. In this characterization setup, two different tunable lasers sources are used. An EDFA is used to amplify the output power of the first tunable laser, which is used as the power source for

the particle trapping. The wavelength of this laser is tuned to a wavelength slightly red shifted in respect to the resonator resonance and will be kept fixed during the experiment. The second laser is used at lower power to simultaneously monitor the variations in the transmission spectrum of the microdisk resonator caused by the trapped nanoparticles. An amplitude modulator and a lock-in amplifier are used to extract the low power monitoring signal from the detected output signal.

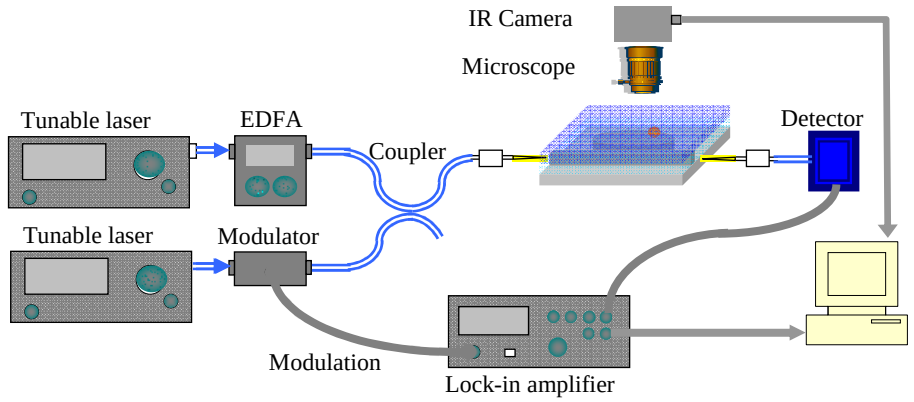

Figure 7.3: Schematic of the characterization setup for dielectric nanoparticle trapping.

7.6 Experimental demonstration of the simultaneous trapping, alignment and sensing of the metallic nanoparticles in micro-resonator structures

In this thesis, we have theoretically investigated the interactions between a nanoresonator with a microdisk resonator and its application for SERS sensing and nanoparticle trapping. The experimental investigation of gold nanoparticles with high-Q resonators will be done in visible (i.e., 652-660 nm) and NIR (i.e., 765-780 nm) wavelengths. High-Q microdisk resonators at visible and NIR wavelength side coupled to single mode waveguides are fabricated on a SiN on oxide substrate. A microfluidic channel similar to the one explained in the previous section will be fabricated on the SiN structure. A dilute solution of gold nanorods in water (Nanopartz Inc.) will be flown through the

microfluidic channel using a syringe pump. The dimensions of the gold nanorods are selected to have their longitudinal surface plasmon resonances (LSPR) around the desired microdisk resonance wavelengths. The input light from a tunable laser source will be coupled to the microdisk resonator through the input waveguide and the wavelength of the laser will be tuned to the resonance wavelength of the microdisk resonator. When a gold nanoparticle approaches the near-field of the microdisk resonator, it causes a reduction in the Q and a red shift in the resonance wavelength of the resonator. The amount of the reduction in the Q and the amount of the resonance wavelength shift depend on the position of the gold nanoparticle in respect to microdisk resonator. Therefore, the interaction of the gold nanorods and microdisk resonator can be monitored through the variations in the transmission amplitude of the CWMR. In addition to the variations in the coupled waveguide-resonator structure transmission amplitude, the out-of-plane scattering of the light in the microdisk resonators through the gold nanorods also will be monitored. A CCD camera mounted on the top of a microscope will be used to image the scattering and the radiation pattern of the gold nanoparticles in the near-field of the microdisk resonator. The monitoring information will be used not only to detect a possible trapping of a nanoparticle in the microdisk optical trap, but also to monitor the nanoparticle movement and dynamics in the trap. The nanoparticle dynamics in the trap will determine the nanoparticle trapping and alignment strength.

To quantify the combined coupled microdisk resonator-gold nanoparticle field enhancement factor SERS labeled gold nanorods (Nanopartz Inc.) will be used. The gold nanoparticles are coated with a thin layer of Cetyl trimethylammonium bromide (CTAB) and are conjugated with a methyl polymer that has Raman resonance peaks at around 200

cm^{-1} and 500 cm^{-1}. The SERS labeled nanoparticles will be excited through the coupling to the microdisk resonator. The emitted SERS signal will be collected out of plane through the top microscope and will be detected by either a spectrometer or a low noise detector. A set of short-pass laser clean-up and long-pass laser blocking Raman filters (Semrock, IDEX Corporation) will be used to suppress the pump laser interference. The SERS signal of single nanoparticles coupled to microdisk resonator will be measured and compared to the measurements obtained for the nanoparticles in the solution.

CHAPTER 8

Conclusions

The main focus of this PhD research has been on the physics, modeling, and implementation of different applications based on light-matter interaction in the vicinity of high-Q resonators in SOI and SiN platforms. The high enhancement of the light-matter interactions in the vicinity of high-Q and small mode-volume resonators enables many applications. In this thesis, I have investigated the high-Q traveling-wave resonators interactions with both resonant and non-resonant nanoparticles. and different applications based on this enhanced interactions in near-field imaging, label-free sensing, optical trapping, and SERS sensing are investigated.

To accomplish this research, several steps have been taken from theory to experiments and different issues have been addressed. First, I developed a near-field imaging system for the investigation of the near-field phenomena in the near-field of high-Q resonators. The developed near-field imaging system uses a coherent detection scheme to provide very high detection sensitivities. Then, the developed near-field imaging system was used to image the near-file pattern of high-Q resonators. However, the required relatively large size of the NSOM tip, for collecting enough signals from the surface of microdisk resonators, results in considerable perturbation of the resonant mode of the resonator and limits the minimum achievable near-field imaging resolution. To address this issue, I developed a new technique based on the near-field perturbation for the imaging of the optical modes in high-Q resonators. The interactions between a small nanoparticle and a microresonator are modeled and used to measure near-field intensity

based on the perturbation in transmission of a coupled waveguide-microresonator system. The proposed new technique enables to achieve a very high resolution (< 10 nm) near-field image with minimal perturbation of the high-Q resonator.

The high Q of compact microdisk resonators and their enhanced interaction with any perturbation in their adjacent environment also enables to achieve high sensitivity label-free sensors for biological and chemical sensing. In this thesis, I have studied the possibility of refractive index sensing using compact microresonators and have proposed different techniques for highly sensitive refractive index sensing based on the on-chip wavelength reference and differential measurement. Furthermore, I have studied different phenomena that affect the efficiency of the sample delivery to the sensor surface and have modeled the interplay between the analyte drift and diffusion in a microfluidic channel and the binding kinetics of the target analyte with the surface coating molecules immobilized on the resonator surface.

The high attractive optical force in the vicinity of the high-Q and small-mode-volume resonators can be used to stably trap a nanoparticle on the surface of a microresonator. I have theoretically shown that the high field enhancement in the microdisk resonators enable low power trapping of small nanoparticle in optical traps generated by compact microdisk resonator.

Finally, I have studied the interaction between a resonant nanoparticle with a high-Q microdisk resonator. I have shown that high field enhancement in high-Q microdisk enables to efficiently couple light to small plasmonic nanoparticle. This efficient coupling of the light to the plasmonic nanoparticles enables to achieve efficient on chip SERS sensing. I have developed a model for interaction of resonant nanoparticles with high-Q

resonators and the optimal parameters for the design of coupled microdisk resonator with a plasmonic nanoparticle are calculated. Furthermore, I have shown that it is possible to trap and align a resonant plasmonic nanoparticle in an SiN microdisk resonator optical trap.

In brief, a summary of the main contributions in these research are as follows:

- Development of a near-field microscopy system for the characterization of the near-field amplitude and phase in integrated photonic device
- Development of a new technique for high-resolution imaging of optical mode in the high-Q resonators
- Development and theoretical and numerical demonstration of high sensitivity differential refractive index sensors for biological sensing.
- Development of a framework for systematic optimization of the design of different aspect of label-free biological sensors from sample delivery to sensing
- Theoretical and numerical demonstration of the possibility of enhancing the binding rate in the integrated photonic label-free sensors using optical trapping.
- Systematic modeling and analysis of the interaction between a plasmonic nanoparticle and a high-Q resonator.
- Calculation of optimal condition for the interaction of a gold nanoparticle and a microresonator.
- Numerical demonstration of the possibility of plasmonic nanoparticle trapping and alignment in the microresonator optical traps.

I hope that the contributions from this thesis will help in paving the road for the future development in the different application of near-field light-matter interactions.

APPENDIX A

Calculation of the trapping lifetime in an exponential optical trap

In Chapter 5, we showed that the nanoparticle lifetime in an optical trap can be calculated from the Equation 5.2. In this appendix we calculate the trapping lifetime for two simplified cases of one dimensional linear and exponential trapping potentials. We are especially interested in exponential traps as the can be used to model the optical traps by the evanescent field.

The weighted nanoparticle density can be related to the nanoparticle input flow by the following equation:

$$J = -DW\nabla M \ . \tag{A1}$$

In a 1D optical trap the trapping field is only a function of the z direction. To calculate the trapping lifetime for a trap that extend up to a distance of b from the surface at *z = 0*, we assume $M(z)\big|_{z=b} = 0$; therefore, using equation A1, the weighted nanoparticle density can be calculated as

$$M(Z) = \frac{J_s}{D}\int_Z^b W^{-1}(z)dz \ . \tag{A2}$$

Therefore, using Equation 5.20 in Chapter 5, the trapping lifetime can be found as

$$\tau = \frac{1}{D}\int_0^b W(Z)\int_Z^b W^{-1}(z)dzdZ \ . \tag{A3}$$

For a linear trap we assume that the normalized trapping potential (V_{trap} , $V_{trap} = \beta I / k_B T$) can be modeled as

$$V_{trap}(z) = V_0(1 - z/b), \tag{A4}$$

where V_0 is the trapping potential on at the trap surface. Replacing $W(z) = \exp(V_{trap}(z))$ in Equation A2, the weighted nanoparticle density can be calculated as

$$M(Z) = \frac{J_s}{D}\int_Z^b e^{-V_0(1-z/b)}dz\,. \tag{A5}$$

By taking the integration in the above equation we have:

$$M(Z) = \frac{J_s b}{DW_0}1-e^{-V_0(1-Z/b)}\,. \tag{A6}$$

By putting the equation A6 in Equation A3 we have:

$$\tau = \frac{b}{DW_0}\int_0^b e^{V_0(1-Z/b)}(1-e^{-V_0(1-Z/b)})dZ\,. \tag{A7}$$

Finally, by calculating the integration in Equation A7, the trapping lifetime in a linear trap can be calculated as

$$\tau = \frac{b^2}{DV_0}\left[\frac{(e^{V_0}-1)}{V_0}-1\right]. \tag{A8}$$

The same formulations that were used for the calculation of the lifetime of a nanoparticle in a linear trap can be applied to the nanoparticle trapping lifetime in an exponentially decaying trap. The trapping potential for an evanescent wave optical trap can be written as

$$V_{trap}(z) = V0e^{-z/d}, \tag{A9}$$

where *d* is the field energy density decay rate. Considering an optical trap with a maximum trapping distance of *b*, the weighted nanoparticle concentration can be found as

$$M(Z) = \frac{J_s}{D}\int_Z^b e^{-V_0e^{-z/d}}dz\,. \tag{A10}$$

The integral in the above equation can be calculated by expanding the exponential term in the integral based on tailor series,

$$M(Z) = \frac{J_s}{D}\int_Z^b 1+\sum_{n=1}^{\infty}\frac{(-V_0)^n}{n!}e^{-nz/d}dz\,. \tag{A11}$$

Therefore,

$$M(Z) = \frac{J_s}{D}\left((b-Z)+d\sum_{n=1}^{\infty}\frac{(-V_0)^n}{nn!}(e^{-nZ/d}-e^{-nb/d})\right). \tag{A12}$$

The trapping time, then, can be calculated as

$$\tau = \frac{1}{D}\int_0^b e^{V_0 e^{-Z/d}}\left((b-Z)+d\sum_{n=1}^{\infty}\frac{(-V_0)^n}{nn!}(e^{-nZ/d}-e^{-nb/d})\right)dZ\,. \tag{A13}$$

Using the tailor expansion again we have:

$$\tau = \frac{1}{D}\int_0^b\left(1+\sum_{m=1}^{\infty}\frac{(V_0)^m}{m!}e^{-mZ/d}\right)\left((b-Z)+d\sum_{n=1}^{\infty}\frac{(-V_0)^n}{nn!}(e^{-nZ/d}-e^{-nb/d})\right)dZ\,. \tag{A14}$$

Assuming b>> d and a high trap stability factor $S_t = V_0$>>1, the above solution be approximated as

$$\tau = \frac{1}{D}\left(\frac{b^2}{2}+\frac{bd}{V_0}(e^{V_0}-V_0-1)\right), \tag{A15}$$

Or in term of the trap stability factor,

$$\tau = \frac{1}{D}\left(\frac{b^2}{2}+\frac{bd}{S_t}(e^{S_t}-S_t-1)\right). \tag{A16}$$

APPENDIX B

Calculation of the nanoparticles cross-section using single point approximation

Once the resonance linewidth and the field profile of a metallic nanoparticle is obtained, the nanoparticle properties such as polarizability, cross-section, and field enhancement factor can be calculated. If the size of a plasmonic nanoparticle is much smaller than the wavelength, the variation of the excitation electric field over the nanoparticle volume is small. Therefore, single point approximation can be used, where the nanoparticle is modeled as a point dipole. The amplitude of the resonant mode of a plasmonic nanoparticle excited by the an electric field [$\overline{E}_{in}(r)$] can be calculated as

$$a_{np} = \frac{j2\overline{\kappa}^{*}_{sp}}{\Gamma_{np}} \frac{1}{1 + j2\delta\omega / \Gamma_{np}} \overline{E}_{in}(r), \tag{B1}$$

where a_{np} is the normalized field amplitude of the resonant mode of the nanoparticle; Γ_{np} is the nanoparticle resonance linewidth; $\delta\omega$ is the frequency detuning between the nanoparticle SPR and the excitation field; and $\overline{\kappa}_{sp}$ is the coupling coefficient between input plane wave and the resonant mode of the nanoparticle, which can be calculate as

$$\overline{\kappa}^{*}_{sp} = \frac{\omega_0}{2} \frac{(\varepsilon_m - \varepsilon_i) \int_{V_{rod}} \overline{E}^{*}_{np}(r)\, dV}{\varepsilon_i V_{np} \left| E^{\max}_{np} \right|^2}. \tag{B2}$$

Therefore, the nanoparticle dipole moment (p) can be calculated by integrating over the induced polarization over the nanoparticle volume:

$$\overline{p} = (\varepsilon_m - \varepsilon_i) \int_{V_{rod}} \overline{E}_{np}(r)\, a_{np}\, dV\,. \tag{B3}$$

By combining Equation B3, Equation B2, and Equation B1, the nanoparticle polarizability tensor can be calculated as

$$\bar{\bar{\alpha}}_{np} = \frac{j\bar{\bar{\alpha}}_0}{1 + j2\delta\omega/\Gamma_{np}}, \tag{B4}$$

where

$$\bar{\bar{\alpha}}_0 = Q_{np}\frac{(\varepsilon_m - \varepsilon_i)^2}{\varepsilon_i V_{np} \mid E_{np}^{\max} \mid^2}\ \bar{p}_0\bar{p}_0^*, \tag{BC5}$$

and $\bar{p}_0 = \left| \int_{V_{rod}} \bar{E}_{np}(r)\, dV \right|$.

The resonance cross-section ($\bar{\bar{\sigma}}$) can be related to the total extinct power (P_{ex}) in the nanoparticle,

$$P_{ex} = 0.5\varepsilon_0 n_i c \bar{E}_{in}^*(r)\bar{\bar{\sigma}}\bar{E}_{in}(r), \tag{B6}$$

Where $P_{ex} = \Gamma_{np}U_{np}$, can be calculated as

$$P_{ex} = 0.5\Gamma_{np}\varepsilon_i V_{np}\left|E_{np}^{\max}\right|^2\left|a_{np}\right|^2. \tag{B7}$$

Combining Equations B1, B2, B6, and B7 we have:

$$\bar{\bar{\sigma}}_{np} = \frac{\bar{\bar{\sigma}}_0}{1 + 4\,(\delta\omega/\Gamma_{np})^{\,2}}, \tag{B8}$$

where

$$\bar{\bar{\sigma}}_0 = \frac{\omega_0 Q_{np}\left|\varepsilon_m - \varepsilon_i\right|^2}{\varepsilon_0 n_i c}\frac{\bar{p}_0\bar{p}_0^*}{\varepsilon_i V_{np}\left|E_{np}^{\max}\right|^2}. \tag{B9}$$

The nanoparticle cross-section and polarizability, then, can be related as

$$\bar{\bar{\sigma}}_0 = \frac{\omega_0}{\varepsilon_0 n_i c}\left|\bar{\bar{\alpha}}_0\right|. \tag{B10}$$

The corresponding field enhancement factor of the nanoparticle ($\left|E_{np}^{\max}\right|/\left|E_{in}(r)\right|$) can be found as

$$\frac{\left|E_{np}^{\max}\right|}{\left|E_{in}\right|} = Q_{np}\,\frac{\left|\varepsilon_m - \varepsilon_i\right|\left|\int_{V_{rod}} E_{np}(r)\,dV\right|}{\varepsilon_i V_{np}\left|E_{np}^{\max}\right|}. \qquad \text{(B11)}$$

REFERENCES

[1] B. Jalali, M. Paniccia, and G. Reed, "Silicon photonics," *IEEE Micro. Mag.*, **l7**, 58 (2006).

[2] O. Painter, R. K. Lee, A. Scherer, and A. Yariv, J. D. O'Brien, P. D. Dapkus, and I. Kim, "Two-dimensional photonic band-gap defect mode laser," *Science* **284**, 1819–21 (1999).

[3] C. Zinoni, B. Alloing, C. Paranthoen, and A. Fiore, "Three-dimensional wavelength scale confinement in quantum dot microcavity light-emitting diodes," *Appl. Phys. Lett.* **85**, 2178–80 (2004).

[4] T. J. Kippenberg, S. M. Spillane, and K. J. Vahala, "Demonstration of ultrahigh- Q small mode volume toroid microcavities on a chip," *Appl. Phys. Lett.* **85**, 6113–15 (2004).

[5] K. J. Vahala, "Optical microcavities," *Nature*, **424**, 6950 (2003).

[6] D. K. Armani, T. J. Kippenberg, S. M. Spillane, and K. J. Vahala, "Ultra-high-Q toroid microcavity on a chip," *Nature* **421**, 925–928 (2003).

[7] Y. Akahane, T. Asano, B. S. Song, and S. Noda, "High-*Q* photonic nanocavity in a two-dimensional photonic crystal," *Nature* **425**, 944 (2003).

[8] T. Asano, B. S. Song, and S. Noda, "Analysis of the experimental *Q* factors (~ 1 million) of photonic crystal nanocavities," *Opt. Express* **14**, 1996 (2006).

[9] P. B. Deotare, M. W. McCutcheon, I. W. Frank, M. Khan, and M. Loncar, "High quality factor photonic crystal nanobeam cavities," *App. Phys. Lett.* **94**, 121106 (2009).

[10] M. Borselli, K. Srinivasan, P.E. Barclay, and O. Painter, "Rayleigh scattering, mode coupling, and optical loss in silicon microdisks," *App. Phys. Lett.* **85**, 3693-3695 (2004).

[11] P. E. Barclay, K. Srinivasan, O. Painter, B. Lev, and H. Mabuchi, "Integration of fiber coupled high-Q SiNx microdisks with atom chips," *Appl. Phys. Lett.* **89**, 131,108 (2006).

[12] L. Novotny, "The History of Near-field Optics," *Progress in Optics* **50**, E. Wolf (ed.), chapter 5, 137- 184 (2007).

[13] B. Hecht, B. Sick, U. P. Wild, V. Deckert, R. Zenobi, O. J. F. Martin, and D. W. Pohl, "Scanning near-field optical microscopy with aperture probes: Fundamentals and applications," *J. Chem. Phys.* **112**, 7761–74 (2000).

[14] X. Fan, I. M. White, S. I. Shopva, H. Zhu, J. D. Suter, and Y. Sun, "Sensitive optical biosensors for unlabeled targets: a review," *Anal. Chem. Acta*, **620**, 8–26 (2008).

[15] B. Liedberg, C. Nylander, and I. Lundstrom, "Biosensing with surface plasmon resonance how it all started," *Biosens. Bioelectron* **10**, 1–9 (1995).

[16] A. Ksendzov and Y. Lin, "Integrated optics ring-resonator sensors for protein detection," *Opt. Lett.* **30**, 3344 (2005).

[17] S. Y. Rabbany, B. L. Donner, and F. S. Ligler, "Optical immunosensors," *Crit. Rev. Biomed. Eng.* **22**, 307–346 (1994).

[18] S. Nie and S. R. Emory, "Surface-Enhanced Raman Scattering Probing Single Molecules and Single by Nanoparticles," *Science* **275**, 1102 (1997).

[19] S. Arnold, M. Khoshsima, I. Teraoka, S. Holler, and F. Vollmer, "Shift of whispering-gallery modes in microspheres by protein adsorption," *Opt. Lett.* **28**, 272-274 (2003).

[20] B. Momeni, S. Yegnanarayanan, M. Soltani, A. Eftekhar, E. Shah Hosseini, and A. Adibi, "Silicon nanophotonic devices for integrated sensing," *J. Nanophoton.* **3**, 031001 (2009).

[21] T. M. Squires, R. J. Messinger, and S. R. Manalis, "Making it stick: convection, reaction and diffusion in surface-based biosensors," *Nature Biotechnol.* **26**, 417-426 (2008).

[22] M. M. Wang, E. Tu, D. E. Raymond, J. M. Yang, H. Zhang, N. Hagen, B. Dees, E. M. Mercer, A. H. Forster, I. Kariv, P. J. Marchand, and W. F. Butler, "Microfluidic sorting of mammalian cells by optical force switching," *Nature Biotechnol.* **23**, 83–87 (2005).

[23] M. Dienerowitz, M. Mazilu, and K Dholakia, "Optical manipulation of nanoparticles: a review", *J. Nanophoton.*, **2**, 021875 (2008).

[24] M. Soltani, "Novel integrated silicon nanophotonic structures using ultra-high-Q resonators," Ph.D. thesis, Georgia Institute of Technology (2009).

[25] H. Haus, W. Huang, "Coupled-mode theory," *Proceedings of IEEE* **79**, 1505 (1991).

[26] A. Yariv, "Universal relations for coupling of optical power between microresonators and dielectric waveguides," *Electron. Lett.* **36**, 321 (2000).

[27] C. Manolatou, M. J. Khan, S. Fan, P. R. Villeneuve, H. A. Haus, J. D. Joannopoulos, "Coupling of modes analysis of resonant channel add-drop filtering," *IEEE J. Lightwave Technol.*, **35**, 1322 (1999).

[28] M. Soltani, S. Yegnanarayanan, Q. Li, A. Adibi, "Systematic Engineering of Waveguide-Resonator Coupling for Silicon Microring/Microdisk/Racetrack Resonators: Theory and Experiment," IEEE Journal of Quantum Electronics **46**, 1158 (2010).

[29] M. Soltani, S. Yegnanarayanan, and A. Adibi, "Ultra-high-Q planar silicon microdisk resonators for chip-scale silicon photonics," Opt. Express **15**, 11 (2007).

[30] P. Schiavone, N. Chaix, Q. Li, A. A. Eftekhar, S. Yegnanarayanan, and A. Adibi, "Fabrication of High-Q Microdisk Resonators Using Thermal Nanoimprint Lithography," Proc. Conference on Lasers and Electro-Optics, OSA Technical Digest (CD) (2010), paper CMI7

[31] P. Schiavone, M. Martin, P. Alipour, A. Eftekhar, S. Yegnanarayanan, and A. Adibi, "3-D AFM Characterization of the Edge Roughness of High-Q Silicon Resonators," Proc. Conference on Lasers and Electro-Optics, OSA Technical Digest (CD) (2010), paper JThE32.

[32] http://nanolithography.gatech.edu

[33] http://www.europractice-ic.com/SiPhotonics_technology.php

[34] S. Scheerlinck, R. H. Pedersen, P. Dumon, W. Bogaerts, U. Plachetka, D. Van Thourhout, R. Baets, and A. Kristensen, "Fabrication of nanophotonic circuit components by thermal nanoImprint lithography," Proc. Conference on Quantum Electronics and Laser Science Lasers and Electro-Optics CLEO/QELS 1-2 (2008).

[35] D. W. Pohl, W. Denk, and M. Lanz, "Optical stethoscopy: Image recording with resolution lambda/20," *Appl. Phys. Lett.* **44**, 651-653 (1984).

[36] E. Betzig and J. K. Trautman, "Near-field optics: Microscopy, spectroscopy, and surface modification beyond the diffraction limit," *Science* **257**, 189-195 (1992).

[37] S. Bourzeix, J. M. Moison, A. F. Mignard, F. Barthe, A. C. Boccara, C. Licoppe, B. Mersali, M. Allovon, and A. Bruno, "Near-field optical imaging of light propagation in semiconductor waveguide structures," *Appl. Phys. Lett.* **73**, 1035–1037 (1998).

[38] M. Abashin, P. Tortora, I. Marki, U. Levy, W. Nakagawa, L. Vaccaro, H. Herzig, and Y. Fainman, "Near-field characterization of propagating optical modes in photonic crystal waveguides," *Opt. Express* **14**, 1643-1657 (2006).

[39] H. Gersen, T. J. Karle, R. J. P. Engelen, W. Bogaerts, J. P. Korterik, N. F. van Hulst, T. F. Krauss, and L. Kuipers, "Real-space observation of ultraslow light in photonic crystal waveguides, " *Phys. Rev. Lett.* **94**, 073903 (2005).

[40] A. L. Campillo, J. W. P. Hsu, C. A. White and A. Rosenberg, "Mapping the optical intensity distribution in photonic crystals using a near-field scanning optical microscope," *J. Appl. Phys.* **89**, 2801-2807 (2001).

[41] S. Gotzinger, S. Demmerer, O. Benson, V. Sandoghdar , “Mapping and manipulating whispering gallery modes of a microsphere resonator with a near-field probe,” *J. Microscopy* **202**, 117 (2001).

[42] E. Verhagen, J.A. Dionne, L. Kuipers, H.A. Atwater and A. Polman, “ Near-Field Visualization of Strongly Confined Surface Plasmon Polaritons in Metal-Insulator-Metal Waveguides,” *Nano lett.* **8**, 2925-2929 (2008).

[43] P. Tortora, M. Abashin, I. Marki, W. Nakagawa, L.Vaccaro, M. Salt, HP. Herzig, U. Levy, and Y. Fainman, “Observation of amplitude and phase in ridge and photonic crystal waveguides operating at 1.55 mu m by use of heterodyne scanning near-field optical microscopy,” *Opt. Lett.* **30**, 2885-2887 (2005).

[44] E. Betzig and J. K. Trautman, “Near-field optics: Microscopy, spectroscopy, and surface modification beyond the diffraction limit,” *Science* **257**, 189-195 (1992).

[45] Y. Inouye and S. Kawata, “Near-field scanning optical microscope with a metallic probe tip,” *Opt. Lett.* **19**, 159-161 (1994).

[46] R. Bachelot, P. Gleyzes, and A. C. Boccara, “Near-field optical microscope based on local perturbation of a diffraction spot,” *Opt. Lett.*, **20**, 1924-1926 (1995).

[47] I. Stefanon, S. Blaize, A. Bruyant, S. Aubert, G. Lerondel, R. Bachelot, and P. Royer, “Heterodyne detection of guided waves using a scattering-type scanning near-field optical microscope,” *Opt. Express*, **13**. 5553-5564 (2005).

[48] J. T. Robinson, S. F. Preble, and M. Lipson, “Imaging highly confined modes in sub-micron scale silicon waveguides using Transmission based Near-field Scanning Optical Microscopy,” *Opt. Express* **14**, 10588-10595 (2006).

[49] M. Abashin, U. Levy, K. Ikeda, and Y. Fainman, "Effects produced by metal-coated near-field probes on the performance of silicon waveguides and resonators," *Opt. Lett.* **32**, 2602-2604 (2007).

[50] A. F. Koenderink, R. Wüest, B. C. Buchler, S. Richter, P. Strasser, M. Kafesaki, A. Rogach, R. B. Wehrspohn, C. M. Soukoulis, D. Erni, F. Robin, H. Jäckel, and V. Sandoghdar, “Near field optics and control of photonic crystals”, *Photon. Nanostruct.* **3**, 63-74 (2005).

[51] I. Märki, M. Salt, and H. P. Herzig, “Tuning the resonance of a photonic crystal microcavity with an AFM probe,” *Opt. Express* **14**, 2969-2978 (2006).

[52] S. Mujumdar, A. F. Koenderink, T. Sünner, B. C. Buchler, M. Kamp, A. Forchel, and V. Sandoghdar, "Near-field imaging and frequency tuning of a high-Q photonic crystal membrane microcavity," *Opt. Express* **15**, 17214-17220 (2007).

[53] L. Lalouat, B. Cluzel, F. de Fornel, P Velha, P Lalanne, D Peyrade, E Picard, T. Charvolin, and E Hadji, "Subwavelength imaging of light confinement in high-Q/small-V photonic crystal nanocavity," *App. Phys. Lett.* **92**, 111111, (2008)

[54] W. C. L. Hopman, K. O. van der Werf, A. J. F. Hollink, W. Bogaerts, V. Subramaniam, and R. M. de Ridder, "Nano-mechanical tuning and imaging of a photonic crystal micro-cavity resonance," *Opt. Express* **14**, 8745-8752 (2006).

[55] T.J Robinson, M Lipson, "Far-Field Control of Radiation from an Individual Optical Nanocavity: Analogue to an Optical Dipole," *Phys. Rev. Lett.* **100**, 043902 (2008).

[56] S. Yegnanarayanan, M. Soltani, E. Shah Hosseini, A. Eftekhar, and A. Adibi, "Microresonators in CMOS compatible substrates," J. Nanoscience and Nanotechnology, (accepted, to appear January 2010).

[57] D. Weiss, V. Sandoghdar, J. Hare, V. Lef´evre-Seguin, J. Raimond, and S. Haroche, "Splitting of high-Q Mie modes induced by light backscattering in silica microspheres," *Opt. Lett.* **22**, 1835-1837 (1995).

[58] T. J. Kippenberg, S. M. Spillane, and K. J. Vahala, "Modal coupling in traveling-wave resonators," *Opt. Lett.* **27**, 1669- 1671 (2002).

[59] S. Mujumdar, A. F. Koenderink, T. Sünner, B. C. Buchler, M. Kamp, A. Forchel, and V. Sandoghdar, "Near-field imaging and frequency tuning of a high-Q photonic crystal membrane microresonator," *Opt. Express* **15**, 17214-17220, (2007).

[60] A. A. Eftekhar, S. Yegnanarayan, M. Soltani, and A. Adibi, "High-resolution imaging of optical modes in high-Q microdisk resonators," Submitted to Opt. Express.

[61] C. F. Bohren and D. R. Huffman, "Absorption and scattering of light by small particles," New York, Wiley, (1998).

[62] A. A. Eftekhar, M. Soltani, S. Yegnanarayanan, and A. Adibi, "Characterization of the Effect of Small Perturbations on the Optical Modes in High-Q Microdisk Cavities," in Conference on Lasers and Electro-Optics/Quantum Electronics and Laser Science Conference and Photonic Applications Systems Technologies, OSA Technical Digest (CD) (Optical Society of America, 2008), paper CTuDD3.

[63] E. Shah Hosseini, S. Yegnanarayanan, A. Atabaki , M. Soltani, and A. Adibi, "Systematic design and fabrication of high-Q pulley-coupled planar silicon nitride microdisk resonators," *Opt. Express* **18**, 2127-2136 (2010)

[64] A. A. Eftekhar, M. Soltani, S. Yegnanarayanan, and A. Adibi, "High Resolution Imaging of Optical Modes in Silicon Microdisk Cavities Based on Near-Field Perturbation," in *Conference on Lasers and Electro-Optics/International Quantum Electronics Conference*, OSA Technical Digest (CD) (Optical Society of America, 2009), paper CTuE1.

[65] M. A. Cooper, “Optical biosensors: where next and how soon,” *Drug Discov. Today* **11**, 1061-1067 (2006).

[66] X. Fan, I.M. White, S.I. Shopova, H. Zhu, J.D. Suter and Y. Sun, “Sensitive optical biosensors for unlabeled targets: A review,” Anal. Chim. Acta **620,** 8-26 (2008).

[67] F. Prieto, B. Sepulveda, A. Calle, A Llobera, C. Dominguez, A. Abad, A. Montoya and L.M. Lechuga, “An integrated optical interferometric nanodevice based on silicon technology for biosensor applications,” Nanotech. **14**, 907 (2003).

[68] A. Ksendzov, Y. Lin, “Integrated Optics Ring-resonator Sensors for Protein Detection,” Opt. Lett. 30, 3344 (2005).

[69] S. Blair and Y. Chen, "Resonant-Enhanced Evanescent-Wave Fluorescence Biosensing with Cylindrical Optical Cavities," Appl. Opt. **40**, 570 (2001).

[70] B. Liedberg, C. Nylander and I. Lundstrom, “Surface plasmon resonance for gas detection and biosensing,” *Sens. Actuators* **4**, 299–304 (1983).

[71] J. Homola, S.S. Yee and G. Gauglitz, “Surface plasmon resonance sensors: review,” *Sens. Actuators B* **54,** 3–15 (1999).

[72]J. Homola, “Surface plasmon resonance sensors for detection of chemical and biological species,” *Chem. Rev.* **108**, 462–493 (2008).

[73] P.P.P. Debackere, R. Baets, P. Bienstman, “Bulk sensing experiments using a surface-plasmon interferometer,” *Opt. Lett.* **34**, 2858-2860, (2009).

[74] F. Prieto, B. Sepulveda, A. Calle, A Llobera, C. Dominguez, A. Abad, A. Montoya and L.M. Lechuga, “An integrated optical interferometric nanodevice based on silicon technology for biosensor applications,” *Nanotech.* **14**, 907-912 (2003).

[75] F. Vollmer, D. Braun, A. Libchaber, M. Khoshsima, I. Teraoka, S. Arnold, “Protein Detection by Optical shift of a Resonant Microcavity”, *Appl. Phys. Lett.* **80**, 4057-4059 (2002).

[76] A. Ksendzov, Y. Lin, “Integrated optics ring-resonator sensors for protein detection,” *Opt. Lett.* **30**, 3344- 3346 (2005).

[77] J. T. Robinson, L. Chen, and M. Lipson, “On-chip gas detection in silicon optical microcavities,” *Opt. Express* **16**, 4296–4301 (2008).

[78] E. Chow, A. Grot, L. W. Mirkarimi, M. Sigalas, and G. Girolami, “Ultracompact biochemical sensor built with two-dimensional photonic crystal microcavity,” Opt. Lett. **29**, 1093-1095, (2004).

[79] B. Schmidt, V. Almeida, C. Manolatou, S. Preble, and M. Lipson, “Nanocavity in a silicon waveguide for ultrasensitive nanoparticle detection,” *Appl. Phys. Lett.* **85**, 4854–6 (2004).

[80] S. Arnold, M. Khoshsima, I. Teraoka, S. Holler, and F. Vollmer, “Shift of whispering-gallery modes in microspheres by protein adsorption,” *Opt. Lett.* **28**, 272-274 (2003).

[81] F. Vollmer, S. Arnold, D. Braun, I. .Teraoka, A. Libchaber, “DNA detection from the shift of whispering gallery modes in multiple microspheres,” *J. Bio. Phys.* **84**, 295A, (2003).

[82] I. Teraoka and S. Arnold, “Theory of resonance shifts in TE and TM whispering gallery modes bynonradial perturbations for sensing applications,” *J. Opt. Soc. Am. B* **23**, 1381-1389 (2006).

[83] H. C. Ren, F. Vollmer, S. Arnold, A. Libchaber, "High-Q microsphere biosensor - analysis for adsorption of rodlike bacteria," *Opt. Express* **15**, 17410-17423 (2007).

[84] F. Vollmer, S. Arnold, and D. Keng, “Single Virus Detection from the Reactive Shift of a Whispering-Gallery Mode,” *Proc. Natl. Acad. Sci. USA* **105**, 20701-20704 (2008).

[85] A. M. Armani, R. P. Kulkarni, S. E. Fraser, R. C. Flagan, K. J. Vahala , “Label-free, single-molecule detection with optical microcavities,” *Science* **317**, 783-787 (2007).

[86] Mandal, S., Erickson, D., “Nanoscale Optofluidic Sensor Arrays,” *Opt. Express* **16**, 1623-1631 (2008).

[87] Mandal, S., Goddard, J,., Erickson, D., “A Multiplexed Optofluidic Biomolecular Sensor for Low Mass Detection,” *Lab on a chip* **9**, 2924-2932 (2009).

[88] K. De Vos, I. Bartolozzi, E. Schacht, P. Bienstman, and R. Baets, “Silicon-on-Insulator microring resonator for sensitive and label-free biosensing,” *Opt. Express* **15**, 7610-7615 (2007).

[89] C.-Y. Chao, W. Fung, and L. J. Guo, “Polymer microring resonators for biochemical sensing applications,” *JSTQE* **12**, 134-142, (2006).

[90] T. Claes, J. Girones Molera, K. De Vos, E. Schacht, R. Baets, P. Bienstman, “Label-Free Biosensing With a Slot-Waveguide-Based Ring Resonator in Silicon on Insulator,” *IEEE Photon. J.* **1**, 197-204 (2009).

[91] A. Nitkowski, L. Chen, and M. Lipson, “Cavity-enhanced on-chip absorption spectroscopy using microring resonators,” *Opt. Express* **16**, 11930-11936 (2008).

[92] T. Claes, J. Girones Molera, K. De Vos, E. Schacht, R. Baets, P. Bienstman, “Label-Free Biosensing With a Slot-Waveguide-Based Ring Resonator in Silicon on Insulator,” *IEEE Photon. J.* **1**, 197-204 (2009).

[93] T. Gervais and K. F. Jensen, “Mass transport and surface reactions in microfluidic systems,” Chem. Eng. Sci., **61**, 1102 – 1121, (2006).

[94] X. Liang, Q. Zhang, and H. Jiang, "Quantitative reconstruction of refractive index distribution and imaging of glucose concentration by using diffusing light," Appl. Opt. **45**, 8360-8365 (2006).

[95] A. Ashkin, J. M. Dziedzic, J. E. Bjorkholm, and S.Chu, “Observation of a single-beam gradient force optical trap for dielectric particles,” *Opt. Lett.* **11**, 288–290 (1986).

[96] D. G. Grier, “A revolution in optical manipulation,” *Nature* **424**, 810–816 (2003).

[97] M. P. MacDonald, G. C. Spalding, and K. Dholakia, “Microfluidic sorting in an optical Lattice,” *Nature* **426**, 421–424 (2003).

[98] L. Novotny, R. X. Bian, X. S. Xie, “Theory of nanometric optical tweezers,” *Phys. Rev. Lett.* **79**, 645–648 (1997).

[99] S. Kawata and T. Sugiura, “Movement of micrometer-sized particles in the evanescent field of a laser beam,” *Opt. Lett.* **17**, 772-774 (1992).

[100] S. Kawata and T. Tani, “Optically driven Mie particles in an evanescent field along a channeled wave guide,” *Opt. Lett.* **21**, 1768-1770 (1996).

[101] Mandal, S., Erickson D., “Optofluidic Transport in Liquid Core Waveguiding Structures,” *Appl. Phys. Lett.* **90**, 184103 (2007).

[102] Schmidt, B.S., Yang, A.H.J., Erickson D., Lipson, M. “Optofluidic trapping and transport on solid core waveguides within a microfluidic device” *Opt. Express* **15**, 14322-14334 (2007).

[103] P. Measor, S. Kühn, E.J. Lunt, B.S. Phillips, A.R. Hawkins, and H. Schmidt, "Hollow-core Waveguide Characterization by Optically Induced Particle Transport", *Opt. Lett.* **33**, 672-674 (2008).

[104] A. H. J. Yang, S. D. Moore, B. S. Schmidt, M. Klug, M. Lipson, D. Erickson, “Optical manipulation of nanoparticles and biomolecules in sub-wavelength slot waveguides,” *Nature* **457**, 71-75 (2009).

[105] A. H. J. Yang, T. Lerdsuchatawanich, D. Erickson, D., “Forces and Transport Velocities for a Particle in a Slotted Waveguide” Nano. Lett. **9**, 1182-1188 (2009).

[106] L. Huang, S. J. Maerkl, and O. J. Martin, "Integration of plasmonic trapping in a microfluidic environment," *Opt. Express* **17**, 6018-6024 (2009).

[107] X. Miao, B. K. Wilson, S. H. Pun, and L. Y. Lin, "Optical manipulation of micron/submicron sized particles and biomolecules through plasmonics," *Opt. Express* **16**, 13517-13525 (2008).

[108] A. Rahmani and P. C. Chaumet, "Optical trapping near a photonic crystal," *Opt. Express* **14**, 6353-6358 (2006).

[109] M. Rosenblit, Y. Japha, P. Horak, and R. Folman, "Simultaneous optical trapping and detection of atoms by microdisk resonators," *Phys. Rev. A* **73**, 063805 (2006).

[110] S. Arnold, D. Keng, S. I. Shopova, S. Holler, W. Zurawsky, and F. Vollmer, "Whispering gallery mode carousel – a photonic mechanism for enhanced nanoparticle detection in biosensing," *Opt. Express* **17**, 6230-6238 (2009).

[111] B. Momeni, S. Yegnanarayanan, M. Soltani, A. Eftekhar, E. Shah Hosseini, and A. Adibi, "Silicon nanophotonic devices for integrated sensing," *J. Nanophoton.* **3**, 031001 (2009).

[112] R. N. C. Pfeifer, T. A. Nieminen, N. R. Heckenberg, and H. Rubinsztein-Dunlop, "Colloquium: Momentum of an electromagnetic wave in dielectric media," *Rev. Mod. Phys.* **79**, 1197-1216 (2007).

[113] M. Mansuripur and A. R. Zakharian, "Maxwell's macroscopic equations, the energy-momentum postulates, and the Lorentz law of force," *Phys. Rev. E* **79**, 026608 (2009).

[114] M. L. Povinelli, S. G. Johnson, M. Loncar, M. Ibanescu, E. J. Smythe, F. Capasso, and J. D. Joannopoulos, "High-Q enhancement of attractive and repulsive optical forces between coupled whispering-gallery-mode resonators," *Opt. Express* **13**, 8286-8295 (2005).

[115] A. H. J. Yang, T. Lerdsuchatawanich, and D. Erickson, "Forces and Transport Velocities for a Particle in a Slotted Waveguide," *Nano Lett.* **9**, 1182-1188 (2009).

[116] B. Lukic, S. Jeney, Z. Sviben, A. J. Kulik, E.-L. Florin, and L. Forro, "Motion of a colloidal particle in an optical trap," *Phys. Rev. E* **76**, 011112 (2007).

[117] T. J. Davis, "Brownian diffusion of nano-particles in optical traps," *Opt. Express* **15**, 2702-2712 (2007).

[118] M. Soltani, Q. Li, S. Yegnanarayanan, and A. Adibi, "Toward ultimate miniaturization of high-Q silicon traveling-wave microresonators," Opt. Express **18**, 19541-19557 (2010).

[119] M. G. Albrecht and J. A. Creighton, “Anomalously intense Raman spectra of pyridine at a silver electrode,” *J. Am. Chem. Soc.* **99**, 5215-5217 (1977).

[120] D. L. Jeanmaire and R. P. Van Duyne, “Surface Raman spectroelectrochemistry Part I. Heterocyclic, aromatic, and aliphatic amines adsorbed on the anodized silver electrode,” *J. Electroanal. Chem.* **84**, 1-20 (1977).

[121] Huh, Y.S., Lowe, A., Strickland, S., Batt, C.A., Erickson, D., “A Surface Enhanced Raman Scattering based Ligase Detection Reaction,” *J. Am. Chem. Soc.* **131**, 2208-2213 (2009).

[122] A. M. Michaels, M. Nirmal, and L. E. Brus, “Surface enhanced Raman spectroscopy of individual rhodamine 6G molecules on large Ag nanocrystals,” *J. Am. Chem. Soc.* **121**, 9932-9939 (1999).

[123] K. Kneipp, Y. Wang, H. Kneipp, L. T. Perelman, I. Itzkan, R. R. Dasari, and M. S. Feld, “Single molecule detection using surface-enhanced Raman scattering (SERS),” *Phys. Rev. Lett.* **78** (1997).

[124] F. M. Cox, A. Argyros, M. C. J. Large, and S. Kalluri, "Surface enhanced Raman scattering in a hollow core microstructured optical fiber," *Opt. Express* **15**, 13675-13681 (2007).

[125] P. Measor, L. Seballos, D. Yin, J. Z. Zhang, E. J. Lunt, A. R. Hawkins, and H. Schmidt, “On-chip surfaceenhanced Raman scattering detection using integrated liquid-core waveguides,” *Appl. Phys. Lett.* **90**, 211107 (2007).

[126] I. M. White, J. Gohring, and X. Fan, "SERS-based detection in an optofluidic ring resonator platform," *Opt. Express* **15**, 17433-17442 (2007).

[127] H. Zhu, I. M. White, J. D. Suter, P. S. Dale, and X. Fan, “Analysis of biomolecule detection with optofluidic ring resonator sensors,” *Opt. Express* **15**, 9139-9146 (2007).

[128] M. Chamanzar, E. Shah Hosseini, S. Yegnanarayanan, and A. Adibi, "Hybrid Plasmonic-photonic Resonators for Sensing and Spectroscopy," Proc. Conference on Lasers and Electro-Optics, OSA Technical Digest (CD) (2011), paper QTuE4.

[129] M. Chamanzar, E. Shah Hosseini, S. Yegnanarayanan, and A. Adibi, " Evanescent Excitation of Plasmonic Nanodisks Using Hybrid Guided Wave Silicon Nitride Structures," Proc. Conference on Lasers and Electro-Optics, OSA Technical Digest (CD) (2010), paper JThE49.

[130] B. Nikoobakht and M. A. El-Sayed, “Surface-Enhanced Raman Scattering Studies on Aggregated Gold Nanorods,” *J. Phys. Chem. A*, **107**, 3372–3378 (2003).

[131] P.K. Jain, K.S. Lee, I.H. El-Sayed, and M.A. El-Sayed, “Calculated absorption and scattering properties of gold nanoparticles of different size, shape, and composition:

Applications in biological imaging and biomedicine," *J. Phys. Chem. B* **110**, 7238-7248 (2006).

[132] E. Moreno, D. Erni, C. Hafner, and R. Vahldieck, "Multiple multipole method with automatic multipole setting applied to the simulation of surface plasmons in metallic nanostructures," *J. Opt. Soc. Am. A* **19**, 101-111 (2002).

[133] W. H. Ni, X. S. Kou, Z. Yang, J. F. Wang, "Tailoring longitudinal surface plasmon wavelengths, scattering and absorption cross sections of gold nanorods", ACS Nano **2**, 677-686 (2008).

[134] L.D. Landau, E.M. Lifshitz, and L.P. Pitaevskii, Electrodynamic of Continuous Media, 2nd edn., Pergamon Press, Oxford (1984).

[135] K. Svoboda and S. M. Block, "Optical trapping of metallic Rayleigh particles," *Opt. Lett.* **19**, 930–932 (1994).

[136] P. M. Hansen, V. K. Bhatia, N. Harrit, L. Oddershede, "Expanding the optical trapping range of gold nanoparticles," *Nano Lett.* **5**, 1937-1942 (2005).

[137] M. Pelton, M. Liu, H. Y. Kim, G. Smith, P. Guyot-Sionnest, and N. F. Scherer, "Optical trapping and alignment of single gold nanorods by using plasmon resonances," *Opt. Lett.* **31**, 2075-2077 (2006).

[138] K. C. Toussaint, M. Liu, M. Pelton, J. Pesic, M. J. Guffey, P. Guyot-Sionnest, and N. F. Scherer, "Plasmon resonance-based optical trapping of single and multiple Au nanoparticles," *Opt.. Express* **15**, 12017-12029 (2007).

[139] M. E. J. Friese, T. A. Nieminen, N. R. Heckenberg, and H. Rubinsztein-Dunlop, "Optical alignment and spinning of laser-trapped microscopic particles," *Nature* **394**, 348–350 (1998).

[140] M. Mansuripur, "Electromagnetic force and torque in ponderable media," Opt. Express **16**, 14821-14835 (2008).

[141] H. J. Butt, B. Cappella, and M. Kappl, "Force measurements with the atomic force microscope: Technique, interpretation and applications," *Surf. Science report* **59**, 1-6 (2005).

[142] P. M. Claesson, T. Ederth, V. Bergeron, and M. W. Rutland, "Techniques for measuring surface forces," *Adv. colloid and Interface Science* **67**, 119-183 (1996).

[143] M. Borselli, T. J. Johnson, and O. Painter, "Beyond the Rayleigh scattering limit in high-Q silicon microdisks: theory and experiment," *Opt. Express* **13**, 1515-1530 (2005).

VITA

ALI ASGHAR EFTEKHAR

Ali Asghar Eftekhar received his B.S. and M.S. degree in electrical engineering from Sharif University of Technology in 1996 and 1998, respectively. He has received honorable mention from the 23th International Physics Olympiad in 1992 in Helsinki, Finland, and also ranked first in the national Iranian electrical engineering competition in 1996. He has co-founded two startup companies in 1999 and 2002 in the field of digital broadcasting technology, wireless technology, digital processing, IP telephony, and soft switching, where he has served as technical manager and CEO from 1999 to 2003, respectively, before moving to US to pursue a Ph.D. degree in electrical engineering. He is currently a Ph.D. student and research engineer at Georgia Institute of Technology. His current research interests include, integrated photonic and plasmoninc devices and systems for RF photonics, Bio and chemical sensing, and on-chip interconnection applications; near-field optical microscopy; and integrated acoustic nanostructures.